

THE QUEST FOR ACTIVE MEDIA MODELS: A SELF-CONSISTENT FRAMEWORK FOR
SIMULATING WAVE PROPAGATION IN NONLINEAR SYSTEMS

By

Connor Adrian Glosser

A DISSERTATION

Submitted to
Michigan State University
in partial fulfillment of the requirements
for the degree of

Physics – Doctor of Philosophy
Electrical Engineering – Dual Degree

2018

ABSTRACT

THE QUEST FOR ACTIVE MEDIA MODELS: A SELF-CONSISTENT FRAMEWORK FOR SIMULATING WAVE PROPAGATION IN NONLINEAR SYSTEMS

By

Connor Adrian Glosser

This work presents new approaches to simulations of active media at the level of individual particles. Active systems contain internal, nonlinear, processes beyond those of simple scattering systems; thus these new models afford high degrees of fidelity in exploring the underlying physics without recourse to continuum or spatially-averaged approximations.

First, I examine the dynamics of microspheres set into motion by ambient acoustic radiation in a fluid described by potential flow in the long-wavelength limit. Variations in the local surface pressure caused by scattering from each microsphere set each microsphere into motion following Newton's second law. By expanding this pressure in terms of spherical harmonics—natural eigenfunctions of the unretarded radiation kernel—I recover an analytic description of the force on individual microspheres due to an incident waveform. High-order numerical integrations then relate the surface potential on one microsphere to the surface pressure on the others, thereby coupling the microspheres' trajectories. These simulations predict a dominant translational effect along the direction of propagation of the incident waveform, though they also reveal significant dipolar interactions between microspheres that produce secondary expansions and contractions of the collective microsphere system.

Extending my approach from acoustic to electromagnetic systems, I apply it to a collection of quantum dots: "artificial" two-level atoms with a size-dependent energy structure. The optical Maxwell-Bloch equations give the evolution of quantum dots under the influence of electromagnetic fields; this evolution then produces secondary radiation that couples a collection of quantum dots together. In my computational model, I cast my secondary electromagnetic fields in terms of a point-to-point integral operator that

accurately recovers both near- and far-field effects. These fields, then, drive a set of implicitly coupled Bloch equations (solved with an exponentially-fitted predictor/corrector scheme) to give the dynamics of the system as a whole. In ensembles of up to 10 000 quantum dots, my model predicts synchronized multiplets of particles that exchange energy, quantum dots that dynamically couple to screen the effect of incident external radiation, localization of the polarization due to randomness and interactions, as well as wavelength-scale regions of enhanced and suppressed polarization.

The remainder of the work uses the same physical quantum dot system while moving towards efficient computer-aided device design. I detail an improved propagation algorithm to reduce the time and space complexity of the simulation dramatically, thereby facilitating rapid analysis of promising device structures. The algorithm makes use of physical and numerical approximations to effect large-scale calculations in reasonable CPU time. A rotating-frame approximation removes high-frequency components in the evolution of the system while simultaneously preserving accurate interference phenomena in space, thereby affording far larger simulation timesteps. Additionally, projecting the source current distribution onto a regular spatial grid makes use of a low-rank approximation to the field propagator to communicate radiation information between distant groups of particles via fast Fourier transforms in a manner reminiscent of fast multipole methods.

Copyright by
CONNOR ADRIAN GLOSSER
2018

I dedicate this thesis to my loving mom and dad, Cindy and Ron, and their eternal, unconditional support.

ACKNOWLEDGMENTS

As I reflect on closing this chapter of my life, I can't help but beam at the memories of everyone who has helped shape me into the person I am today. Thanks in no small part to my studies, I've gotten to meet many truly incredible people who guided me when I felt lost, encouraged my grandiose schemes, or simply shared a portion of their story with me. Some of you remain with me and some of you have left only marks, but I am a far better person for having spent time with all of you and I offer my dearest thanks here.

First and foremost, I need to thank my incredible parents, Cindy Roach and Ron Glosser. I truly don't have enough words to express my gratitude for the love and support you've given me in everything I've decided to pursue, academic or otherwise. Whereas school taught me facts, you gave me what I needed to *think* and examine the world around me, no doubt setting me on a lifelong journey of scientific and personal discovery on which this Ph.D is but a stop.

Next, I'd like to thank my two wonderful advisers-turned-friends, Carlo Piermarocchi and Shanker Balasubramaniam. I'm so happy my interests put me on a course to work with both of you daily and I don't think I could have asked for better mentors as I concurrently learned to be both a physicist and an engineer. Together you've taught me a great deal about doing science on a computer and a great deal more about determination and professionalism. It saddens me that I have to leave MSU now that I've just started to come into my own as a researcher, but it makes me much happier to think that we'll find ways to collaborate for a long time to come.

I'd also like to thank the members of my committee—Phil Duxbury, Stuart Tessmer, John Albrecht, and John Luginsland—for your encouragement and insights into the work I present here. Phil, I need to thank you in particular for giving my high-school self the chance to experience what being a scientist is like. When we started working together in 2008 (if you could call a high-schooler's attempts at research "work") I had no idea I

was taking my first steps on a road that would lead me across a couple of continents and through a Ph.D. I realize now I've learned so much about the world and the people that live in it for having walked that road with you, and I sincerely hope I can pay your kindness forward to many students of my own someday.

Xander van Kooten, Liz Fujita, Kim & Erin McGarrity, Scott O'Connor, and Bill Martinez, thank you for being such noble and selfless companions. You all have shown me exceptional warmth and kindness when I've needed it most, and every day you inspire me to learn, do, or try something new and to become the best person I can be. While we may sometimes live a great distance apart, I find tremendous joy in knowing our shared sense of adventure will reunite us with striking regularity. You will always have a home with me.

Jenni & Giuseppe Zerilli, Dan & Marilyn Olds, Shannon Nicley, Chelsea Johnson, and Gift Pimcharoen, I cashed in all my undergrad points for this Ph.D, but somehow I only ended up with more undergrad points. Thank you for adopting me into Game Night and showing me the *real* ropes of graduate school. Our evenings spent betraying each other and hurling (false) accusations of betraying each other remain some of my favorite memories of my time at MSU and I hope we can find time for numerous reunions soon.

Jos Thijssen, Chris Verzijl, Laurens Janssen, Félix Carlier, Joost de Gussem, Max Huisman, Witek Nawara, Daan Kuitenbrouwer, and all of the other ICCP-ers, thank you for sharing so much of your culture with this loudmouth American. Everything I ever needed to know about grad school I learned in ICCP alongside you all, and the class simply would not have existed without the many international exchanges you helped facilitate.

Finally, thanks to some of the friends I've had along the way: Charlie & JoAnn Steele, Juan Manfredi, Tony Szedlak, Chris Sullivan, Robin de Kivit, Håkon Jensen, Julia Rohrer, Louis Garcia, Mike Bennett, Chris Morse, and Steve Hughey. You all continue to brighten my days with discussions of everything from the latest philosophies on doing science to the most entertaining (and possibly least effective) game strategies.

You all have routinely helped me find my way into truly magnificent experiences greater than any I could have imagined, and for that I am profoundly grateful. I consider myself beyond fortunate to count you amongst my friends and family and I sincerely hope our bonds last long, long into the future. Thank you all for everything you have given me.



TABLE OF CONTENTS

| | |
|--|------------|
| LIST OF TABLES | xi |
| LIST OF FIGURES | xii |
| CHAPTER 1 INTRO | 1 |
| 1.1 Active media | 1 |
| 1.1.1 Acoustophoresis | 2 |
| 1.1.2 Light in disordered media | 3 |
| 1.2 Numerical simulation of wave propagation | 4 |
| CHAPTER 2 ACOUSTOPHORESIS IN RIGID MICROSPHERES | 6 |
| 2.1 Introduction | 6 |
| 2.2 Continuum problem statement | 7 |
| 2.3 Discretization of the Integral Equations | 9 |
| 2.4 Analytic results | 12 |
| 2.4.1 Single microsphere solution | 12 |
| 2.4.2 Low-order interactions | 14 |
| 2.5 Numerical Results | 15 |
| 2.5.1 Single microspheres | 16 |
| 2.5.2 Many-particle simulations | 18 |
| 2.6 Conclusions | 21 |
| CHAPTER 3 RADIATION IN COUPLED QUANTUM DOT SYSTEMS | 23 |
| 3.1 Introduction | 23 |
| 3.2 Problem Statement | 25 |
| 3.3 Computational Approach | 27 |
| 3.4 Numerical Results | 31 |
| 3.4.1 Stability & adjacency effects | 31 |
| 3.4.2 Polarization enhancement | 35 |
| 3.4.3 Inhomogeneous broadening | 37 |
| 3.5 Conclusions & future work | 37 |
| CHAPTER 4 AN FFT-ACCELERATED SOLUTION METHODOLOGY FOR RADIATIVE MAXWELL-BLOCH SYSTEMS | 40 |
| 4.1 Abstract | 40 |
| 4.2 Introduction | 40 |
| 4.3 Problem statement | 42 |
| 4.4 Computational approach | 43 |
| 4.4.1 Expansion matrices | 47 |
| 4.4.2 Complexity | 49 |
| 4.5 Results | 50 |
| 4.5.1 Convergence | 50 |

| | | |
|---|--|-----------|
| 4.5.2 | Timing | 52 |
| 4.5.3 | Maxwell-Bloch | 53 |
| CHAPTER 5 CONCLUSIONS AND FUTURE PERSPECTIVE | | 55 |
| 5.1 | Conclusion | 55 |
| 5.2 | Discussion | 57 |
| 5.2.1 | Advanced dissipators | 57 |
| 5.2.2 | Micromagnetics | 58 |
| 5.2.2.1 | Technical details | 59 |
| APPENDICES | | 61 |
| APPENDIX A | QuEST Manual | 62 |
| APPENDIX B | The predictor/corrector integration scheme | 67 |
| APPENDIX C | Chebyshev polynomials | 72 |
| APPENDIX D | Conventions | 78 |
| BIBLIOGRAPHY | | 82 |

LIST OF TABLES

| | |
|---|----|
| Table 2.1: Typical simulation parameters. | 15 |
| Table 3.1: Simulation parameters (unless otherwise stated); e and a_0 denote the elementary charge and Bohr radius. The decoherence times here, while shorter than those typical of optical resonance experiments, afford a shorter computational time but preserve dynamical emission phenomena. | 31 |
| Table 4.1: Power-law regressions and their coefficients of determination (r^2) for the data in fig. 4.8. Here, t denotes the walltime of the simulation (in seconds) and n the number of spatial basis functions. | 53 |

LIST OF FIGURES

| | |
|---|----|
| Figure 1.1: Comparison of differential-equation and integral-equation methodologies. As both approaches have several advantages and disadvantages, the choice of which technique to use largely depends on the problem under consideration. | 4 |
| Figure 2.1: Coordinate notation. | 10 |
| Figure 2.2: Perpendicular configuration. | 14 |
| Figure 2.3: Translation of a single microsphere interacting with an incident pulse ($f_0 = 0.5 \text{ MHz}$, $\sigma = 7 \mu\text{s}$). Microspheres interacting with the pulse translate a finite distance along \mathbf{k} due to the Gaussian envelope in eq. (2.9). 16 | 16 |
| Figure 2.4: Confinement of non-interacting spheres to planes; identical counter-propagating pulses ($f_0 = 20 \text{ MHz}$, $\sigma = 23.8 \mu\text{s}$) initially displaced along $\hat{\mathbf{z}}$ tend to align objects in $\nabla P = \mathbf{0}$ planes at $\lambda/2$ intervals. Here, we have sampled the field and trajectories every 30 timesteps and smoothed the resulting data with a 16-sample windowed average. . . . | 17 |
| Figure 2.5: Calculated isopotential contours near a lone microsphere. Red and blue colorations represent regions of positive and negative potential. The motion of each microsphere through the background medium serves primarily to produce a dipolar field of velocity potential with \mathbf{v}_s serving as the sphere's dipole moment. | 18 |
| Figure 2.6: Scaling behavior of two microspheres arranged perpendicularly to an incident pulse for various radii and initial separations. The (\blacktriangle , \bullet) symbols on each axis denote data associated with that axis. The \blacktriangle follow a regression of $\Delta \mathbf{v} _d = 0.250754d_{12}^{-3.00077}$, and the \bullet follow $\Delta \mathbf{v}_{\text{max}} _r = 3.13328 \times 10^{-5}a_0^{2.99814}$. These trends strongly indicate dominant dipolar interactions between microspheres. | 19 |
| Figure 2.7: Isosurfaces of velocity potential (arb. units) calculated by evaluating the \hat{S} and \hat{D} terms in eq. (2.8) for a $N = 16$ particle simulation. Red, blue, and yellow surfaces denote regions of positive, negative, and zero potential respectively, with holes appearing due to intersections with the bounding box. Rendered with VisIt[21]. | 20 |

| | | |
|-------------|---|----|
| Figure 2.8: | Fractional change in the volume of 20 randomly-initialized microsphere clouds subject to the same incident pulse, smoothed with a 128-sample moving average. Positive and negative values denote expansion and contraction. $\sigma = 1.5$ cm. | 21 |
| Figure 3.1: | Bloch sphere representation of a two-level quantum system. Equation (3.1) describes the evolution of $ \psi\rangle$ on the surface of this sphere in response to an external electric field. | 25 |
| Figure 3.2: | Nonorthogonal and C^0 -continuous temporal basis function $T(t/\Delta t)$ constructed from intervals of third-order Lagrange polynomials. | 28 |
| Figure 3.3: | Flowchart of one iteration of the coupled quantum/electromagnetic solution procedure. | 30 |
| Figure 3.4: | Comparison of $\rho_{00}(t)$ using both fixed (requiring 59959 timesteps) and rotating (requiring 160 timesteps) reference frames for two interacting quantum dots. Both frames produce similar trajectories, however the inset spy reveals the fixed frame contains a minute oscillatory term that the rotating frame does not. | 32 |
| Figure 3.5: | Population dynamics of adjacent quantum dots (top, shown with the trajectory of a quantum dot driven exclusively by the external laser in black) and a 1024-particle neighborhood (dots (1) and (2) maintain their separation and orientation between simulations). The interaction between particles gives a greatly diminished response to the external pulse through a dynamical detuning of the two-dot system. The majority of the neighboring particles in the 1024-dot system follow trajectories nearly identical to that prescribed by the laser (omitted for clarity); many-dot effects, however, produce significant oscillatory modes in the evolution of selected quantum dots (shown in gray). Note that $\rho_{00}^{(1)}$ and $\rho_{00}^{(2)}$ appear to have <i>two</i> coherent modes in the presence of multiple dots: a high-frequency oscillation between the pair, as well as a low-frequency oscillation of the group about a decaying envelope. | 33 |
| Figure 3.6: | Spatial distribution of $ \tilde{\rho}_{01} $ for 1024 quantum dots as an indicator of polarization. Recorded at $t = 2$ ps relative to the peak of a 1 ps-wide π -pulse, the color and size of each sphere indicates the location of each quantum dot and its polarization. Following a π -pulse, a single quantum dot would have no remnant polarization; here, due to the near-field interactions between particles, clusters of quantum dots remain in highly-polarized states depending on their separation. | 34 |

| | |
|--|----|
| Figure 3.7: Inverse participation ratio (IPR) for the system shown in fig. 3.6. The dashed line indicates the sample time for fig. 3.6. | 34 |
| Figure 3.8: Coloration of $ \tilde{\rho}_{01} $ as an indicator of $ \tilde{\mathbf{P}} $ at $t_1 = -0.05$ ps, $t_2 = 0$ ps, $t_3 = 0.05$ ps, and $t_4 = 0.10$ ps relative to the peak of a 1 ps-wide pulse. 10 000 quantum dots randomly distributed throughout a $0.2 \mu\text{m}$ (radius) \times $4 \mu\text{m}$ cylinder oriented along \mathbf{k}_L demonstrate near-field the effects of fig. 3.5 as distinct, outlying bright/dark quantum dots. Additionally, the size of the system allows for wavelength-scale phenomena that appear here as five standing regions of enhanced polarization. (Note that we model quantum dots as point objects; the size of the spheres here has no physical interpretation.) | 36 |
| Figure 3.9: Coloration of $ \tilde{\rho}_{01} $ for 10 000 quantum dots arranged in a finite planar geometry (in units of λ). The slab displays a prominent polarization pattern 1.25 ps after the peak of a 1 ps pulse. | 37 |
| Figure 3.10: z -distribution of polarization $ \tilde{\rho}_{01} $ for the geometry in fig. 3.8. In each simulation, 10 000 quantum dots had random Gaussian noise (with width parameters of 0.0 meV, 0.2 meV, 0.4 meV and 0.6 meV) added to a resonant $\hbar\omega_0 = 1500$ meV. The induced long-range patterns in the polarization remain for mild detunings $\lesssim 0.5$ meV but have completely washed out at 0.6 meV. Additionally, each simulation displayed the characteristic near-field coupling effects of fig. 3.5 (not visible here). | 38 |
| Figure 4.1: the interaction matrix for $g(\mathbf{r}, t) = \mathbf{r} ^{-1}$ between points randomly distributed throughout a unit cube appears to have very little structure (left). while we cannot fully order the points in three dimensions, we <i>can</i> permute the matrix so as to give points within the same neighborhood adjacent indices. points ordered thusly produce a diagonally-dominant interaction matrix with a hierarchical Toeplitz substructure (right). such structures indicate portions of the matrix have very accurate low-rank approximations that offer the possibility of significant compression. | 43 |
| Figure 4.2: Illustration of the grid structure and related terminology. All of the sources within a box (shown as the central shaded square) map to the same set of expansion points (shown as open circles) indexed relative to \mathbf{r}_{box} | 44 |

| | | |
|-------------|---|----|
| Figure 4.3: | Illustration of the nearfield criterion for a third order expansion ($\gamma = 2$). The dashed line indicates the complete nearfield of the box associated with \mathbf{r}_0 —i.e. all boxes that have an expansion point within Δs of the expansion around \mathbf{r}_0 . Consequently, all of the $\mathbf{s}_\ell(\mathbf{r})$ within the central dark blue square have a pairwise interaction with the $\mathbf{s}_{\ell'}(\mathbf{r})$ inside the dashed box. | 46 |
| Figure 4.4: | Illustration of nearfield corrections between close boxes. Expansions A and B overlap, but only box B lies in the nearfield of box C . The grid-based propagation strategy only remains accurate for distant source/observer pairs. To avoid incurring undue error, we remove the interaction “through the grid” between the BC pair (red line) and replace it with a more accurate “direct” interaction (dashed blue line). The AC pair requires no such treatment as they have well-separated expansion regions. | 47 |
| Figure 4.5: | Spatial expansion pattern for $\mathbf{s}_\ell(\mathbf{r}) = \hat{\mathbf{d}}_\ell \delta(\mathbf{r} - \mathbf{r}_\ell)$ through order five. The numbers on the grid indicate the points added in the equivalent order expansion such that an expansion of order m requires $(m + 1)^3$ grid points. Moreover, increasing the expansion order incorporates new points in such a way as to keep $\mathbf{s}_\ell(\mathbf{r})$ as close to the center of the expansion region as possible. | 48 |
| Figure 4.6: | Polynomial interpolation of $g(x - x_{\text{src}})$ near x_{obs} . Here, the green curve represents the actual $g(x - x_{\text{src}})$ and the dashed black line its approximation. Evaluating the m^{th} -order approximation requires samples of the signal at $m + 1$ grid points surrounding x_{obs} | 51 |
| Figure 4.7: | ℓ_2 error calculation of $g(\mathbf{r} - \mathbf{r}') = e^{ik \mathbf{r}-\mathbf{r}' }/ \mathbf{r} - \mathbf{r}' $ for expansion orders zero through four. For each of the points above, a source and observation box separated by $\Delta \mathbf{r} = 10\lambda \hat{\mathbf{x}} + 10\lambda \hat{\mathbf{y}} + 10\lambda \hat{\mathbf{z}}$ each contain 64 randomly placed points, thus the points within each box all map to identical nodes in the auxiliary grid. The moment-matching expansion scheme dictates that the overall error for an expansion of order m scales as $\mathcal{O}(\Delta s^{m+1})$ | 52 |
| Figure 4.8: | Time to evaluate retarded potential vs. number of spatial basis functions for several system sizes. Simulated on an Intel(R) Core(TM) i5-4690K CPU @ 3.50 GHz. | 53 |

Figure 4.9: Comparison of a Maxwell-Bloch quantum dot simulation with direct (red) and FFT-accelerated (blue) propagation strategies. Here, we show the off-diagonal matrix elements of 25 random quantum dots (out of 1024) as a function of time. The quantum dots experience an incident π -pulse and their interactions induce significant secondary oscillations (see the second-to-last row). The FFT-accelerated algorithm developed here readily captures these effects, making it eminently suitable for large-scale quantum dot simulations. 54

Figure A.1: Hierarchy of the major pieces of QuEST. While a true class diagram would depict the inheritance relationships of the objects that comprise the QuEST library, These blocks *roughly* indicate the interdependence of the program pieces that form QuEST, akin to a class hierarchy (though avid software developers should not take this literally). 62

Figure B.1: Illustration of the “retardation problem” in solving coupled delay differential equations. If $\partial_t x_{\bullet}(t) = f\{(\{x_{\bullet}(t - |\mathbf{r}_{\bullet\bullet}|) + x_{\bullet}(t - |\mathbf{r}_{\bullet\bullet}|))\}$ then determining $x_{\bullet}(t - |\mathbf{r}_{\bullet\bullet}|)$ and $x_{\bullet}(t - |\mathbf{r}_{\bullet\bullet}|)$ requires some sort of interpolation scheme. Evaluating $\partial_t x_{\bullet}(t)$ in hopes of obtaining $x_{\bullet}(t)$ therefore requires knowledge of $x_{\bullet}(t)$. The converse holds as well;—evaluating $\partial_t x_{\bullet}(t)$ requires knowledge of $x_{\bullet}(t)$ which poses problems in evaluating the derivatives simultaneously. The predictor step of the integrator overcomes this issue by providing a stable extrapolation of past quantities to provide a guess value of $x_{\bullet}(t)$ and $x_{\bullet}(t)$ 69

Figure B.2: Selection of the λ_n parameters used in determining the predictor/corrector coefficients. 69

Figure C.1: Chebyshev polynomials $T_0(x)$ through $T_6(x)$. The roots of $T_{m+1}(x)$ give the sample points for an interpolation scheme of order m on the interval $[-1, 1]$ 72

Figure C.2: Interpolation of a pathological function, $f(x) = (1 + 16x^2)^{-1/2}$, using Chebyshev and equally-spaced Lagrange interpolation schemes. Because the Chebyshev scheme clusters sample points in the tails of the interpolation window, it does not suffer from high-order ringing effects (Runge’s phenomenon). 74

CHAPTER 1

INTRO

“Begin at the beginning,” the King said, very gravely, “and go on till you come to the end: then stop.”

—The King of Hearts, *Alice in Wonderland*

As our ability to resolve physical systems grows, so, too, do our demands of the models we build. Unfortunately, we rapidly approach an age where approximate analytic descriptions of physical systems simply cannot recover important features in systems of interest. Substituting *numerical*—i.e. *in silico*—techniques into higher resolution models alleviates this problem somewhat (particularly as computer hardware evolves “below” the model), though the computational overhead of naïve algorithms limits their utility beyond nearly analytic calculations, particularly in multi-scale or multiphysics applications. Computational scientists, then, have a tricky job: they must have expertise in their own domain so as to begin formulating testable hypotheses about the (multi-)physical systems, as well as expertise in “computation” to understand the constraints inherent in exploring such hypotheses numerically.

1.1 Active media

Active media—dynamical systems that couple together through radiative processes—encompass a large class of problems across length and time scales and exhibit behavior fundamentally different from their passive counterparts. These behaviors offer new avenues towards novel device designs, though engineering devices to exploit them presents a considerable challenge. In particular, the underlying dynamical nature of active systems makes them inherently nonlinear, and accounting for these dynamics alongside the radiative coupling requires a multiphysical approach. As such, this thesis primarily concerns itself with the development of computational techniques for use in modeling active systems both

efficiently and accurately with a particular focus on acoustophoresis (acoustically-induced motion) and quantum optics.

1.1.1 Acoustophoresis

The placement of biological material or microscopic objects plays a large role in a number of technological applications related to biosensing [78]. For example, droplet-based microfluidics entails the careful construction, manipulation, and sensing of μL (or smaller) droplets of fluid for myriad lab-on-a-chip applications. Similarly, DNA microarrays employ large numbers of micron-sized spots—each filled with a particular DNA sequence—to perform an experiment on thousands of genes simultaneously. Manipulating individual droplets and fabricating a microarray both require careful placement of apparatus; though, given the small length scale of these problems, conventional manipulation techniques (such as pipetting) become problematic. Instead, researchers require alternative means of precisely controlling the motion of such objects.

Because of their low energy and minimal invasiveness, so-called acoustic tweezers offer an ideal mechanism for precise microscopic positioning in both biological and nonbiological applications. By varying the pressure in the surrounding environment through the precise application of ultrasonic pulses, acoustic tweezers effect acoustophoresis for a variety of purposes including object placement, fractionation [59], and flow shaping. Present models of such systems often fail to account for multiple scattering events or do so only by way of time- or volume-averaged techniques. This poses a significant problem in extremely small systems where such effects necessarily become important. To overcome this, chapter 2 develops the machinery to simulate the motion of an ensemble of hard spheres within a fullwave scattering framework.

1.1.2 Light in disordered media

Disordered nanostructures give rise to striking optical phenomena. *Cyphochilus* spp. beetles, for instance, owe their intense white coloration to an aperiodic arrangement of scales that scatters light across wavelengths [80]. Whereas man-made objects of similar whiteness and intensity require structures as thick as $100\ \mu\text{m}$, the scales of *cyphochilus* spp. can span as few as $4\ \mu\text{m}$ by exploiting an interior structure of disordered filaments. Additional effects such as Anderson localization [5]—wherein light remains spatially confined for extended periods of time—and Lévy flights [10]—in which light experiences superdiffusive, i.e. superlinear (in time), behavior—all follow from similarly disordered structures. Because of their dynamical absorption and emission effects, these phenomena all fall under the broad category of active light/matter interactions.

Quantum dots—colloquially called “tuneable atoms” because of the ease with which engineers can manipulate their spectra—stand as a premier element in modern optoelectronic devices and have enjoyed widespread success in areas such as light harvesting and quantum information storage/retrieval. Because of this, a number of analytic methods based on ensemble-averaged single particle and higher order Green’s functions have arisen to describe light propagation in such systems. These methods essentially cast the active quantum system as a homogeneous continuum source in the governing electromagnetic equations (Maxwell’s equations for semiclassical systems) [6], though such a treatment cannot account for effects arising from long-range order, partial order, or anisotropies. Models of these effects, then, require a detailed computational framework that captures scattering/radiation effects between discrete, disordered elements. In chapter 3 we develop just such a framework; one that eschews a phenomenological treatment of matter, preferring instead to “generate” the constitutive relations that govern the sources in Maxwell’s equations.

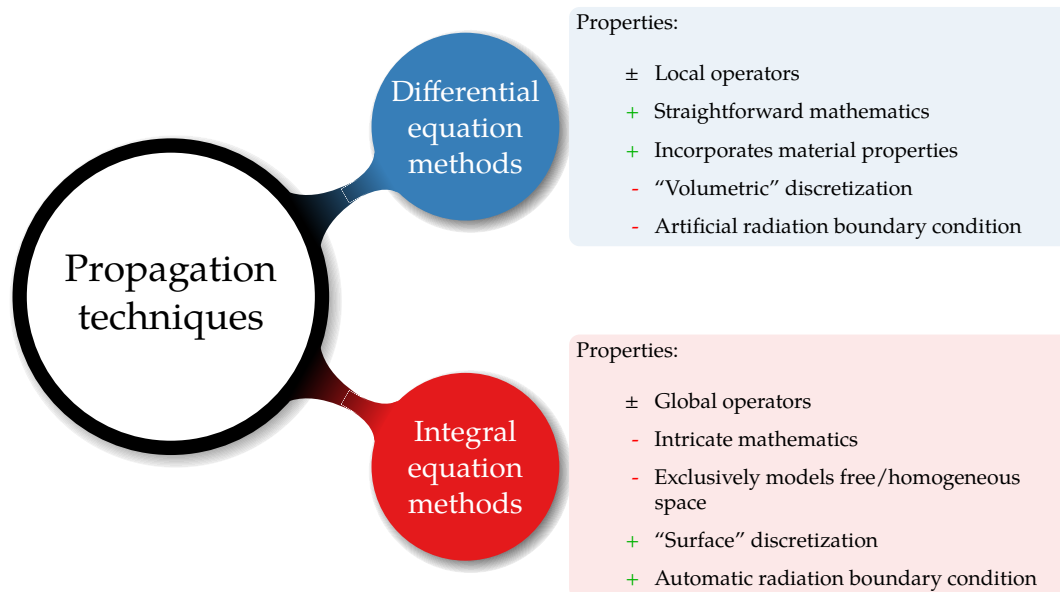


Figure 1.1: Comparison of differential-equation and integral-equation methodologies. As both approaches have several advantages and disadvantages, the choice of which technique to use largely depends on the problem under consideration.

1.2 Numerical simulation of wave propagation

Wave phenomena influence every aspect of our lives across every scale of the universe, thus it should come as little surprise that techniques to explore and analyze these phenomena lie at the heart of many scientific and engineering disciplines. Broadly, these techniques fall into differential-equation-based and integral-equation-based categories with each having several benefits and drawbacks. Differential-equation-based models have a large, sparse character that follows directly from a discretization of the wave equation throughout a volume of interest. Such a volumetric discretization explicitly describes fields within the entirety of the simulation domain and works well to capture cavity effects or effects involving variations in material parameters. Open systems where waves propagate “to infinity” require significant care, however, and employ corrections such as perfectly-matched layers [11] or absorbing boundary conditions [57] to approximate correct asymptotic behavior.

Integral-equation-based methods, on the other hand, remedy many of the problems

associated with differential methods. By employing a Green's function to directly determine the response of interacting sources, these methods automatically capture radiation boundary conditions and eliminate the numerical issues associated with intermediate meshes entirely. These features, however, do not come without cost. Integral-equation methodologies have a great deal more mathematical sophistication than their differential-equation analogues and their discretizations inherently produce dense interaction matrices. The $O(n^2)$ solution cost of these matrices scales poorly for systems with many degrees of freedom, thus a large body of work has emerged to reduce this cost to $O(n^p)$ (where $p < 2$) or even $O(n \log n)$. These so-called "fast methods" exploit the underlying structure of the interaction matrix to develop compressed representations of the interaction between distant sources with fully-controllable numerical error. Because of its accuracy and speed, the development of such a method stands as the principal contribution of chapter 4.

CHAPTER 2

ACOUSTOPHORESIS IN RIGID MICROSPHERES

“Where are you going?”

“Which way should I go?”

“That depends on where you are going.”

“I don’t know.”

“Then it doesn’t matter which way you go.”

—The Cheshire Cat and Alice, *Alice in Wonderland*

2.1 Introduction

Computational approaches that employ an integral equation formalism to examine acoustic scattering from particles typically assume a static environment in which scatterers remain stationary. At present, a large body of work details such scattering problems [81, 24, 83]. While these stationary integral equation methods offer a large degree of accuracy in capturing the underlying physics, many problems of interest require a fully dynamical treatment. For instance, in biomedical physics, gas-filled microspheres exposed to ultrasonic beams have demonstrated effectiveness as a contrast imaging agent [13] and as a drug delivery method [3, 42], and Ding *et al.* have demonstrated their manipulation using acoustic tweezers in microfluidic channels [23]. Moreover, composite materials consisting of colloidal in-fluid suspensions have peculiar sound propagation properties that can deviate from the ones of homogeneous liquids [82]. In each of these applications, the unconstrained motion of scatterers requires a self-consistent description of their dynamics in conjunction with a description of the acoustic field propagation.

Here, we demonstrate the applicability of coupling particle kinetics to a time-domain integral equation (TDIE) scattering framework to model rigid-sphere motion induced by a

time-dependent acoustic potential. Specifically, we consider the case of an acoustic pulse acting on microspheres that move in a fluid. Effective Langevin time-averaged radiation pressure forces [50, 17], which consider the case of a steady radiation flux incident upon a body kept in static equilibrium, do not provide an appropriate model in this case as they cannot accommodate inter-particle scattering effects. While many theoretical and computational descriptions of higher-order acoustic interactions exist [40, 25, 26, 44, 8], few actually make use of computed fields to predict particle trajectories. As we consider only short-duration pulses, we refrain from time-averaging in favor of using a time-domain scattering formulation to explicitly calculate particle trajectories resulting from a prescribed pulse. By adopting a weakly-compressible potential formulation of the fluid media, our scalar wave problem inherits a number of similarities and solution techniques from scattering problems in electromagnetic theory, a topic previous works discuss extensively [77, 40, 54]. Moreover, our time-domain formulation readily allows the study of transient phenomena (such as acoustic tweezing), a convenience not shared with more common frequency domain approaches.

We structure the remainder of this chapter as follows: we first provide a formal mathematical description of the problem—including details on both the kinetic and field methods—followed by data obtained from various pulse and microsphere configurations, demonstrating both attractive and repulsive regimes suitable for subtle control of spherical systems in a homogeneous fluid. Finally, we offer concluding remarks on the effectiveness of the simulation as well as our thoughts on possible future extensions.

2.2 Continuum problem statement

Consider a collection of N rigid, non-intersecting spherical scatterers (microspheres), each having radius a_k , position \mathbf{r}_k , and enclosing volume $V_k \subset \mathbb{R}^3$. The microspheres move in a homogeneous exterior fluid occupying V_E , where we denote the boundary of each microsphere as $\Omega_k = \partial V_k$ and thus may ascribe to each an outward-pointing normal

$\hat{\mathbf{n}}_k(\theta, \phi)$, where θ and ϕ represent colatitude and azimuthal angles with respect to the local origin (microsphere center). We wish to investigate the reaction of the system to an incident acoustic pulse, thus the fluid carries a prescribed (band-limited) waveform through the microsphere system in which it interacts with each of the $\partial\Omega_k$ according to the “sound-hard” regime presented in [54]. The incident acoustic pulse, in combination with the acoustic field scattered from each microsphere and the hydrodynamic field induced by the relative velocity of each microsphere, acts as a perturbation to the initially at-rest uniform ideal fluid [58, 53]. We consider here the linear regime, in which the perturbation induced by the acoustic and aerodynamic contribution remain sufficiently small so that the velocity field $\mathbf{v}(\mathbf{r}, t)$ satisfies the condition $|\mathbf{v}(\mathbf{r}, t)| \ll c_s$, where c_s represents the speed of sound in the fluid. In this limit, the velocity potential, defined by $\mathbf{v}(\mathbf{r}, t) = \nabla\varphi(\mathbf{r}, t)$, satisfies the scalar wave equation:

$$\left(\nabla^2 - \frac{1}{c_s^2} \frac{\partial^2}{\partial t^2}\right)\varphi(\mathbf{r}, t) = 0, \quad (2.1)$$

and we may express the pressure perturbation at any point in the exterior medium as

$$p(\mathbf{r}, t) = -\rho_0 \frac{\partial\varphi(\mathbf{r}, t)}{\partial t}, \quad (2.2)$$

where ρ_0 denotes the equilibrium density of the fluid. Rigidity of the Ω_k necessarily prescribes boundary conditions on the normal velocity components at each interface, namely,

$$\left.\frac{\partial\varphi(\mathbf{r}, t)}{\partial\hat{\mathbf{n}}_k}\right|_{\mathbf{r}\in\Omega_k} = \frac{d\mathbf{r}_k}{dt} \cdot \hat{\mathbf{n}}_k. \quad (2.3)$$

where \mathbf{r}_k represents the center-of-mass coordinate for the k^{th} microsphere.

Using these relations, we apply the Kirchoff-Helmholtz theorem to define the following system of integral equations,

$$\varphi(\mathbf{r}, t) = \varphi_{\text{inc}}(\mathbf{r}, t) + \sum_{i=0}^{N-1} \iint \left(\varphi(\mathbf{r}', t') \frac{\partial g_r(\mathbf{r}, t; \mathbf{r}', t')}{\partial\hat{\mathbf{n}}_k} - g_r(\mathbf{r}, t; \mathbf{r}', t') \frac{\partial\varphi(\mathbf{r}', t')}{\partial\hat{\mathbf{n}}_k} \right) dA' dt', \quad (2.4)$$

where $A' \in \Omega_k(t')$ and $g_r(\mathbf{r}, t; \mathbf{r}', t')$ denotes the Green’s function for a retarded potential,

$$g_r(\mathbf{r}, t; \mathbf{r}', t') = \frac{\delta(t - t' - |\mathbf{r} - \mathbf{r}'|/c_s)}{4\pi|\mathbf{r} - \mathbf{r}'|}. \quad (2.5)$$

If the system remains localized to a region with small dimensions when compared to the wavelength of sound, retardation effects become negligible and we may instead use the Laplace-kernel Green's function,

$$g(\mathbf{r}, \mathbf{r}') = \frac{1}{4\pi|\mathbf{r} - \mathbf{r}'|}. \quad (2.6)$$

To ease notation, we define the following two integral operators,

$$\hat{\mathcal{S}}_k[\varphi(\mathbf{r} \in \Omega_k(t), t)] = \int g(\mathbf{r}, \mathbf{r}') \partial_{\hat{\mathbf{n}}_k} \varphi(\mathbf{r}', t) dA \quad (2.7a)$$

$$\hat{\mathcal{D}}_k[\varphi(\mathbf{r} \in \Omega_k(t), t)] = \int \varphi(\mathbf{r}', t) \partial_{\hat{\mathbf{n}}_k} g(\mathbf{r}, \mathbf{r}') dA, \quad (2.7b)$$

reducing eq. (2.4) to

$$\varphi(\mathbf{r}, t) = \varphi_{\text{inc}} + \sum_{k=0}^{N-1} \left(\hat{\mathcal{D}}_k - \hat{\mathcal{S}}_k \right) [\varphi(\mathbf{r} \in \Omega_k(t), t)]. \quad (2.8)$$

In solving eq. (2.8), we obtain the velocity potential everywhere for a given time without retarded scattered fields. For the incident pulse, φ_{inc} , we consider superpositions of wave packets of the form

$$\varphi_{\text{inc}}(\mathbf{r}, t) = P_0 \cos(\omega_0 t - \mathbf{k} \cdot \mathbf{r}) e^{-(c_s t - \hat{\mathbf{k}} \cdot \mathbf{r})^2 / (2\sigma^2)} \quad (2.9)$$

due to their established spectral properties (i.e. known bandwidth and center frequency). Finally, the variation in pressure (and thus φ) over each of the Ω_k necessarily propels each microsphere according to

$$m_k \frac{d^2 \mathbf{r}_k}{dt^2} = \rho_0 \int \frac{\partial \varphi(\mathbf{r}, t)}{\partial t} d\mathbf{S} \quad (2.10)$$

where \mathbf{S} denotes the outward-pointing normal of $\Omega_k(t)$.

2.3 Discretization of the Integral Equations

To solve the integral equation scattering problem, we begin by discretizing our field in both space and time. As we have restricted our particles to completely spherical geometries,

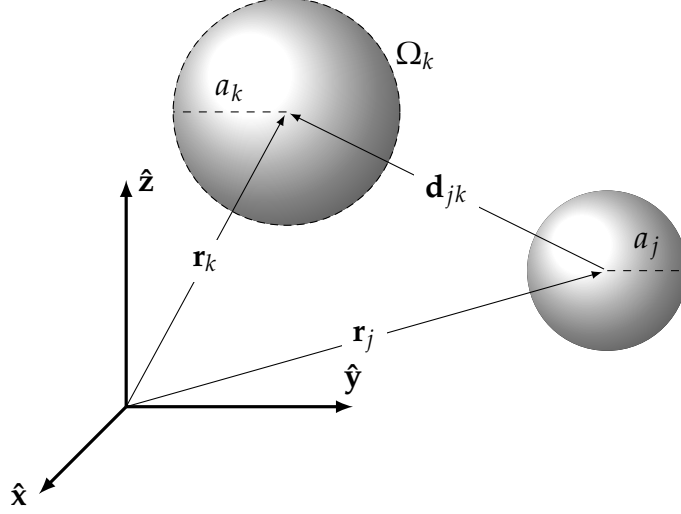


Figure 2.1: Coordinate notation.

the $Y_{\ell m}(\theta, \phi)$ spherical harmonics give simple eigenfunctions of the operators in eq. (2.7) where

$$Y_{\ell m}(\theta, \phi) = \sqrt{\frac{2\ell + 1}{4\pi} \frac{(\ell - m)!}{(\ell + m)!}} P_{\ell}^m(\cos \theta) e^{im\phi}. \quad (2.11)$$

As a result, they lend themselves well to an expansion of φ on the surface of each microsphere with respect to the microsphere's center,

$$\varphi(\mathbf{r} \in \Omega_k, t) = \sum_{\ell \geq 0} \sum_{|m| \leq \ell} C_{\ell m}^k(t) Y_{\ell m}(\theta, \phi). \quad (2.12)$$

By considering eq. (2.2) and expressing the local velocity potential at each of the Ω_k as a linear combination of spherical harmonics, we have a complete representation of the body force acting on each microsphere due to the orthogonality of dipole terms with the rest of the multipoles. Hence,

$$\begin{aligned} \mathbf{F}_{\text{body}}^k(t) &= - \int p(\mathbf{r}, t) d\mathbf{S} \\ &= \rho_0 \sqrt{\frac{2\pi}{3}} r^2 \left([\dot{C}_{11}^k(t) - \dot{C}_{1-1}^k(t)] \hat{\mathbf{x}} + i[\dot{C}_{11}^k(t) + \dot{C}_{1-1}^k(t)] \hat{\mathbf{y}} - \sqrt{2} \dot{C}_{10}^k(t) \hat{\mathbf{z}} \right). \end{aligned} \quad (2.13)$$

The problem then becomes one of solving a system of linear equations that we may compactly represent as

$$\overline{\mathcal{Z}} \cdot \boldsymbol{\varphi} = \mathcal{F}, \quad (2.14)$$

with the overbar denoting a matrix quantity. We define the elements of \mathcal{F} as projections of the incident field onto local spherical harmonics,

$$\mathcal{F}_{\ell m}^k = \int Y_{\ell m}^*(\theta, \phi) \varphi_{\text{inc}}(\mathbf{r}, t) dA, \quad (2.15)$$

and detail $\mathcal{Z}_{\ell m, \ell' m'}^{jk}$ for two cases: $j = k$ and $j \neq k$. In the instances where $j = k$, eq. (2.7) propagates effects of the interaction to every point on a surface sharing a coordinate system with the original, thus the harmonics remain orthogonal and

$$\mathcal{Z}_{\ell m, \ell' m'}^{jj} = \frac{\ell + 1}{2\ell + 1} \delta_{\ell \ell'} \delta_{mm'} \quad (2.16)$$

after exploiting the well-known expansion theorem for eq. (2.6),

$$g(\mathbf{r}, \mathbf{r}') = \sum_{\ell, m} \frac{1}{2\ell + 1} \frac{r_{<}^{\ell}}{r_{>}^{\ell+1}} Y_{\ell m}(\theta, \phi) Y_{\ell m}^*(\theta', \phi') \quad (2.17)$$

where $r_{<} = \min(|\mathbf{r}|, |\mathbf{r}'|)$ and $r_{>} = \max(|\mathbf{r}|, |\mathbf{r}'|)$. A description of the off-diagonal terms where $j \neq k$ proceeds much the same way, though the surface expansions no longer share a local origin, complicating the projections. Translation operators for the spherical harmonics [19, 37] allow analytic expressions for these matrix elements, though we eschew such operators in favor of numerical integration for speed.

Thus, at every timestep of the simulation, the algorithm proceeds as follows: (i) project the incident pulse and surface velocities onto local expansions of spherical harmonics, (ii) propagate scattering effects through space by inverting the operators in eq. (2.8), (iii) project these scattered fields onto local spherical harmonics to give a total representation of φ on each surface, and (iv) move each microsphere according to eq. (2.10) and advance $t \rightarrow t + \Delta t$. Only $\ell = 1$ terms contribute to the center-of-mass motion of rigid microspheres, thus we use the C_{1m} coefficients in evolving eq. (2.10).

The inversion in step (ii) above requires some care; by simply inverting the entire propagation operator, $\hat{\mathcal{D}} - \hat{\mathcal{S}}$, to give a single surface pressure, eq. (2.10) reduces to a differential equation of the form

$$\dot{\mathbf{r}}_k = f(t, \mathbf{r}_k, \dot{\mathbf{r}}_k). \quad (2.18)$$

This presents a number of irregularities with conventional integration schemes and will rapidly diverge towards $\pm\infty$ due to the additional $\dot{\mathbf{r}}_k$ on the right if implemented naïvely. To remedy this, we note that $\hat{\mathcal{S}}$ serves to produce *only* a reaction or drag term on each microsphere that impedes motion. By maintaining quantities for the inversion of $\hat{\mathcal{D}}$ and $\hat{\mathcal{S}}$ separately, we remove the explicit dependence on $\dot{\mathbf{r}}_k$ by introducing a linear coefficient in the form of an additional mass term—given by the $\dot{\mathbf{r}}_k$ -dependent contribution in the single-layer $\hat{\mathcal{S}}$ operator—when solving eq. (2.10).

2.4 Analytic results

2.4.1 Single microsphere solution

As an example, consider a single sphere of density ρ_s and radius a . Taking $ka \ll 1$, we may approximate eq. (2.9) as $\varphi_{\text{inc}}(\mathbf{r}, t) = v_0(t)z$ and we wish to find the response velocity of the sphere, \mathbf{u} , in terms of the field velocity $\mathbf{v} = \nabla\varphi_{\text{inc}}$. It follows that the expansion of φ_{inc} contains only $\ell = 1$ terms, thus

$$\varphi_{\text{inc}} = v_0(t) a \cos(\theta) \quad (2.19)$$

on the surface of the sphere. Similarly, from eq. (2.3),

$$\begin{aligned} \partial_{\hat{\mathbf{n}}}\varphi &= \mathbf{u} \cdot \hat{\mathbf{n}} \\ &= u_z a \cos(\theta) \end{aligned} \quad (2.20)$$

due to the symmetries present in x and y . As a result,

$$\varphi - \int \varphi(\mathbf{r}') \partial_{\hat{\mathbf{n}}'} G(\mathbf{r}, \mathbf{r}') dS' = v_0 a \cos(\theta) - \int a u_z \cos(\theta) G(\mathbf{r}, \mathbf{r}') dS', \quad (2.21)$$

and it becomes apparent that only $\ell = 1, m = 0$ terms in eq. (2.17) remain after integrating. Consequently, the field becomes

$$\varphi(\mathbf{r}, t) = \left(v_0(t)|\mathbf{r}| + \frac{a^3(v_0(t) - u_z)}{2|\mathbf{r}|^2} \right) \cos(\theta) \quad (2.22)$$

outside the microsphere and

$$\varphi(\mathbf{r} \in \Omega, t) = \left(\frac{3}{2}v_0(t) - \frac{1}{2}u_z \right) a \cos(\theta) \quad (2.23)$$

on its surface. From this we conclude the total velocity potential in the fluid arises from a surface-scattering term alongside a term describing the transfer of momentum from the moving microsphere to the fluid.

Using eq. (2.10), we may then write the equation of motion for the system as

$$\rho_s V \dot{u}_z = \rho_0 V \left(\frac{3}{2}\dot{v}_0 - \frac{1}{2}\dot{u}_z \right). \quad (2.24)$$

where $V = 4\pi a^3/3$ gives the volume of the microsphere. The transfer of momentum from the moving microsphere to the fluid becomes a reaction force of the fluid due to the sphere. Landau & Lifshitz [53] initially derived this non-dissipative *drag force* by way of momentum and energy conservation. Note that this drag force presents only in the case of accelerated motion of the microsphere and we may recast its effect in the form of a *virtual mass* that includes a contribution due to the mass of the displaced fluid,

$$\left(\rho_s + \frac{\rho_0}{2} \right) V \dot{u}_z = \frac{3\rho_0 V}{2} \dot{v}_0. \quad (2.25)$$

This expression leads to a simple relation linking $u_z(t)$ and $v_0(t)$ provided that the velocity does not remain constant and that the sphere does not move in the absence of the field:

$$\frac{u_z}{v_0} = \frac{3\rho_0}{\rho_0 + 2\rho_s}. \quad (2.26)$$

The idea of a virtual mass for the accelerated motion of a single sphere in an ideal fluid readily generalizes to the case of a moving collection of mutually-interacting spheres. Through this, we may compute the dynamics of each microsphere in the group, taking into account the effect of the momentum exchange between the fluid and the microspheres. This results in both drag and inter-particle forces in addition to the displacement caused by the driving acoustic field.

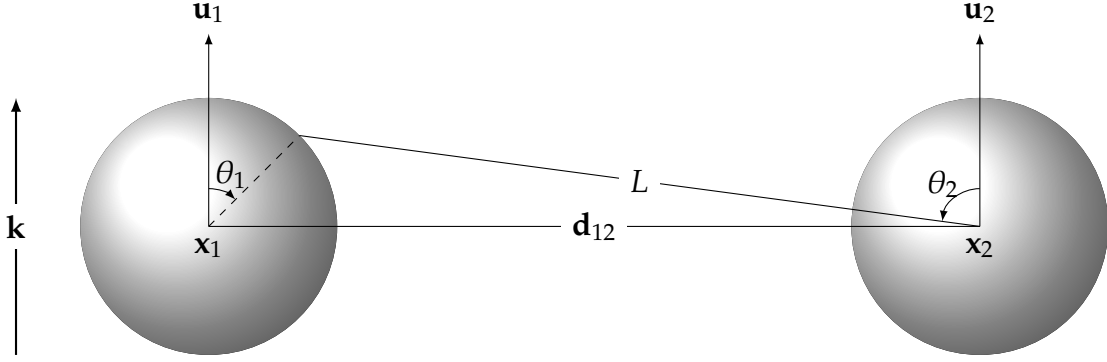


Figure 2.2: Perpendicular configuration.

2.4.2 Low-order interactions

We now consider two identical microspheres arranged perpendicularly to an incident waveform as in fig. 2.2. Within the Born approximation, we may take eq. (2.19) as the incident field and use it in place of the total field on the right-hand side of eq. (2.8), assuming negligible contributions from scattering. In doing so, the field everywhere becomes

$$\varphi(\mathbf{r}, t) = v_0(t)z + \frac{a^3}{3} \frac{\cos(\theta_1)}{|\mathbf{r} - \mathbf{d}_{12}/2|^2} [v_0 - u_1] + \frac{a^3}{3} \frac{\cos(\theta_2)}{|\mathbf{r} + \mathbf{d}_{12}/2|^2} [v_0 - u_2]. \quad (2.27)$$

By inserting this into eq. (2.10) for \mathbf{r}_1 , we have

$$\begin{aligned} m_1 \mathbf{u}_1 \cdot \hat{\mathbf{z}} &= 2\pi\rho_0 a^2 \int \cos^2 \theta_1 a^3 \left(\frac{4}{3} v_0 - \frac{u_1}{3} \right) d(\cos \theta_1) + \\ &\rho_0 \int_{\Omega_1} \frac{a^5}{3} \frac{v_0 - u_2}{|\mathbf{r} - \mathbf{d}_{12}|^2} \cos \theta_1 \cos \theta_2 d\phi_1 d(\cos \theta_1). \end{aligned} \quad (2.28)$$

Writing

$$\cos \theta_2 = \frac{a}{d_{12}} \frac{\cos \theta_1}{\sqrt{\left(1 - \frac{a}{d_{12}} \sin \theta_1\right)^2 + \left(\frac{a}{d_{12}} \cos \theta_1\right)^2}} \quad (2.29)$$

and noting $\mathbf{u}_1 = \mathbf{u}_2 \equiv \mathbf{u}_s$ due to symmetry in the initial configuration, we may expand eq. (2.28) in a/d_{12} to give

$$\rho_s u_s = \rho_0 \left(\frac{4}{3} v_0 - \frac{1}{3} u_s \right) + \frac{\rho_0 (v_0 - u_s)}{3} \left(\frac{a}{d_{12}} \right)^3. \quad (2.30)$$

In the limit of $d_{12} \rightarrow \infty$, this becomes

$$\frac{u_s}{v_0} = \frac{4\rho_0}{\rho_0 + 3\rho_s}. \quad (2.31)$$

| Quantity | Symbol | Value |
|---------------------------|----------|--|
| Sound speed | c_s | 1500 m s^{-1} |
| Microsphere radius | a_k | $1 \text{ }\mu\text{m}$ |
| Density (exterior) | ρ_0 | 1000 kg m^{-3} |
| Density (interior) | ρ_s | 1 kg m^{-3} |
| Pulse amplitude | P_0 | $0.05 \text{ m}^2 \text{ s}^{-1}$ |
| Center frequency | f_0 | $0.5 \text{ MHz to } 20 \text{ MHz}$ |
| Pulse duration (st. dev.) | σ | $7 \text{ }\mu\text{s to } 24 \text{ }\mu\text{s}$ |

Table 2.1: Typical simulation parameters.

By considering negligible scattered fields at the surface of each microsphere, we qualitatively recover eq. (2.27) with different coefficients arising only from the Born approximation. Moreover, the additional interaction term in eq. (2.31) scales as $|\mathbf{d}_{ij}|^{-3}$; a behavior anticipated from the dipolar nature of eq. (2.22).

2.5 Numerical Results

Here we present a series of numerically-solved systems to illustrate the utility of the method in investigating acoustic phenomena. We perform simulations of one- and two-particle/pulse systems to determine the principal particle-field and particle-particle interactions, followed by simulations of larger assemblages of spheres to investigate group phenomena and effects in systems without symmetry. Unless otherwise stated, table 2.1 gives the simulation parameters for each of the following simulations; as our interests lie in hydrodynamic applications, we use material parameters characteristic of water to define our external fluid medium. Similarly, we consider here the case of gas-filled microspheres [13], and therefore set their density much smaller than that of the exterior medium. The acoustic pulses lie in the ultrasonic regime, and the chosen frequency of 20 MHz corresponds to that of typical applications in acoustic microscopy.

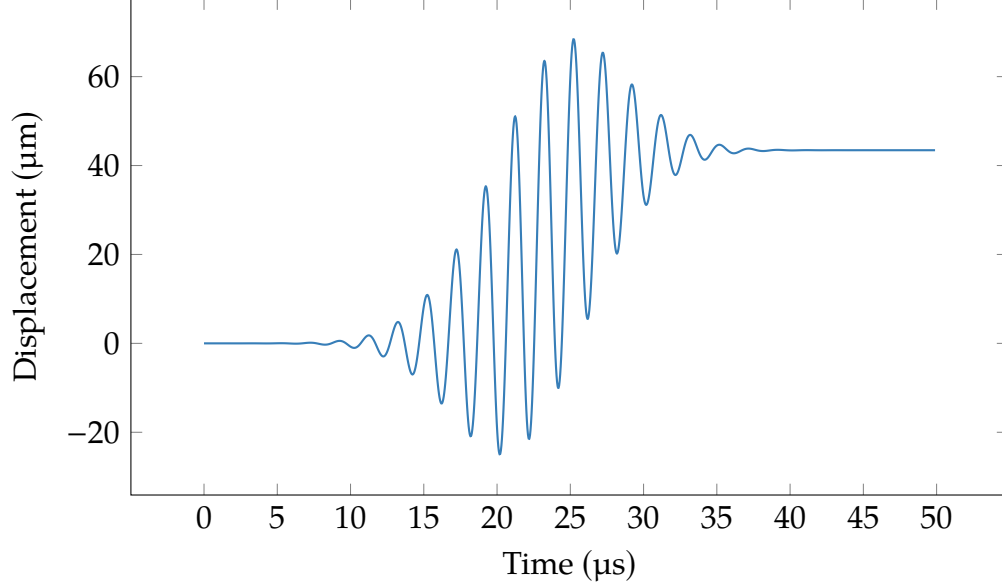


Figure 2.3: Translation of a single microsphere interacting with an incident pulse ($f_0 = 0.5 \text{ MHz}$, $\sigma = 7 \mu\text{s}$). Microspheres interacting with the pulse translate a finite distance along \mathbf{k} due to the Gaussian envelope in eq. (2.9).

2.5.1 Single microspheres

Figure 2.3 gives the trajectory of a single microsphere initially at rest under the effects of an incident Gaussian pulse. Under the linear and ideal fluid approximations and without the Gaussian envelope in eq. (2.9), the microsphere merely oscillates about its origin in accordance with eq. (2.26). In the pulsed case, however, the variation in pressure imposed by the finite value of \mathbf{k} modifies the system dynamics to yield a net translation of each microsphere. Note that the regime considered here produces no net transfer of momentum between the acoustic field and the microsphere—a consequence of the ideal fluid.

Figure 2.4 depicts smoothed results of 128 trajectories corresponding to single microspheres initially spaced along $\hat{\mathbf{z}}$ and excited by identical counter-propagating pulses. By taking the width of each pulse much greater than the radius of each microsphere, the two pulses reproduce the effects of interfering standing waves. The confinement occurs at $\nabla P = \mathbf{0}$ (nodal) planes where the net force on each microsphere vanishes. The half-wavelength associated with the dominant pulse frequency gives the separation between

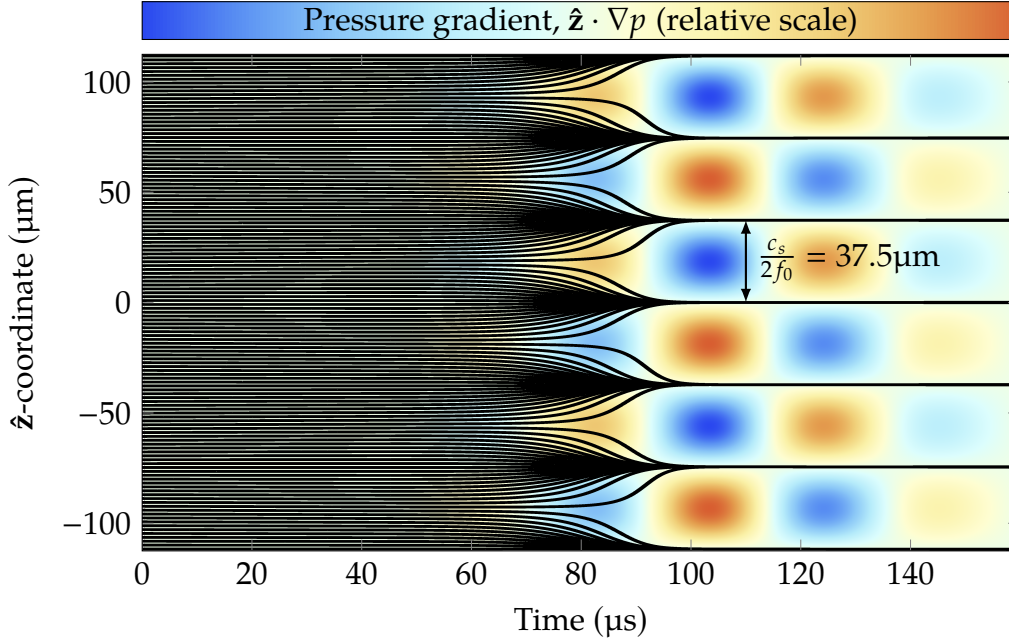


Figure 2.4: Confinement of non-interacting spheres to planes; identical counter-propagating pulses ($f_0 = 20$ MHz, $\sigma = 23.8$ μ s) initially displaced along \hat{z} tend to align objects in $\nabla P = \mathbf{0}$ planes at $\lambda/2$ intervals. Here, we have sampled the field and trajectories every 30 timesteps and smoothed the resulting data with a 16-sample windowed average.

neighboring planes.

Finally, fig. 2.5 shows the relative velocity potential near a single microsphere; given a surface expansion of φ , we may compute the potential everywhere through application of eq. (2.8). As predicted by eq. (2.22), this field greatly resembles that of a pointlike “velocity dipole” with \mathbf{v}_s acting as a dipole moment.

The simulations described thus far demonstrate precise acoustic control; through careful application of the incident field parameters, we may induce a (finite, given a finite pulse) translation along the principal $\hat{\mathbf{k}}$ -vector with a large degree of accuracy in the overall displacement. In addition, the application of multiple pulses serves to confine microspheres to highly localized regions in space, offering a self-consistent model of acoustic tweezing.

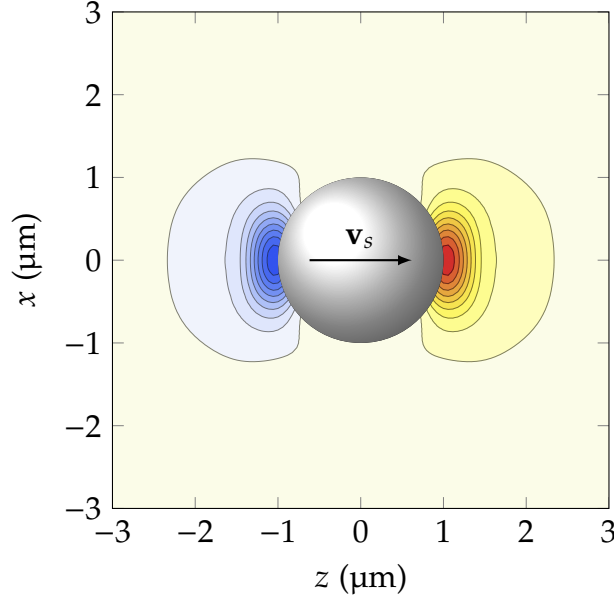


Figure 2.5: Calculated isopotential contours near a lone microsphere. Red and blue colorations represent regions of positive and negative potential. The motion of each microsphere through the background medium serves primarily to produce a dipolar field of velocity potential with \mathbf{v}_s serving as the sphere’s dipole moment.

2.5.2 Many-particle simulations

We now turn our attention to collections of mutually interacting microspheres. To quantify the effects of scattering, we first decouple scattering forces from the incident pulse by arranging two microspheres perpendicularly to the pulse’s \mathbf{k} -vector. Figure 2.6 gives results for such a simulation where we plot the relative change in velocity as compared with the single-particle simulation,

$$\Delta|\mathbf{v}_{\max}| = \max(|\mathbf{v}_{\text{double}}(t) - \mathbf{v}_{\text{single}}(t)|). \quad (2.32)$$

In principle, describing quantities found from a complete simulation as a function of initial separation could obfuscate scaling data considerably; forces arising from scattering could alter the geometry of the system. In practice, however, the perpendicular configuration used here gives scattering forces that only influence the motion along \mathbf{k} . Consequently, $\Delta\mathbf{v} \propto \mathbf{z}$ and the microspheres’ initial separation remains a good estimator of scaling behavior. We see in fig. 2.6 that the radii data scale as a_k^3 and the separation data exhibit strong $|\mathbf{d}_{12}|^{-3}$

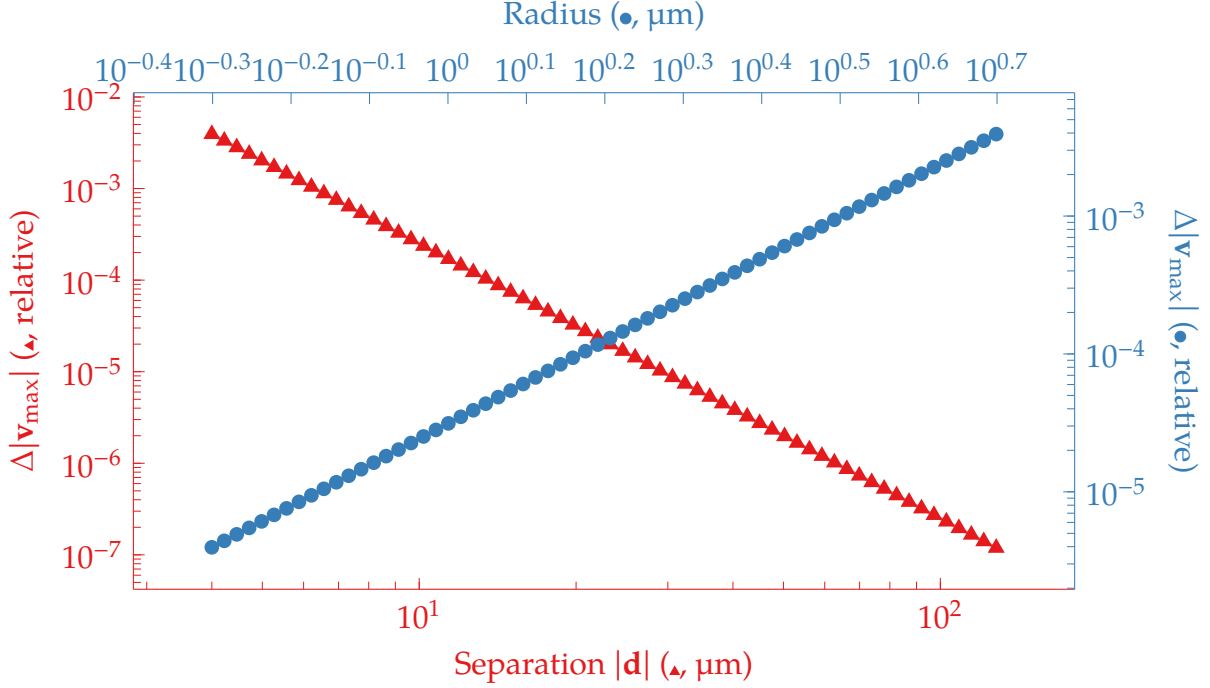


Figure 2.6: Scaling behavior of two microspheres arranged perpendicularly to an incident pulse for various radii and initial separations. The (▲, ●) symbols on each axis denote data associated with that axis. The ▲ follow a regression of $\Delta|\mathbf{v}|_d = 0.250754d_{12}^{-3.00077}$, and the ● follow $\Delta|\mathbf{v}_{\max}|_r = 3.13328 \times 10^{-5}a_0^{2.99814}$. These trends strongly indicate dominant dipolar interactions between microspheres.

scaling, again indicating a dominant dipolar interaction between microspheres as shown by Ilinskii *et al.* in 2007 [44] and predicted by eq. (2.22).

Finally, we consider the dynamics of large ($N = 16$) clouds of microspheres. For each simulation, we generate a collection of microspheres initialized with zero velocity and random positions within a $10 \mu\text{m}$ ball subject to a minimum-separation constraint to prevent collisions. Figure 2.7 shows a snapshot of the velocity potential isosurfaces calculated in one such simulation. Even with mutual interactions, the shape of each isosurface remains consistent with the presence of a dipolar field oriented along the microspheres' velocity. Again, due to the localization assumption used to justify eq. (2.6), each system predominantly translates a finite distance in accordance with the results found for a single microsphere in fig. 2.3. To quantify small changes in the geometry of a system, we compute V_h , the volume of the convex hull containing each microsphere, at every timestep in the

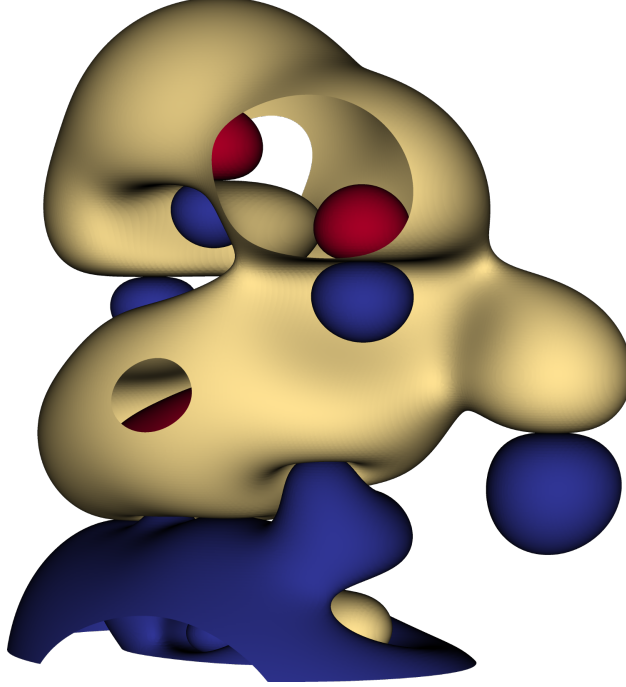


Figure 2.7: Isosurfaces of velocity potential (arb. units) calculated by evaluating the $\hat{\mathcal{S}}$ and $\hat{\mathcal{D}}$ terms in eq. (2.8) for a $N = 16$ particle simulation. Red, blue, and yellow surfaces denote regions of positive, negative, and zero potential respectively, with holes appearing due to intersections with the bounding box. Rendered with VisIt[21].

simulation [47]. Figure 2.8 shows the fractional change in the hull volume,

$$\Delta V_h = \frac{V_h(t) - V_h(0)}{V_h(0)}, \quad (2.33)$$

for 20 such systems after smoothing with a weighted moving average. Curves ending above and below zero indicate larger and smaller hull volumes (system expansion and contraction). We note from fig. 2.8 a greater tendency for random clouds to expand; the effective dipole-dipole interaction between particles with $\mathbf{d}_{ij} \perp \mathbf{k}$ gives purely repulsive forces, while the interaction between particles with $\mathbf{d}_{ij} \parallel \mathbf{k}$ gives both repulsive and attractive effects depending on σ and the relative phase of the oscillating microsphere velocities.

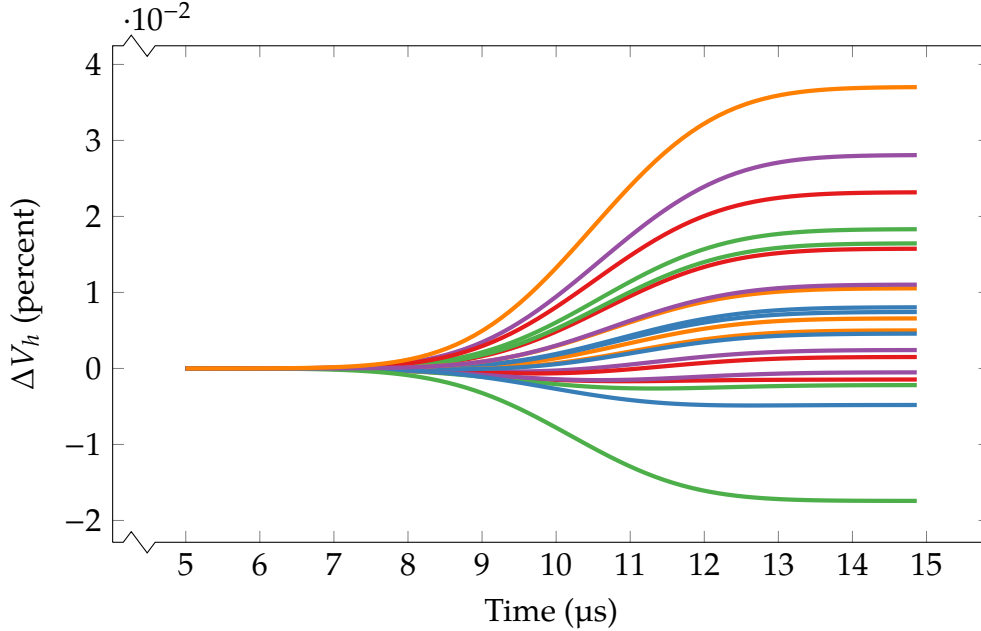


Figure 2.8: Fractional change in the volume of 20 randomly-initialized microsphere clouds subject to the same incident pulse, smoothed with a 128-sample moving average. Positive and negative values denote expansion and contraction. $\sigma = 1.5$ cm.

2.6 Conclusions

This work lends a novel, fine-grained approach to the study of acoustic response via integral equation methods. By considering a potential representation in terms of spherical harmonics on the surfaces of microspheres coupled to a standard molecular dynamics scheme, we obtain a description of the microspheres' dynamics under the effect of ultrasound pulses without resorting to time-average approximations. Furthermore, the confined microsphere geometries under consideration allow us to neglect small effects arising from time-delays in scattering. We have shown that the net effect of an ultrasound pulse on a single microsphere consists of a translation that we can tune through careful control of pulse parameters. Additionally, systems with multiple incident waveforms tend to confine microspheres to nodes in the pressure field governed by acoustic interference. Finally, in the dynamics of systems with many microspheres, we have observed the effect of weak inter-particle transient effects induced by the driving acoustic pulse. These effects can produce both expansion and contraction of a cloud of microspheres, in addition to the

overall translation.

Prior work in this area [85, 75] makes use of deformable bubble boundaries about fixed locations. Incorporation of these methodologies to our theoretical model naturally offers possibilities for future research, as does the addition of retardation effects. Additionally, we expect a straightforward approach to experimental confirmation of the results presented here. Optical tracking of tracer particles[76] has demonstrated its effectiveness in similar fluid-trajectory studies and would readily adapt to track physical analogues of our theoretical microspheres.

CHAPTER 3

RADIATION IN COUPLED QUANTUM DOT SYSTEMS

“But I don’t want to go among mad people,” Alice remarked.

“Oh, you can’t help that,” said the Cat: “we’re all mad here. I’m mad. You’re mad.”

“How do you know I’m mad?” said Alice.

“You must be,” said the Cat, “or you wouldn’t have come here.”

—Alice and the Cheshire Cat, *Alice in Wonderland*

3.1 Introduction

Semiconductor structures containing a large number of quantum dots offer ideal environments for exploring collective effects induced by light-matter interactions. Often, these structures exhibit new phenomena due to geometrical randomness and nonlinearities in the underlying system dynamics. Additionally, optical excitations (excitons) undergo characteristic Rabi oscillations [70, 48, 43] in quantum dots analogous to those observed in atomic systems; because quantum dots have stronger dipolar transitions than atoms, these light-induced oscillations generate secondary fields that couple the system more strongly than equivalent atomic species. We can therefore expect—at least in some regions of the sample—these local secondary fields will produce modified collective behavior in the exciton dynamics. Phenomena induced by these secondary fields have received considerable theoretical/computational [69, 68] and experimental [7] attention as they may provide new insight on the coherent dynamics of excitons in quantum dot systems.

In the realm of theoretical/computational investigation, researchers in atomic and solid-state optics have developed numerous variations of the Maxwell-Bloch equations [38] to describe features such as ringing in pulse propagation [18, 55] or emission fluctuations [41]. Early solution strategies for these equations fell to continuum models [63, 55] that recover

effects arising from far-field interactions or describe near-field phenomena assuming spatial homogeneity [71]. More recently, mesh-based PDE solvers [79, 30, 9] added a large degree of fidelity to these models, though the finite size of the mesh means they still struggle to resolve short-range effects without unduly increasing the computational cost. Additionally, the nature of these meshes makes them prohibitively expensive to extend into higher dimensional geometries for optically-large systems. In this work we develop a computational framework to discover signatures of collective effects in strongly-driven quantum dots within a microscopic formalism. By constructing the Maxwell-Bloch equations with an integral kernel to describe radiation, we recover near- and far-electric fields with full fidelity across the simulation while allowing for dynamics at the level of individual quantum dots. Our methodology—based on successful models of other electromagnetic [67, 61, 60] and acoustic [28, 29, 36] systems—accommodates 10^4 particles distributed over optically-large regions in three dimensions.

As we explicitly track the evolution of each quantum dot in the system, we will numerically demonstrate that the collective Rabi oscillation can induce significant coupling in sufficiently close quantum dots. This laser-induced inter-dot coupling manifests itself in different forms: (i) The polarization generated in isolated quantum dot pairs dynamically suppresses the Rabi rotation. We interpret this as the consequence of a time-dependent energy shift that brings the pair temporarily out of resonance with the external driving field. (ii) In addition to this screening, we observe oscillations in the free-induction decay for larger multiplets of quantum dots. (iii) Optical pulses of integer π area, for which we expect no polarization in uncoupled systems following the pulse, produce patterns of residual localized polarization that remain in the system. (iv) The long-range interactions in optically-large systems produce wavelength-scale regions of enhanced and suppressed polarization. These effects could, for instance, help identify multiplets of dots that dynamically couple during Rabi oscillations, or help understand nonlinear pulse propagation effects in these media.

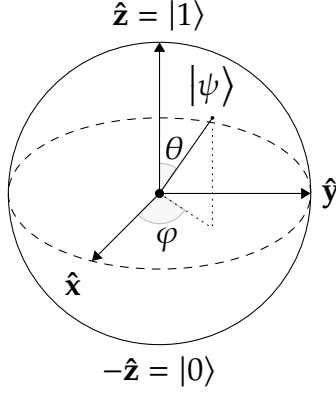


Figure 3.1: Bloch sphere representation of a two-level quantum system. Equation (3.1) describes the evolution of $|\psi\rangle$ on the surface of this sphere in response to an external electric field.

We structure the remainder of this chapter as follows: section 3.2 motivates the physical model of an ensemble of two-level systems that interact through a classical electric field. Section 3.3 presents the details of our methodology in the context of a global rotating-wave approximation and we offer an implementation of this algorithm at [34]. Section 3.4 contains the results of our investigation where we observe polarization features not present in noninteracting systems at both sub- and super-wavelength scales. Finally, section 3.5 contains concluding remarks where we hypothesize on the mechanisms underpinning the observed polarization features as well as comment on our future work in this area.

3.2 Problem Statement

Consider the evolution of a set of quantum dots in response to a time-varying electric field. If we concern ourselves only with electric dipole transitions in a resonant (or nearly-resonant) system, we may write the time-dependence of a given quantum dot's density matrix, $\hat{\rho}(t)$, as

$$\frac{d\hat{\rho}}{dt} = \frac{-i}{\hbar} [\hat{\mathcal{H}}(t), \hat{\rho}] - \hat{\mathcal{D}}[\hat{\rho}]. \quad (3.1)$$

As we wish to investigate two-level systems, $\hat{\rho}(t)$ contains three unique unknowns (ρ_{00} and the real and imaginary parts of ρ_{01}) that describe point on the Bloch sphere (fig. 3.1), $\hat{\mathcal{H}}(t)$ represents a local Hamiltonian that governs the internal two-level structure of the

quantum dot, as well as its interaction with an external electromagnetic field, and $\hat{\mathcal{D}}$ provides dissipation terms that account for emission effects phenomenologically. Formally,

$$\hat{\mathcal{H}}(t) \equiv \begin{pmatrix} 0 & \hbar\chi(t) \\ \hbar\chi^*(t) & \hbar\omega_0 \end{pmatrix} \quad (3.2a)$$

$$\hat{\mathcal{D}}[\hat{\rho}] \equiv \begin{pmatrix} (\rho_{00} - 1)/T_1 & \rho_{01}/T_2 \\ \rho_{10}/T_2 & \rho_{11}/T_1 \end{pmatrix} \quad (3.2b)$$

where $\chi(t) \equiv \mathbf{d} \cdot \hat{\mathbf{E}}(\mathbf{r}, t)/\hbar$, $\mathbf{d} \equiv \langle 1|e\hat{\mathbf{r}}|0\rangle$, and $|0\rangle$ & $|1\rangle$ represent the highest valence and lowest conduction states of the quantum dot under consideration. Finally, the T_1 and T_2 constants characterize average emission and relaxation times.

To account for the interactions between quantum dots, we turn to a semiclassical description of the system under the assumption of coherent fields and negligible quantum statistics effects. Such an approximation preserves the discrete two-level energy structure of *individual* quantum dots though electromagnetic quantities behave like their classical analogues. We define the total electric field at any point as $\mathbf{E}(\mathbf{r}, t) = \mathbf{E}_L(\mathbf{r}, t) + \mathfrak{F}\{\mathbf{P}(\mathbf{r}, t)\}$ where $\mathbf{E}_L(\mathbf{r}, t)$ describes an incident laser field, $\mathbf{P}(\mathbf{r}, t)$ a polarization distribution arising from the off-diagonal elements (coherences) of $\hat{\rho}$, and

$$\mathfrak{F}\{\mathbf{P}(\mathbf{r}, t)\} \equiv \frac{-1}{4\pi\epsilon} \int (\mathbf{I} - \bar{\mathbf{r}}\otimes\bar{\mathbf{r}}) \cdot \frac{\partial_t^2 \mathbf{P}(\mathbf{r}', t_R)}{c^2|\mathbf{r} - \mathbf{r}'|} + (\mathbf{I} - 3\bar{\mathbf{r}}\otimes\bar{\mathbf{r}}) \cdot \left(\frac{\partial_t \mathbf{P}(\mathbf{r}', t_R)}{c|\mathbf{r} - \mathbf{r}'|^2} + \frac{\mathbf{P}(\mathbf{r}', t_R)}{|\mathbf{r} - \mathbf{r}'|^3} \right) d^3\mathbf{r}' \quad (3.3)$$

(see [53, section §72] or section D.2.1). Here, \mathbf{I} denotes the identity dyad, $\bar{\mathbf{r}} \equiv (\mathbf{r} - \mathbf{r}')/|\mathbf{r} - \mathbf{r}'|$, \otimes represents the tensor product (i.e. $(\mathbf{a}\otimes\mathbf{b})_{ij} = a_i b_j$), $t_R \equiv t - |\mathbf{r} - \mathbf{r}'|/c$, and ϵ gives the dielectric constant of the inter-dot medium. Thus, in a system composed of multiple quantum dots, eq. (3.3) couples the evolution of each quantum dot by way of the off-diagonal matrix elements appearing in eq. (3.2a). Note that this approach does not require an instantaneous dipole-dipole Coulomb term between (charge-neutral) quantum dots; the interactions between structures occur only via the electric field which propagates through space with finite velocity. (See [22, sections A_{IV} and C_{IV}] for in-depth discussions of this point.)

In the systems under consideration here, ω_0 lies in the optical frequency band ($\sim 1500 \text{ meV}/\hbar$). As such, naively integrating eq. (3.1) to resolve the Rabi dynamics that occur on the order of 1 ps becomes computationally infeasible. By introducing $\tilde{\rho} = \hat{U}\rho\hat{U}^\dagger$ where $\hat{U} = \text{diag}(1, e^{i\omega_L t})$, we may instead write eq. (3.1) as

$$\frac{d\tilde{\rho}}{dt} = \frac{-i}{\hbar} [\hat{U}\hat{\mathcal{H}}\hat{U}^\dagger - i\hbar\hat{V}, \tilde{\rho}] - \hat{\mathcal{D}}[\tilde{\rho}], \quad \hat{V} \equiv \hat{U} \frac{d\hat{U}^\dagger}{dt} \quad (3.4)$$

which will contain only terms proportional to $e^{i(\omega_0 \pm \omega_L)t}$ if $\mathbf{E}(t) \sim \tilde{\mathbf{E}}(t) \cos(\omega_L t)$. Consequently, we ignore the high-frequency quantities under the assumption that such terms will integrate to zero in solving eq. (3.4) over appreciable timescales [4]. Because the system no longer contains any optical frequencies, one can then construct efficient numerical strategies for solving eq. (3.4).

Due to the quantum mechanical transitions at play in producing secondary radiation, we may assume similarly monochromatic radiated fields. As such, a similar transformation applies to the source distribution in eq. (3.3). Writing $\mathbf{P}(\mathbf{r}, t) = \tilde{\mathbf{P}}(\mathbf{r}, t)e^{i\omega_L t}$ and similarly ignoring high-frequency terms, the radiated field envelope becomes

$$\begin{aligned} \tilde{\mathfrak{F}}\{\tilde{\mathbf{P}}(\mathbf{r}, t)\} \equiv & \frac{-1}{4\pi\epsilon} \int (\mathbf{I} - \bar{\mathbf{r}}\otimes\bar{\mathbf{r}}) \cdot \frac{(\partial_t^2 \tilde{\mathbf{P}}(\mathbf{r}', t_R) + 2i\omega_L \partial_t \tilde{\mathbf{P}}(\mathbf{r}', t_R) - \omega_L^2 \tilde{\mathbf{P}}(\mathbf{r}', t_R)) e^{-i\omega_L |\mathbf{r}-\mathbf{r}'|/c}}{c^2 |\mathbf{r}-\mathbf{r}'|} + \\ & (\mathbf{I} - 3\bar{\mathbf{r}}\otimes\bar{\mathbf{r}}) \cdot \frac{(\partial_t \tilde{\mathbf{P}}(\mathbf{r}', t_R) + i\omega_L \tilde{\mathbf{P}}(\mathbf{r}', t_R)) e^{-i\omega_L |\mathbf{r}-\mathbf{r}'|/c}}{c |\mathbf{r}-\mathbf{r}'|^2} + (\mathbf{I} - 3\bar{\mathbf{r}}\otimes\bar{\mathbf{r}}) \cdot \frac{\tilde{\mathbf{P}}(\mathbf{r}', t_R) e^{-i\omega_L |\mathbf{r}-\mathbf{r}'|/c}}{|\mathbf{r}-\mathbf{r}'|^3} d^3\mathbf{r}'. \end{aligned} \quad (3.5)$$

Critically, eq. (3.5) maintains the high-frequency phase relationship between sources oscillating at ω_L via the factors of $e^{-i\omega_L |\mathbf{r}-\mathbf{r}'|/c}$ that appear.

3.3 Computational Approach

To solve eqs. (3.4) and (3.5) for each of N_s quantum dots at N_t equally-spaced timesteps, we begin with a suitable representation of $\tilde{\mathbf{P}}(\mathbf{r}, t)$ in terms of spatial and temporal basis functions, i.e.

$$\tilde{\mathbf{P}}(\mathbf{r}, t) = \sum_{\ell=0}^{N_s-1} \sum_{m=0}^{N_t-1} \tilde{\mathcal{A}}_\ell^{(m)} \mathbf{S}_\ell(\mathbf{r}) T(t - m \Delta t). \quad (3.6)$$

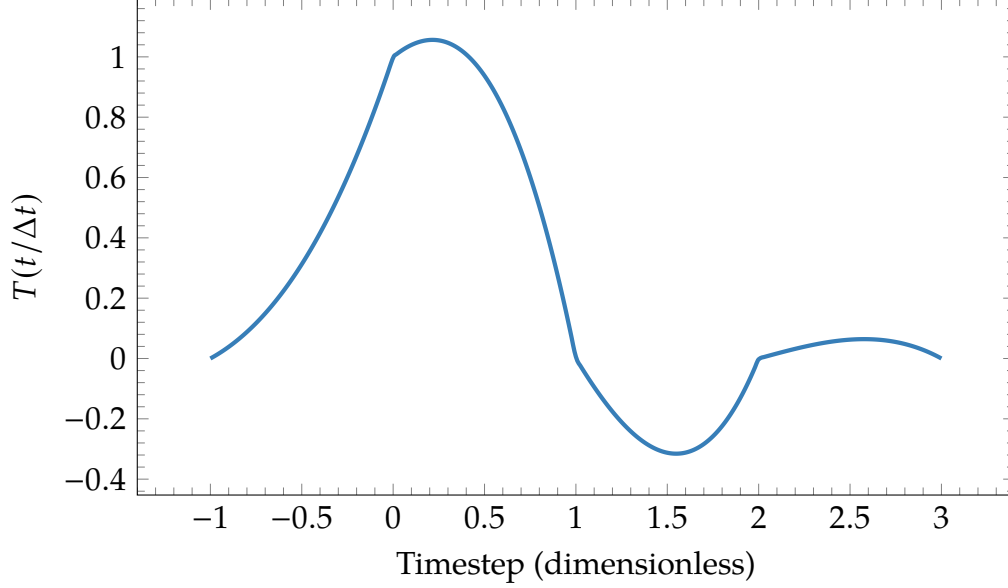


Figure 3.2: Nonorthogonal and C^0 -continuous temporal basis function $T(t/\Delta t)$ constructed from intervals of third-order Lagrange polynomials.

As the wavelength of any radiation in the system far exceeds the dimensions of the quantum dots under consideration, we take $\mathbf{S}_\ell(\mathbf{r}) \equiv \mathbf{d}_\ell \delta(\mathbf{r} - \mathbf{r}_\ell)$ where \mathbf{d}_ℓ and \mathbf{r}_ℓ denote the dipole moment and position of dot ℓ . Furthermore, we require the $T(t)$ to have finite support as well as causal and interpolatory properties so as to recover $\tilde{\mathbf{P}}$, $\partial_t \tilde{\mathbf{P}}$, and $\partial_t^2 \tilde{\mathbf{P}}$ at every timestep. Accordingly, we have elected to use

$$T(t) = \sum_{j=0}^p \lambda_j(t) \quad (3.7)$$

where

$$\lambda_j(t) = \begin{cases} \frac{(1-\tau)_j}{j!} \frac{(1+\tau)_{p-j}}{(p-j)!} & j-1 \leq \tau < j \\ 0 & \text{otherwise,} \end{cases} \quad (3.8)$$

$(a)_k \equiv \Gamma(a+k)/\Gamma(a)$ denotes the Pochhammer rising factorial, and $\tau \equiv t/\Delta t$. Such a $T(t)$ consists of shifted, backwards-looking Lagrange polynomials of order p (we require $p \geq 3$ to recover a twice-differentiable function), forming a temporal basis set with functions similar to the one shown in fig. 3.2. These functions reliably interpolate smooth functions with controllable error and have a long history of use in studies of radiative systems [56, 14].

Combining eqs. (3.5) and (3.6) and projecting the resulting field onto the spatiotemporal basis functions produces a marching-on-in-time system of the form

$$\tilde{\mathcal{L}}^{(m)} + \sum_{k=0}^m \tilde{\mathcal{Z}}^{(k)} \tilde{\mathcal{A}}^{(m-k)} = \tilde{\mathcal{F}}^{(m)}. \quad (3.9)$$

In this (block $N_s \times N_s$) matrix equation

$$\tilde{\mathcal{L}}_\ell^{(m)} = \langle \mathbf{S}_\ell(\mathbf{r}), \tilde{\mathbf{E}}_L(\mathbf{r}, m \Delta t) \rangle \quad (3.10a)$$

$$\tilde{\mathcal{Z}}_{\ell\ell'}^{(k)} = \langle \mathbf{S}_\ell(\mathbf{r}), \tilde{\mathfrak{F}}\{\mathbf{S}_{\ell'}(\mathbf{r})T(k \Delta t)\} \rangle \quad (3.10b)$$

$$\tilde{\mathcal{F}}_\ell^{(m)} = \langle \mathbf{S}_\ell(\mathbf{r}), \tilde{\mathbf{E}}(\mathbf{r}, m \Delta t) \rangle \quad (3.10c)$$

where $\langle \cdot, \cdot \rangle$ denotes the scalar product of two functions. As we have elected to use a uniform Δt , the summation in eq. (3.9) represents a discrete convolution that will produce $\tilde{\mathcal{F}}^{(m)}$ given only $\tilde{\mathcal{A}}^{(m' \leq m)}$. To link $\tilde{\mathcal{A}}^{(m)}$ with the density matrix in eq. (3.4), we take

$$\tilde{\mathcal{A}}_\ell^{(m)} \equiv \tilde{\rho}_{\ell,01}(t = m \Delta t) \quad (3.11)$$

as the off-diagonal matrix elements (coherences) of $\tilde{\rho}_\ell$ directly characterize the dipole radiating at \mathbf{r}_ℓ under the rotating-wave approximation. Consequently, determining $\tilde{\mathcal{A}}^{(m+1)}$ amounts to integrating eq. (3.4) from $t_i = m \Delta t$ to $t_f = (m + 1) \Delta t$ for every quantum dot in the system. For this, we make use of the predictor/corrector scheme detailed in [33]. Defining $t_m \equiv m \Delta t$ and approximating $\tilde{\rho}(t)$ as a weighted sum of complex exponentials, the predictor/corrector scheme proceeds with an extrapolation predictor step,

$$\tilde{\rho}_\ell(t_{m+1}) \leftarrow \sum_{w=0}^{W-1} \mathcal{P}_w^{(0)} \tilde{\rho}_\ell(t_{m-w}) + \mathcal{P}_w^{(1)} \partial_t \tilde{\rho}_\ell(t_{m-w}), \quad (3.12)$$

and iterated corrector steps¹,

$$\tilde{\rho}_\ell(t_{m+1}) \leftarrow \sum_{w=-1}^{W-1} \mathcal{C}_w^{(0)} \tilde{\rho}_\ell(t_{m-w}) + \mathcal{C}_w^{(1)} \partial_t \tilde{\rho}_\ell(t_{m-w}) \quad (3.13)$$

¹The arrow in these operations denotes an operation akin to assignment; this prediction/correction does not *define* $x(t_W)$, only the steps of an iteration that will converge on $x(t_W)$ (or an approximation thereof).

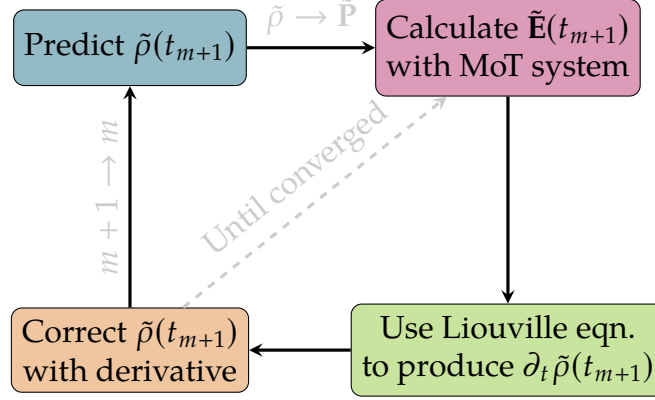


Figure 3.3: Flowchart of one iteration of the coupled quantum/electromagnetic solution procedure.

($C_{-1}^{(0)} \equiv 0$ by construction) to advance the system by Δt . Such an integrator has significantly better convergence properties than Runge-Kutta integrators for equations of the type seen in eq. (3.4) and naturally accommodates basis functions within $c \Delta t$ of each other. (See appendix B for an in-depth discussion of this point.)

Figure 3.3 illustrates these computational steps. In short,

1. At timestep m , use eqs. (3.11) and (3.12) to predict $\tilde{\mathcal{A}}^{(m+1)}$. This prediction depends only on the known history of the system and does not require the calculation of any electromagnetic interactions.
2. Use eq. (3.9) to calculate $\tilde{\mathcal{F}}^{(m+1)}$. Having extrapolated $\tilde{\mathcal{A}}^{(m+1)}$ in step 1, $\tilde{\mathcal{F}}^{(m+1)}$ will contain information from quantum dots within $c \Delta t$ of each other.
3. Produce $\partial_t \tilde{\rho}(t_{m+1})$ (and thus $\partial_t \tilde{\mathcal{A}}^{(m+1)}$) by evaluating eq. (3.4) with the $\tilde{\mathcal{F}}^{(m+1)}$ found in step 2.
4. Correct $\tilde{\mathcal{A}}^{(m+1)}$ with eq. (3.13) and $\partial_t \tilde{\mathcal{A}}^{(m+1)}$ found in step 3. Repeat steps 2 through 4 until $\tilde{\mathcal{A}}^{(m+1)}$ has sufficiently converged, then set $m \leftarrow m + 1$.

| Quantity | Symbol | Value |
|--------------------------|-------------------|--|
| Speed of light | c | $300 \mu\text{m ps}^{-1}$ |
| Transition frequency | ω_0 | $1500 \text{ meV}/\hbar$ |
| Transition dipole moment | \mathbf{d} | $10 e a_0$ (uniform) |
| Decoherence times | T_1, T_2 | 10 ps and 20 ps |
| Laser frequency | ω_L | $1500 \text{ meV}/\hbar$ |
| Laser wavevector | \mathbf{k}_L | ω_L/c ($\mathbf{k}_L \cdot \mathbf{d} = 0$) |
| Pulse width | σ/ω_L | 1 ps |
| Pulse area | – | π |

Table 3.1: Simulation parameters (unless otherwise stated); e and a_0 denote the elementary charge and Bohr radius. The decoherence times here, while shorter than those typical of optical resonance experiments, afford a shorter computational time but preserve dynamical emission phenomena.

3.4 Numerical Results

Here we detail the results of investigations into coupled quantum dot behavior with the model presented thus far. Our algorithm reliably handles tens of thousands of quantum dots and can simulate ten picoseconds of system dynamics in two days on a single processor. We perform simulations of systems of quantum dots randomly distributed throughout a simulation volume experiencing a laser pulse of the form

$$\tilde{\mathbf{E}}_L(\mathbf{r}, t) = \tilde{\mathbf{E}}_0 e^{-(\mathbf{k}_L \cdot \mathbf{r} - \omega_L t)^2 / (2\sigma^2)}. \quad (3.14)$$

Table 3.1 provides the physical system parameters unless otherwise stated.

3.4.1 Stability & adjacency effects

Figure 3.5 details $\rho_{00}(t)$ for two-, and 1024-particle simulations shown against a solution of eq. (3.4) for a quantum dot evolving according to $\tilde{\mathbf{E}}_L(\mathbf{r}, t)$ alone. The system in fig. 3.5(a) contains two quantum dots with a separation of 6.3 nm perpendicular to their mutual \mathbf{d} to ensure large contributions from the near-field term of eq. (3.5). The two quantum dots in this system follow the same trajectory and both excite far less than either would in response to the incident laser alone. These signatures indicate the effect arises as a dynamical frequency shift that brings adjacent quantum dots out of resonance with the

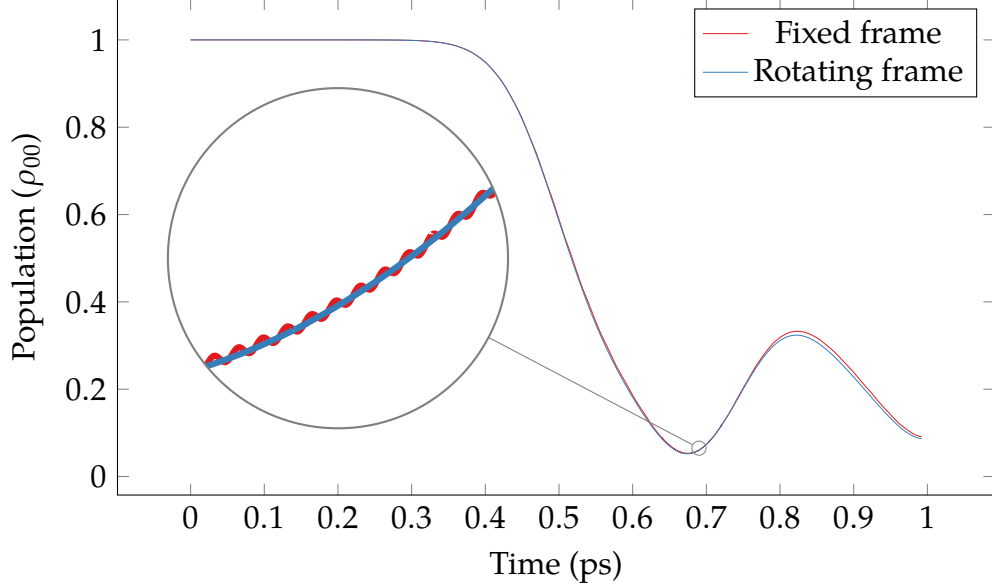


Figure 3.4: Comparison of $\rho_{00}(t)$ using both fixed (requiring 59959 timesteps) and rotating (requiring 160 timesteps) reference frames for two interacting quantum dots. Both frames produce similar trajectories, however the inset spy reveals the fixed frame contains a minute oscillatory term that the rotating frame does not.

applied electric field. We note that this suppression effect occurred to varying degrees for all near-field arrangements of two quantum dots that we investigated. In fig. 3.5(b), the system contains the same two-dot arrangement as in (a), however we have added an additional 1024 quantum dots randomly distributed throughout a $6.4 \times 10^{-2} \mu\text{m}^3$ cube centered around the original pair. Most of these additional quantum dot populations deviate little from those produced by the laser-only pulse due to the large separation between particles. Nevertheless, as we have filled the cube randomly, some regions of the system contain localized clusters of quantum dots that produce the suppression effect detailed above (for two adjacent particles) or populations with higher frequency oscillations (in the case of clusters with three or more quantum dots). Specifically, the two “original” quantum dots acquire an out-of-phase oscillation with respect to each other as well as a lower frequency in-phase oscillation of the pair about a decaying envelope.

Figure 3.6 further illustrates the near-field coupling between quantum dots. Here, 1024 quantum dots randomly fill an $8 \times 10^{-3} \mu\text{m}^3$ cube and the same 1 ps Gaussian π -pulse

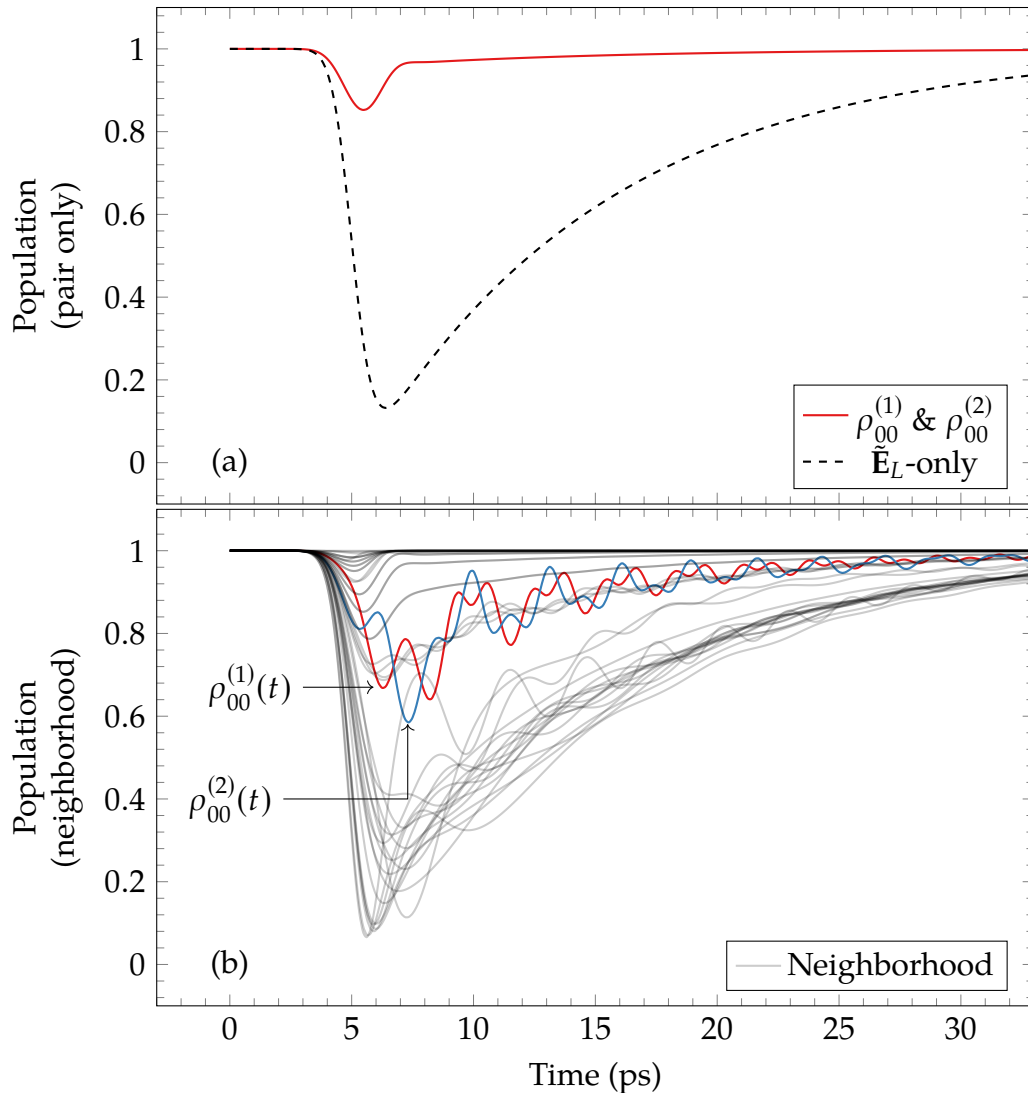


Figure 3.5: Population dynamics of adjacent quantum dots (top, shown with the trajectory of a quantum dot driven exclusively by the external laser in black) and a 1024-particle neighborhood (dots (1) and (2) maintain their separation and orientation between simulations). The interaction between particles gives a greatly diminished response to the external pulse through a dynamical detuning of the two-dot system. The majority of the neighboring particles in the 1024-dot system follow trajectories nearly identical to that prescribed by the laser (omitted for clarity); many-dot effects, however, produce significant oscillatory modes in the evolution of selected quantum dots (shown in gray). Note that $\rho_{00}^{(1)}$ and $\rho_{00}^{(2)}$ appear to have *two* coherent modes in the presence of multiple dots: a high-frequency oscillation between the pair, as well as a low-frequency oscillation of the group about a decaying envelope.

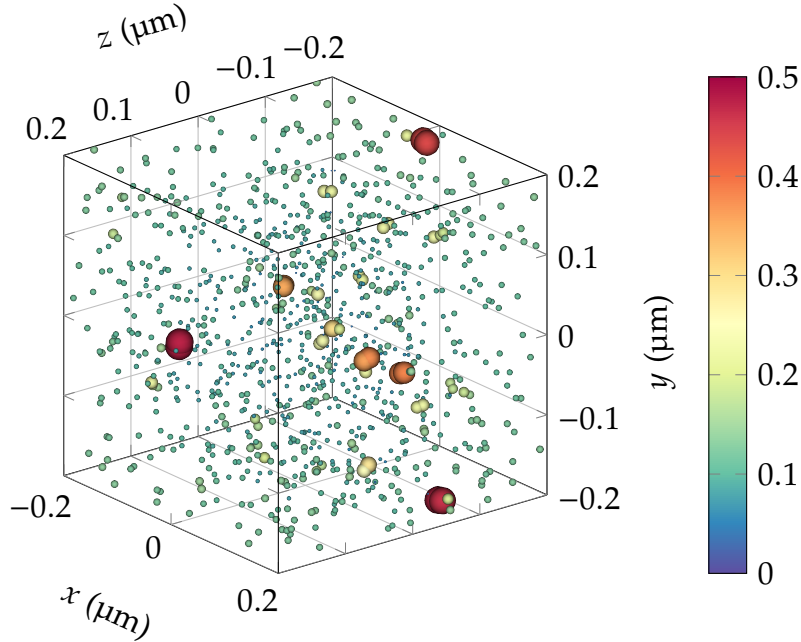


Figure 3.6: Spatial distribution of $|\tilde{\rho}_{01}|$ for 1024 quantum dots as an indicator of polarization. Recorded at $t = 2$ ps relative to the peak of a 1 ps-wide π -pulse, the color and size of each sphere indicates the location of each quantum dot and its polarization. Following a π -pulse, a single quantum dot would have no remnant polarization; here, due to the near-field interactions between particles, clusters of quantum dots remain in highly-polarized states depending on their separation.

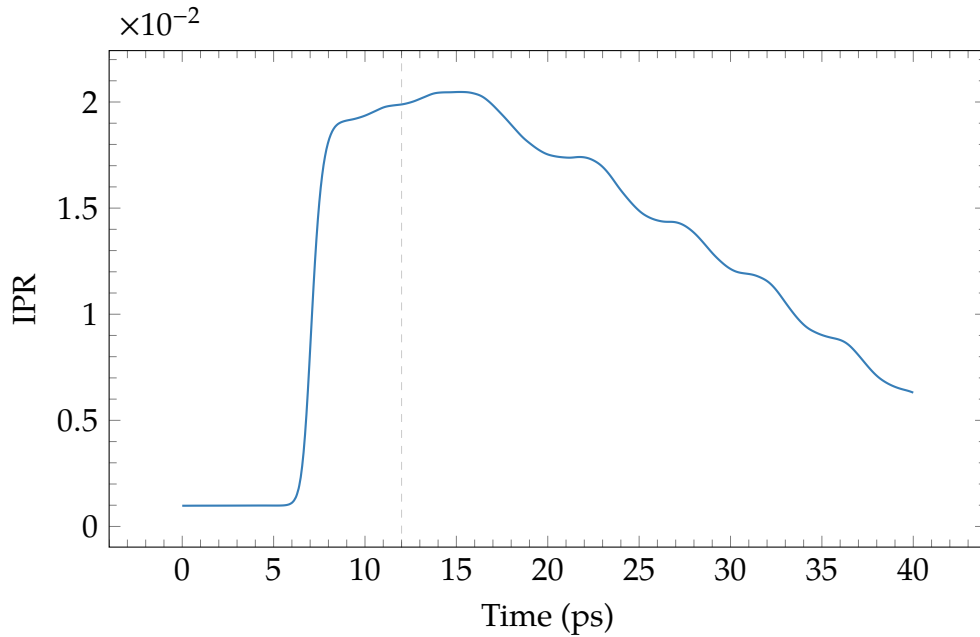


Figure 3.7: Inverse participation ratio (IPR) for the system shown in fig. 3.6. The dashed line indicates the sample time for fig. 3.6.

illuminates the system. Without any inter-dot interactions, such a pulse would perfectly transition every quantum dot from $|0\rangle$ to $|1\rangle$, leaving behind no polarization after the pulse has passed. As the system in fig. 3.6 has experienced most of the pulse, the majority of the quantum dots behave this way. A number of particles remain polarized well after the pulse has passed through the system, however, due to their apparent proximity.

3.4.2 Polarization enhancement

Borrowing from standard measures of localization (in which one calculates integrals of \mathbf{E} over the simulation volume), we have adapted the inverse participation ratio (IPR) of the dot polarization as

$$\text{IPR}(t) = \frac{\sum_{\ell} |\tilde{\mathbf{p}}_{\ell}(t)|^4}{\left(\sum_{\ell} |\tilde{\mathbf{p}}_{\ell}(t)|^2\right)^2} \quad (3.15)$$

to provide a quantitative description of these phenomena [66]. Figure 3.7 shows this quantity for the system in fig. 3.6. The maximum IPR occurs some time after the pulse has passed through the system, indicating strongly-coupled quantum dots retain their polarization longer than their neighbors. Moreover, this dynamical localization effect features oscillations which suggests many-dot effects contribute to the dynamics within a narrow spectral region.

Figure 3.8 depicts the evolution of $|\rho_{01}(\mathbf{r})|$ as an indicator of $\tilde{\mathbf{P}}$ for a cylinder containing 10 000 quantum dots. The cylinder has a radius of $0.2 \mu\text{m}$ and a length of $4 \mu\text{m}$, and the incident \mathbf{k}_L lies along the cylindrical axis (again perpendicular to \mathbf{d} so as to maximize the long-distance interaction between quantum dots). This simulation captures the suppression effects of figs. 3.5 and 3.6 as a small number of quantum dots remain in an unexcited state while the cylinder polarizes around them. Additionally, due to the length of the cylinder, larger regions of enhanced polarization begin to appear as the system polarizes—an effect we did not observe in sub-wavelength structures. We liken these nodes to standing waves in a cavity that arise from the far-field interaction term of eq. (3.5). As the pulse varies little

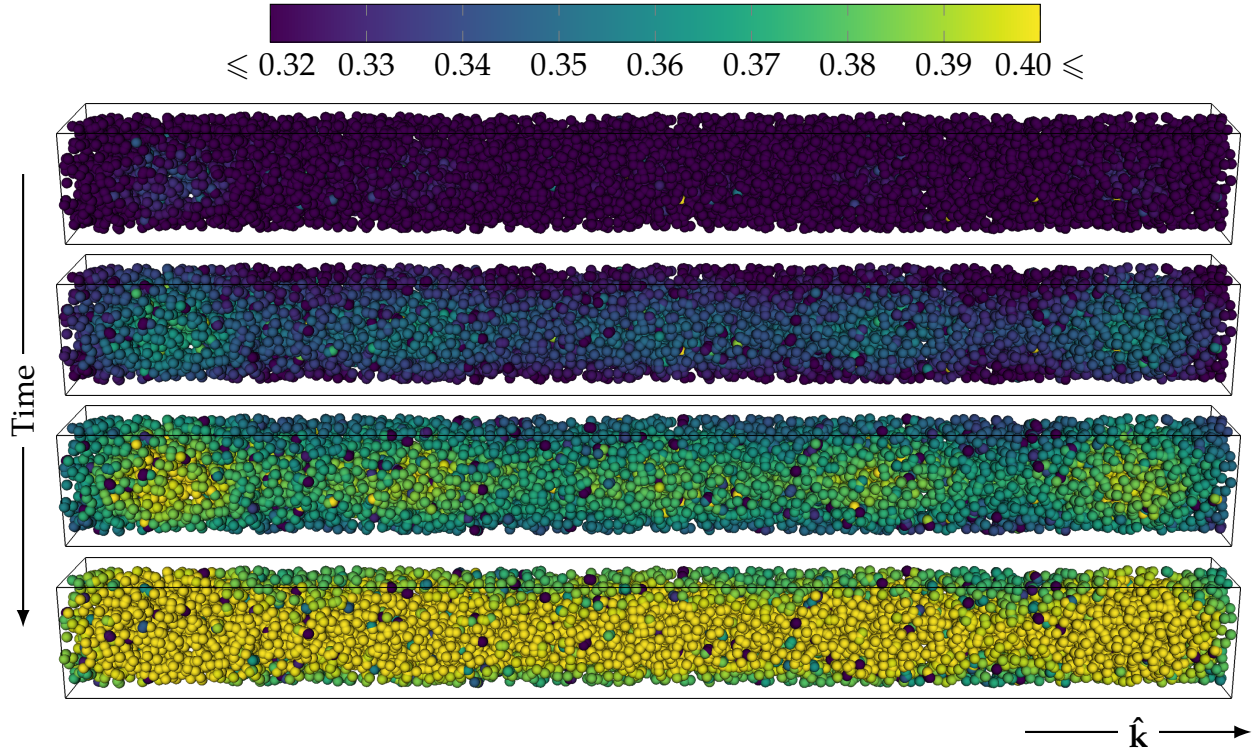


Figure 3.8: Coloration of $|\tilde{\rho}_{01}|$ as an indicator of $|\tilde{\mathbf{P}}|$ at $t_1 = -0.05$ ps, $t_2 = 0$ ps, $t_3 = 0.05$ ps, and $t_4 = 0.10$ ps relative to the peak of a 1 ps-wide pulse. 10 000 quantum dots randomly distributed throughout a $0.2 \mu\text{m}$ (radius) $\times 4 \mu\text{m}$ cylinder oriented along \mathbf{k}_L demonstrate near-field the effects of fig. 3.5 as distinct, outlying bright/dark quantum dots. Additionally, the size of the system allows for wavelength-scale phenomena that appear here as five standing regions of enhanced polarization. (Note that we model quantum dots as point objects; the size of the spheres here has no physical interpretation.)

over the length of the cylinder, identical simulations run without interactions (i.e. $\mathcal{Z} = 0$ everywhere) produce homogeneous polarization distributions. Reducing the simulation to a planar geometry (fig. 3.9) preserves both the short-range (dark, adjacent quantum dots) and long-range (regions of enhanced/diminished polarization) phenomena observed in fig. 3.8. We note these geometries produce a much weaker effect than their fully three dimensional counterparts, though larger simulations with greater far-field contributions or quantum dots engineered to have a larger dipole moment may produce more measurable effects.

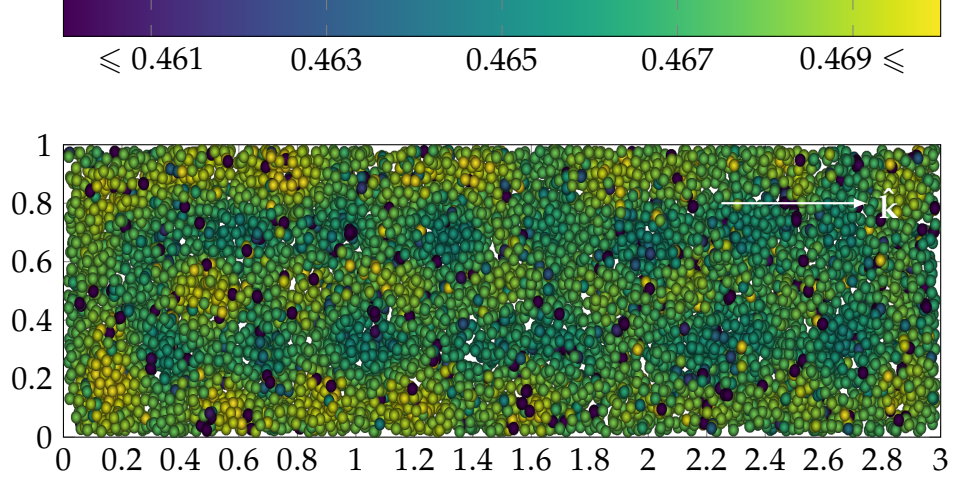


Figure 3.9: Coloration of $|\tilde{\rho}_{01}|$ for 10 000 quantum dots arranged in a finite planar geometry (in units of λ). The slab displays a prominent polarization pattern 1.25 ps after the peak of a 1 ps pulse.

3.4.3 Inhomogeneous broadening

Thus far we have investigated only homogeneous systems (i.e. an identical ω_0 for every quantum dot in the system). To probe the effects of interaction-independent inhomogeneities (possibly occurring due to some experimental variation in quantum dot sizes), fig. 3.10 presents four simulations with normally-distributed transition frequencies characterized by a width parameter. In simulations with mild detuning, we observe a distribution pattern characteristic of the enhancement phenomenon seen in fig. 3.8. More variation in the detuning distribution, however, quickly serves to destroy these phenomena, leaving only “pulse-driven” effects. At present, inhomogeneous broadening in quantum dots typically exceeds the values used in fig. 3.10. Impurity-bound excitons have greatly diminished inhomogeneous effects and thus could offer an avenue to observe these phenomena [74].

3.5 Conclusions & future work

Here we developed a robust, fine-grained algorithm to solve for the dynamics of an ensemble of quantum dots that couple in response to external light fields. By making use of

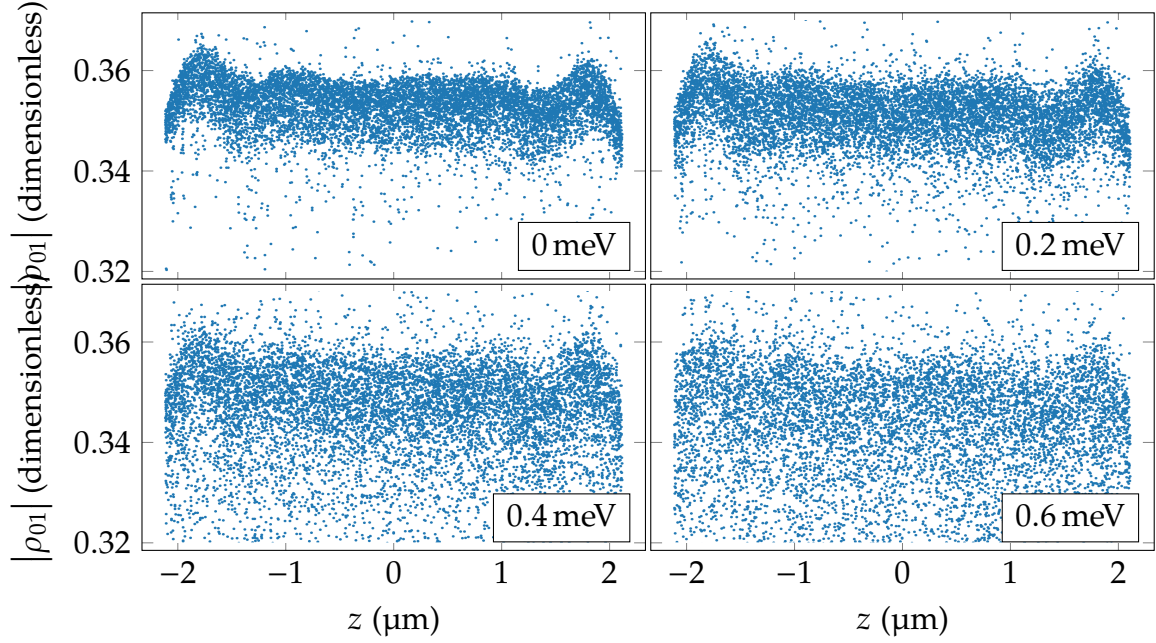


Figure 3.10: z -distribution of polarization $|\tilde{\rho}_{01}|$ for the geometry in fig. 3.8. In each simulation, 10 000 quantum dots had random Gaussian noise (with width parameters of 0.0 meV, 0.2 meV, 0.4 meV and 0.6 meV) added to a resonant $\hbar\omega_0 = 1500$ meV. The induced long-range patterns in the polarization remain for mild detunings $\lesssim 0.5$ meV but have completely washed out at 0.6 meV. Additionally, each simulation displayed the characteristic near-field coupling effects of fig. 3.5 (not visible here).

an integral equation kernel to propagate radiated fields, our model facilitates simulations of thousands of quantum dots in three dimensions with accurate bookkeeping of both near and far radiation fields. Our simulations predict a suppression effect between adjacent quantum dots that screens out the incident laser pulse and we interpret this effect as a dynamical detuning that shifts the effective ω_0 of the affected quantum dots. Moreover, we observe additional oscillatory behavior and localization effects in larger clusters of particles. These effects could prove useful in optically identifying quantum dot “molecules” in an extended sample by detecting residual localized polarization following integral π pulse(s)—we expect that an experimental π -pulse calibrated to a single quantum dot with a scanning-type polarization measurement [7] would reveal signatures of these effects in dense samples. Finally, in larger systems of densely-packed quantum dots, we see significant localization/enhanced polarization over length scales comparable to that of the

incident wavelength. These effects persist in simulations with other extended geometries and in simulations with inhomogeneously-broadened transition frequencies, though the effects quickly disappear with only a few meV detuning.

Semi-classical approaches can describe some superradiant effects within a continuum formulation [38, 15, 16]. First predicted in 2005 [72] and observed in 2007 [65], superradiant effects in quantum dot ensembles have since spurred theoretical analyses into cooperative radiation mechanisms [73, 20]. While our semiclassical approach accounts for collective effects due to the secondary field emission from quantum dots, we do so in the Hamiltonian term on the right hand side of eq. (3.1) and not in the $\hat{\mathcal{D}}[\hat{\rho}]$ dissipator. In future work, we plan to extend our microscopic approach to include collective dissipation effects so as to better model superradiant phenomena. We expect that our approach—when extended to systems containing a larger number of quantum dots—will aid in investigating the role of many-dot interactions in systems such as nanolasers [46] that exploit these phenomena. Unfortunately, the naïve $\mathcal{O}(N_s^2)$ interaction calculation presented here hampers attempts to extend these calculations to systems more than $\sim 10^4$ spatial unknowns. Our ongoing research includes the development of accelerated computational techniques that exploit the structure of \mathcal{Z} to reduce the big- \mathcal{O} complexity of eq. (3.9). Additionally, the technique presented here readily extends to model atomic, molecular, and semiconductor systems with richer structure (e.g. systems with energy degeneracies or biexcitonic transitions).

CHAPTER 4

AN FFT-ACCELERATED SOLUTION METHODOLOGY FOR RADIATIVE MAXWELL-BLOCH SYSTEMS

“Curiouser and curiouser!”

—The Cheshire Cat, *Alice in Wonderland*

4.1 Abstract

The Maxwell-Bloch algorithm of chapter 3 scales poorly for large numbers of quantum dots due to an implicit $O(n^2)$ spatial complexity in the propagation calculation (eqs. (3.9) and (3.10)). As many physical systems have the same mathematical structure, numerous techniques exist to reduce the poor scaling of these convolutions with fully controllable error. This chapter will explain this bottleneck, several acceleration schemes that one might use to alleviate it, and, why we feel one particular variety of accelerator works best. Additionally, I will detail the mathematics of such an acceleration technique, offer a reference implementation online, and give physical results found through simulating extended systems.

4.2 Introduction

The naïve $O(n^2)$ complexity of matrix-vector products in integral equation systems stands as the singular bottleneck to large-scale simulations of related phenomena. Since the 1990s, so-called “fast” solvers have played a critical role in alleviating this bottleneck; by exploiting properties of the underlying physical system (such as smoothness and translational invariance) these methods achieve space and time complexities of $O(n \log n)$ or even $O(n)$ with fully-controllable error¹.

¹In particular this means one can choose parameters such that the error in the calculation falls below the floating point error of a given machine, thus fast solution techniques produce identical results to their naïve counterparts with *no* discernible approximation error.

Kernel-type solvers [37, 27] exploit the physical similarity of sources at large distances to develop a series representation of the Green’s function in terms of source and observation regions independently. Specifically, these techniques lump adjacent sources together so as to transmit their effects in aggregate across large distances (a process not dissimilar to how a telephone network or the Internet works). These methods scale very well for surface discretizations as they intelligently partition the simulation space into a hierarchy of boxes and only compute interactions between regions containing sources. Unfortunately, as these methods rely on the underlying mathematical structure of the kernel to produce a suitable series representation, they have limited utility in systems with nonstandard (specifically rotating-frame) kernels.

In contrast, *source-type* solvers [12, 84, 49] apply effective transformations to the source distribution (leaving the actual interaction kernel unchanged) with the intention of producing a nearly-equivalent system with exploitable low-rank properties. The Adaptive Integral Method (AIM), which we extend here, represents a kernel matrix as a sum of nearfield and farfield contributions, each constructed from a different set of basis functions. For all basis functions within a prescribed distance of each other, we compute their interactions directly, thus the nearfield matrix becomes increasingly sparse in the limit of a large number of sources. The farfield contribution arises as the interaction between a reduced number of auxiliary basis functions (commonly taken as δ -functions) on a regular Cartesian grid. Each source function maps to a finite number of overlapping auxiliary functions—thus the mapping matrices have a sparse signature and compress the distant portions of the interaction matrix—and the translationally-invariant structure imposed by the Cartesian grid allows for an efficient matrix diagonalization by way of a (multidimensional) fast Fourier transform (FFT). Because AIM does not rely on the specific mathematical form of the interaction kernel (a so-called “algebraic acceleration”), it works equally well for rotating and fixed-frame problems.

4.3 Problem statement

We wish to calculate the field radiated from a distribution of time-dependent sources under the action of an arbitrary (linear) differential operator, $\mathfrak{F}\{\cdot\}$. These fields exist throughout space and time alongside/in response to an incident field, \mathbf{E}_{inc} . Formally, we may write the total field everywhere as

$$\begin{aligned} \mathbf{E}(\mathbf{r}, t) &= \mathbf{E}_{\text{inc}}(\mathbf{r}, t) + \mathfrak{F} \left\{ \iint g(\mathbf{r} - \mathbf{r}', t - t') \mathbf{P}(\mathbf{r}', t') d^1 t' d^3 \mathbf{r}' \right\} \\ &\equiv \mathbf{E}_{\text{inc}}(\mathbf{r}, t) + \mathfrak{F} \{ g(\mathbf{r}, t) * \mathbf{P}(\mathbf{r}, t) \} \end{aligned} \quad (4.1)$$

where $g(\mathbf{r}, t)$ denotes a propagation potential (most commonly the retarded potential, $g(\mathbf{r}, t) = \delta(t - |\mathbf{r}|/c)/|\mathbf{r}|$). To numerically evaluate eq. (4.1), we discretize $\mathbf{P}(\mathbf{r}, t)$ with separable space/time basis functions such that

$$\mathbf{P}(\mathbf{r}, t) \approx \sum_{\ell=0}^{N_s-1} \sum_{m=0}^{N_t-1} \mathcal{A}_\ell^{(m)} \mathbf{s}_\ell(\mathbf{r}) T(t - m \Delta t) \quad (4.2)$$

where Δt denotes a fixed time interval chosen to accurately sample the dynamics of the physical quantities involved. Furthermore, we require both $\mathbf{s}_\ell(\mathbf{r})$ and $T(t)$ to have finite support and that $T(t)$ obey (discrete) causality (i.e. $T(t) = 0$ if $t \notin [-\Delta t, T_{\text{max}}]$). Here, we consider δ -functions and shifted Lagrange polynomials for the $\mathbf{s}_\ell(\mathbf{r})$ and $T(t)$, respectively, though this analysis readily extends to accommodate any similar set of functions.

Substituting eq. (4.2) into eq. (4.1) and projecting the resulting field onto the same set of $\mathbf{s}_\ell(\mathbf{r})$ produces an $(N_s \times N_s)$ -block matrix equation of the form

$$\mathcal{E}^{(m)} = \mathcal{E}_{\text{inc}}^{(m)} + \sum_{m'=0}^m \mathcal{F}^{(m-m')} \cdot \mathcal{A}^{(m')} \quad (4.3)$$

where

$$\mathcal{E}_\ell^{(m)} = \langle \mathbf{s}_\ell(\mathbf{r}), \mathbf{E}(\mathbf{r}, m \Delta t) \rangle \quad (4.4a)$$

$$\mathcal{E}_{\text{inc}, \ell}^{(m)} = \langle \mathbf{s}_\ell(\mathbf{r}), \mathbf{E}_{\text{inc}}(\mathbf{r}, m \Delta t) \rangle \quad (4.4b)$$

$$\mathcal{F}_{\ell \ell'}^{(k)} = \langle \mathbf{s}_\ell(\mathbf{r}), \mathfrak{F} \{ g(\mathbf{r}, t) * \mathbf{s}_{\ell'}(\mathbf{r}) T(k \Delta t) \} \rangle. \quad (4.4c)$$

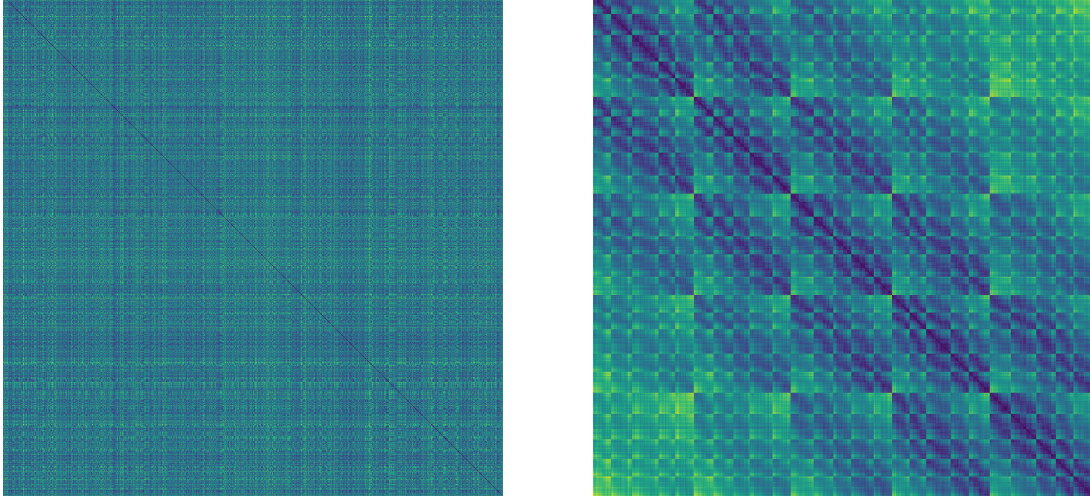


Figure 4.1: the interaction matrix for $g(\mathbf{r}, t) = |\mathbf{r}|^{-1}$ between points randomly distributed throughout a unit cube appears to have very little structure (left). while we cannot fully order the points in three dimensions, we *can* permute the matrix so as to give points within the same neighborhood adjacent indices. points ordered thusly produce a diagonally-dominant interaction matrix with a hierarchical Toeplitz substructure (right). such structures indicate portions of the matrix have very accurate low-rank approximations that offer the possibility of significant compression.

From this, it immediately becomes apparent that eq. (4.4c) bottlenecks the field calculation due to the $O(N_s^2)$ complexity of the inner product.

4.4 Computational approach

To effect a sub-quadratic calculation of eq. (4.3), we approximate $\mathcal{F}^{(k)}$ as a sum of near- and far-field contributions. The near-field matrix elements follow directly from eq. (4.4c)—sources within a prescribed distance threshold interact “directly” so as to avoid incurring unreasonable approximation error between adjacent basis functions. Sources beyond this threshold, however, interact via auxiliary spatial basis functions taken to reside at the vertices of a regular Cartesian grid. These auxiliary sources recover $\mathfrak{F}\{g(\mathbf{r}, t) * \mathbf{P}(\mathbf{r}, t)\}$ at large distances and have two computational advantages: (i) they compress the interaction matrix by representing sources within the same spatial region in terms of the same auxiliary set (fig. 4.2) and (ii) they impose a Toeplitz structure on the resulting interaction matrix that lends itself to efficient diagonalization through application of an FFT. One iteration of

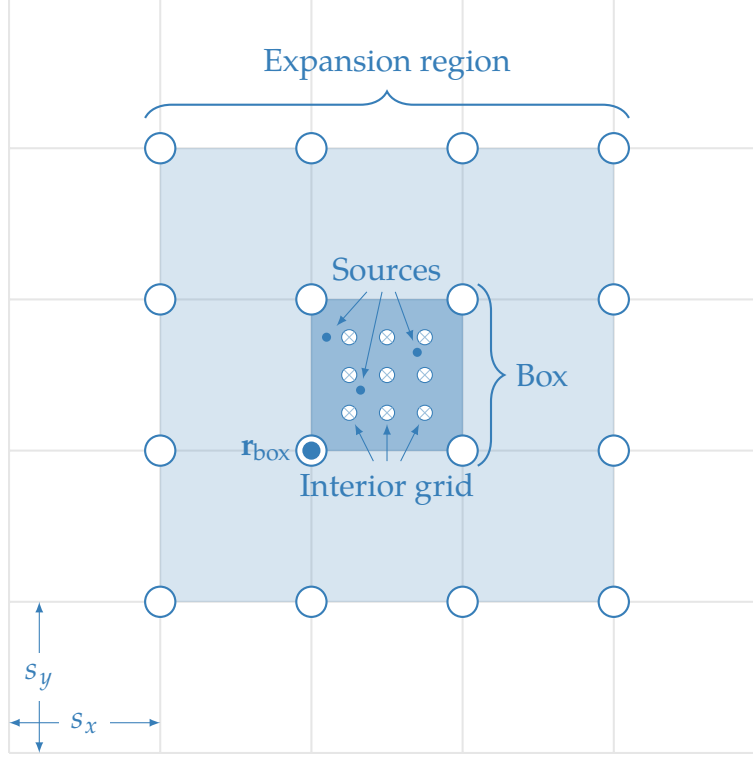


Figure 4.2: Illustration of the grid structure and related terminology. All of the sources within a box (shown as the central shaded square) map to the same set of expansion points (shown as open circles) indexed relative to \mathbf{r}_{box} .

our algorithm, then, proceeds as follows:

1. At timestep m project each of the $s_\ell(\mathbf{r})\mathcal{A}_\ell^{(m)}$ onto the auxiliary sources. Aside from discretization/sampling criteria, the operators in eq. (4.1) do not affect these projections, thus the distribution of auxiliary sources, $\mathbf{P}_{\text{aux}}(\mathbf{r}, t)$, mimics the distribution of $\mathbf{P}(\mathbf{r}, t)$ at large distances.
2. Effect the convolution in eq. (4.1) between auxiliary sources. Having imposed a regular structure on $\mathbf{P}_{\text{aux}}(\mathbf{r}, t)$, we may efficiently diagonalize the matrix representing this (discrete) convolution with (up to four-dimensional) blocked FFTs. Note that the algorithm thus far has essentially evaluated the potential, $g(\mathbf{r}, t) * \mathbf{P}(\mathbf{r}, t)$, at $t = m \Delta t$ at every point \mathbf{u} in the grid.
3. Recover the total field under the action of \mathfrak{F} by projecting the potential on each \mathbf{u}

back onto the $\mathbf{s}_\ell(\mathbf{r})$. These projections make use of specialized projection matrices that depend on the particular derivatives contained inside \mathfrak{F} .

4. Subtract the fields determined by steps 1-3 for pairs of spatial basis functions within a prescribed distance threshold and replace it with eq. (4.4c). The auxiliary grid approximations only remain accurate at large distances, thus this step corrects large approximation errors that occur between adjacent $\mathbf{s}_\ell(\mathbf{r})$.

Mathematically,

$$\begin{aligned} \mathcal{F}^{(m-m')} &\approx \mathcal{F}_{\text{direct}}^{(m-m')} + \Lambda_{\mathfrak{F}} \begin{pmatrix} \partial_t^0 \mathcal{G}^{(m-m')} \\ \partial_t^1 \mathcal{G}^{(m-m')} \\ \partial_t^2 \mathcal{G}^{(m-m')} \\ \vdots \end{pmatrix} \Lambda^\dagger \\ &\equiv \mathcal{F}_{\text{direct}}^{(m-m')} + \mathcal{F}_{\text{FFT}}^{(m-m')} \end{aligned} \quad (4.5)$$

where

$$\mathcal{F}_{\text{direct},\ell\ell'}^{(m-m')} = \begin{cases} \mathcal{F}_{\ell\ell'}^{(m-m')} - \mathcal{F}_{\text{FFT},\ell\ell}^{(m-m',\tau)} & R_{\ell\ell'} \leq \gamma \\ 0 & \text{otherwise,} \end{cases} \quad (4.6a)$$

$$\mathcal{G}_{ab}^{(m-m')} = \langle \mathbf{u}_a(\mathbf{r}) \delta(t - (m - m') \Delta t), g(\mathbf{r}, t) * \mathbf{u}_b(\mathbf{r}) T(t) \rangle \quad (4.6b)$$

The Λ matrices in eq. (4.5) denote the (sparse) projections to and from the grid (detailed in section 4.4.1), and $\mathbf{u}_a(\mathbf{r})$ indicates an auxiliary basis function on the spatial grid indexed by a . Finally, τ_{max} and γ serve as adjustable input parameters to control the accuracy of the simulation and $R_{\ell\ell'}$ gives the minimum distance (in integral units of the grid spacing) between the expansion regions enclosing $\mathbf{s}_\ell(\mathbf{r})$ and $\mathbf{s}_{\ell'}(\mathbf{r})$ (fig. 4.3) via

$$R_{\ell\ell'}^{\text{grid}} = \min\{\|\mathbf{u} - \mathbf{u}'\|_\infty \mid \mathbf{u} \in C_\ell, \mathbf{u}' \in C_{\ell'}\}. \quad (4.7)$$

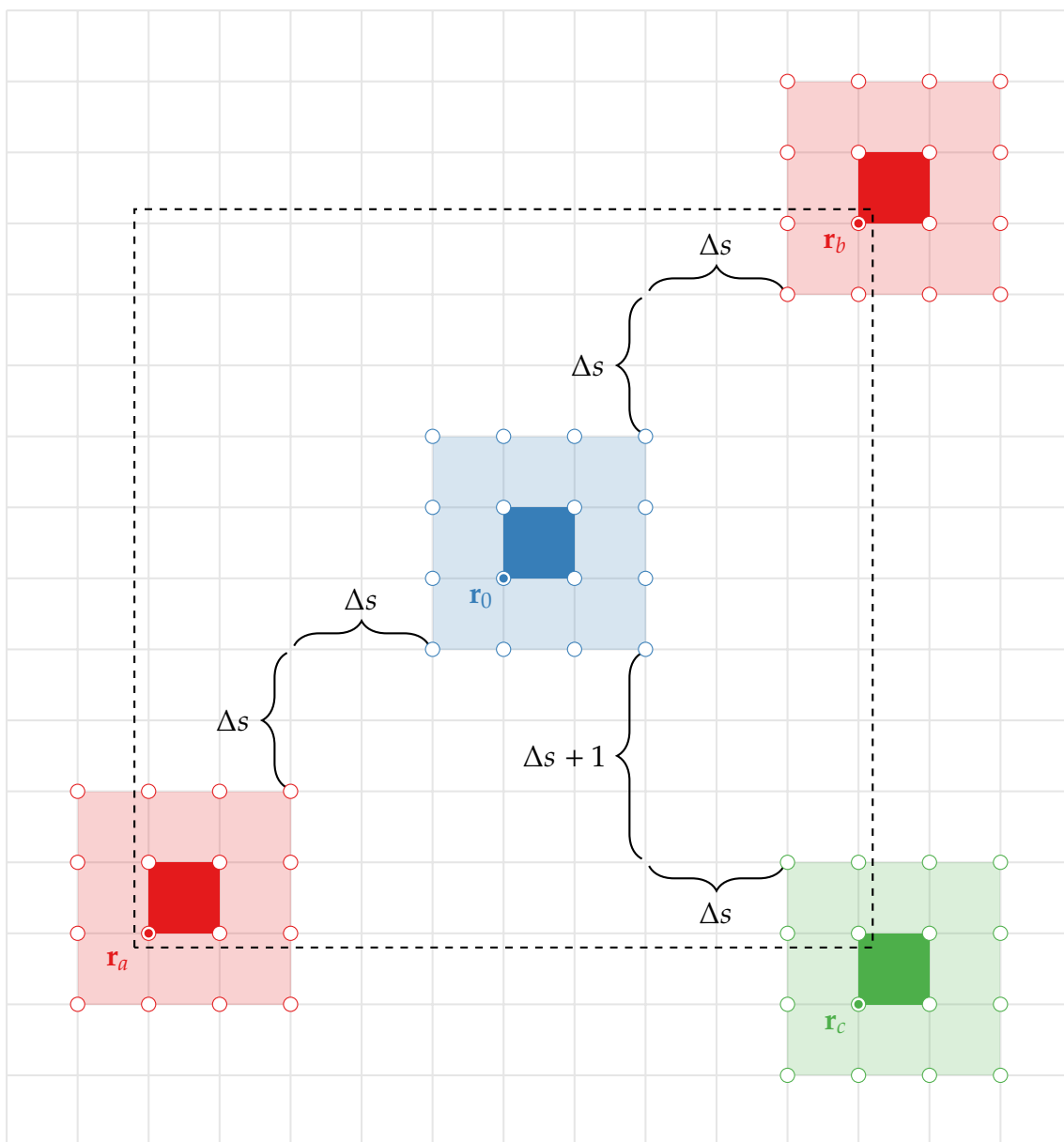


Figure 4.3: Illustration of the nearfield criterion for a third order expansion ($\gamma = 2$). The dashed line indicates the complete nearfield of the box associated with \mathbf{r}_0 —i.e. all boxes that have an expansion point within Δs of the expansion around \mathbf{r}_0 . Consequently, all of the $\mathbf{s}_\ell(\mathbf{r})$ within the central dark blue square have a pairwise interaction with the $\mathbf{s}_{\ell'}(\mathbf{r})$ inside the dashed box.

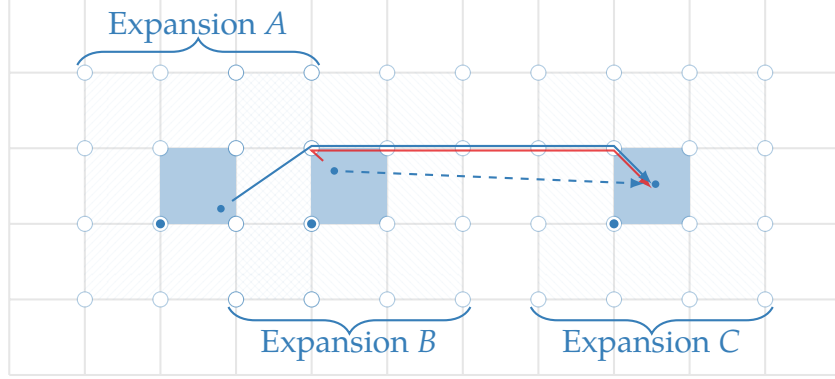


Figure 4.4: Illustration of nearfield corrections between close boxes. Expansions A and B overlap, but only box B lies in the nearfield of box C . The grid-based propagation strategy only remains accurate for distant source/observer pairs. To avoid incurring undue error, we remove the interaction “through the grid” between the BC pair (red line) and replace it with a more accurate “direct” interaction (dashed blue line). The AC pair requires no such treatment as they have well-separated expansion regions.

4.4.1 Expansion matrices

We represent the primary $\mathbf{s}_\ell(\mathbf{r})$ basis functions as a weighted sum of δ -functions on the surrounding gridpoints, thus $\mathbf{u}_a(\mathbf{r}) \propto \delta(\mathbf{r} - \mathbf{r}_a)$ and

$$\psi_\ell(\mathbf{r}) \approx \sum_{\mathbf{u} \in C_\ell} \Lambda_{\ell\mathbf{u}}^\dagger \delta(\mathbf{r} - \mathbf{u}). \quad (4.8)$$

Here, $\psi_\ell(\mathbf{r}) \in \{\mathbf{s}_\ell(\mathbf{r}) \cdot \hat{\mathbf{x}}, \mathbf{s}_\ell(\mathbf{r}) \cdot \hat{\mathbf{y}}, \mathbf{s}_\ell(\mathbf{r}) \cdot \hat{\mathbf{z}}\}$ and C_ℓ denotes the collection of grid points within the expansion region of $\mathbf{s}_\ell(\mathbf{r})$ (fig. 4.2). For an expansion of order² m , this sum contains $(m + 1)^3$ terms corresponding to the $(m + 1)^3$ grid points nearest to $\mathbf{s}_\ell(\mathbf{r})$ (fig. 4.5). Consequently, the $\Lambda_{\ell\mathbf{u}}^\dagger$ matrices contain few nonzero elements and we have elected to use a moment-matching scheme to capture the $(m + 1)^3$ multipole moments of $\mathbf{s}_\ell(\mathbf{r})$ according to

$$\int (x - x_0)^{m_x} (y - y_0)^{m_y} (z - z_0)^{m_z} \left[\psi_\ell(\mathbf{r}) - \sum_{\mathbf{u} \in C_\ell} \Lambda_{\ell\mathbf{u}}^\dagger \delta(\mathbf{r} - \mathbf{u}) \right] d^3\mathbf{r} = 0. \quad (4.9)$$

In this expression, $0 \leq m_x, m_y, m_z \leq m$ and $\mathbf{r}_0 \equiv x_0 \hat{\mathbf{x}} + y_0 \hat{\mathbf{y}} + z_0 \hat{\mathbf{z}}$ denotes the origin about which we compute the multipoles. To determine the $\Lambda_{\ell\mathbf{u}}^\dagger$, we then solve the least-squares

²In principle, one could expand to different orders in different Cartesian directions, though this involves considerably more bookkeeping for relatively little benefit. Thus, for convenience, we take “the expansion order” to mean the expansion order in every direction.

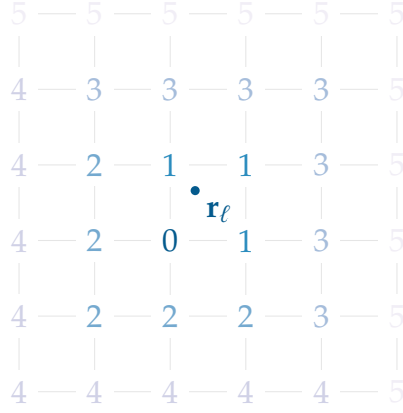


Figure 4.5: Spatial expansion pattern for $\mathbf{s}_\ell(\mathbf{r}) = \hat{\mathbf{d}}_\ell \delta(\mathbf{r} - \mathbf{r}_\ell)$ through order five. The numbers on the grid indicate the points added in the equivalent order expansion such that an expansion of order m requires $(m + 1)^3$ grid points. Moreover, increasing the expansion order incorporates new points in such a way as to keep $\mathbf{s}_\ell(\mathbf{r})$ as close to the center of the expansion region as possible.

system

$$\sum_{\mathbf{u} \in C_\ell} W_{\mathbf{mu}} \Lambda_{\ell \mathbf{u}}^\dagger = Q_{\ell \mathbf{m}} \quad (4.10)$$

where

$$W_{\mathbf{mu}} = (u_x - x_0)^{m_x} (u_y - y_0)^{m_y} (u_z - z_0)^{m_z} \quad (4.11a)$$

$$Q_{\ell \mathbf{m}} = \int \psi_\ell(\mathbf{r}) (x - x_0)^{m_x} (y - y_0)^{m_y} (z - z_0)^{m_z} d^3 \mathbf{r}, \quad (4.11b)$$

$\mathbf{u} \in C_\ell$, and \mathbf{m} denotes the multi-index $\mathbf{m} = \{m_x, m_y, m_z\}$. With an infinite precision calculation, the choice of $\mathbf{r}_0 = x_0 \hat{\mathbf{x}} + y_0 \hat{\mathbf{y}} + z_0 \hat{\mathbf{z}}$ merely defines an origin for the polynomial expansion system. To minimize numerical issues, we choose \mathbf{r}_0 at the center of $\mathbf{s}_\ell(\mathbf{r})$.

As Λ^\dagger arises purely as a function of space with no time component, differentiating eq. (4.9) with respect to x , y , or z can also recover spatial derivatives occurring in \mathfrak{F} . We interpret this as differentiating the underlying polynomial that interpolates the potential between gridpoints at the location of $\mathbf{s}_\ell(\mathbf{r})$, thus the differentiation procedure removes the high-order moments in eq. (4.11b).

4.4.2 Complexity

We have largely designed this acceleration algorithm to accommodate time-domain propagators within a rotating-wave/envelope-tracking framework. Such systems notably have decoupled length and time scales; downshifting a narrow-band signal to baseband (in time) affords very efficient temporal discretizations due to an assumed carrier signal. No such trick works for the spatial properties, however, due to the space/time coupling in $g(\mathbf{r}, t)$ and need to preserve interference phenomena throughout space³. As such, $g(\mathbf{r}, t)$ can impose a high spatial frequency on fields radiating from artificially low-frequency sources. Consequently, the both the primary and auxiliary spatial basis functions require a discretization on the order of this spatial frequency to accurately sample fields. The calculation of eq. (4.5), then, remains the dominant factor in the complexity of our algorithm, though it performs significantly better than a pairwise interaction between all of the $\mathbf{s}_\ell(\mathbf{r})$. Projecting sources to/from the auxiliary grid (i.e. right-multiplying by $\Lambda_{\mathfrak{F}}$ or Λ^\dagger) necessarily require $\mathcal{O}(N_s)$ operations per timestep as each $\mathbf{s}_\ell(\mathbf{r})$ maps to a fixed number $\mathbf{u}_a(\mathbf{r})$ auxiliary functions, independent of N_s . Similarly, for uniformly-dense volume-filling geometries, a volume proportional to γ^3 contains a fixed number of $\mathbf{s}_\ell(\mathbf{r})$ independent of N_s , ergo the calculation of $\mathcal{F}_{\text{direct}}^{(m-m')} \mathcal{A}^{(m')}$ also requires $\mathcal{O}(N_s)$ operations. Thus, the potential evaluation between auxiliary functions—multiplying by $\mathcal{G}^{(m-m')}$ and its derivatives—dominates the overall complexity of the calculation. By storing a diagonal, \mathbf{k} -space representation of these matrices (requiring storage proportional only to the number of grid points, N_{grid} , not its square), each timestep in the algorithm requires an $\mathcal{O}(N_{\text{grid}} \log N_{\text{grid}})$ forward FFT to equivalently transform the auxiliary source distribution, an $\mathcal{O}(N_{\text{grid}})$ elementwise product to effect the “convolution”, and a backward $\mathcal{O}(N_{\text{grid}} \log N_{\text{grid}})$ to restore the potential in \mathbf{r} - (not \mathbf{k} -) space. Similar Toeplitz diagonalization strategies also work in time (see [84, section D]) though this provides almost no benefit in rotating-frame systems due to the relatively

³Because of this, rotating-wave systems share a large number of similarities with their fully frequency-domain counterparts.

small number of timesteps required for radiation to traverse the system.

Additionally, we note that transferring the spatial derivatives in \mathfrak{F} onto the “receiving” projection matrices, $\Lambda_{\mathfrak{F}}$, results in a modest acceleration for tensorial propagators such as that of the electric, magnetic, or combined field integral equations,

$$\mathfrak{F} = \partial_t^2 - c^2 \nabla \nabla \cdot . \quad (4.12)$$

Instead of projecting both $\mathbf{s}_\ell(\mathbf{r})$ and $\nabla \cdot \mathbf{s}_\ell(\mathbf{r})$ onto the auxiliary grid and propagating them with the relatively expensive \mathcal{G} multiplication, we reconstruct all spatially-varying quantities from the potential sampled on the auxiliary grid. (A similar method reconstructs time derivatives from the history of potential samples on the auxiliary grid, though this requires a discrete convolution with several weighted $\Lambda_{\mathfrak{F}}$ matrices.) Moreover, this decomposition maintains the strong form of the integral relation in eq. (4.1) and makes no assumptions of differentiability in the underlying $\mathbf{s}_\ell(\mathbf{r})$ discretization.

4.5 Results

4.5.1 Convergence

Consider two point particles located at x_{src} and x_{obs} . A time-independent Green’s function, $g(x_{\text{obs}} - x_{\text{src}})$, describes the interaction between the two particles and we wish to construct a polynomial approximation of $g(x - x_{\text{src}})$ for x in the vicinity of x_{obs} as in fig. 4.6.

To construct an interpolation polynomial over the expansion region of order M , we define a polynomial coordinate x_p in units of h such that $x_p^{\text{min}} \leq x_p \leq x_p^{\text{min}} + M$ where $x_p^{\text{min}} \equiv -\lfloor M/2 \rfloor$. Consequently, the expansion points about x_{obs} correspond to $x_p \in \{-\lfloor M/2 \rfloor, -\lfloor M/2 \rfloor + 1, -\lfloor M/2 \rfloor + 2, \dots\}$ with the 0th order expansion point, x_0 , equivalent to $x_p = 0$. Such a coordinate system defines the Vandermonde linear equation

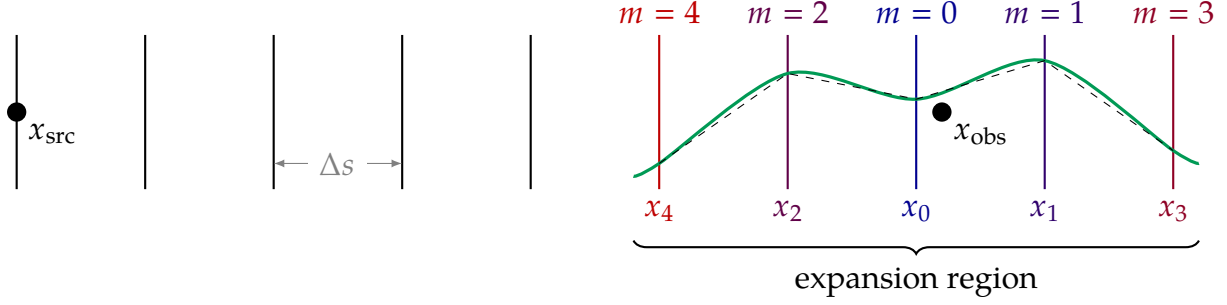


Figure 4.6: Polynomial interpolation of $g(x - x_{\text{src}})$ near x_{obs} . Here, the green curve represents the actual $g(x - x_{\text{src}})$ and the dashed black line its approximation. Evaluating the m^{th} -order approximation requires samples of the signal at $m + 1$ grid points surrounding x_{obs} .

$\sum_j V_{ij} w_j = g_i$ for the weights of an interpolating polynomial⁴ [62] where

$$V_{ij} = (x_p^{\min} + i)^j \quad (4.13a)$$

$$g_i = g\left((x_0 - x_{\text{src}}) + (x_p^{\min} + i) \Delta s\right) \quad (4.13b)$$

and $0 \leq i, j \leq M$. Approximating $g(x - x_{\text{src}})$ at x_{obs} then becomes a matter of evaluating this polynomial at $x_p = (x_{\text{obs}} - x_0)/h$, i.e.

$$g(x_{\text{obs}} - x_{\text{src}}) \approx \sum_{i=0}^M w_i \left(\frac{x_{\text{obs}} - x_0}{\Delta s}\right)^i. \quad (4.14)$$

Accordingly, the polynomial approximation to $g(x_{\text{obs}} - x_{\text{src}})$ contains terms of order $\mathcal{O}(h^{-M})$ and we can expect the approximation error to scale as $\mathcal{O}(\Delta s^{-(M+1)})$ as demonstrated in fig. 4.7. This also motivates using the approximation to calculate interactions involving differential operators; applying an n^{th} -order derivative reduces the polynomial order by n , thus the error scales like $\mathcal{O}(\Delta s^{-(M+1)+n})$.

⁴In principle this analysis works equally well in the original $(x_{\text{src}}, x_{\text{obs}})$ coordinate system. The polynomial coordinate has three advantages, however: it indexes the expansion points “logically” from left to right, $x_p^{\min} \in \mathbb{Z}$ and thus the Vandermonde matrix has infinite precision, and it makes the interpolation error in terms of h explicit.

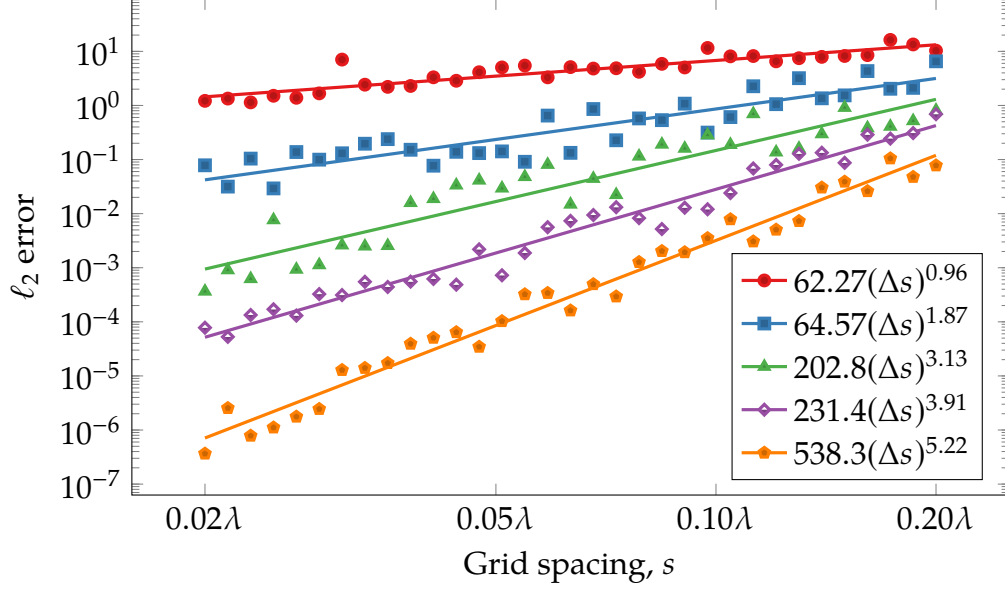


Figure 4.7: ℓ_2 error calculation of $g(\mathbf{r} - \mathbf{r}') = e^{ik|\mathbf{r}-\mathbf{r}'|}/|\mathbf{r} - \mathbf{r}'|$ for expansion orders zero through four. For each of the points above, a source and observation box separated by $\Delta\mathbf{r} = 10\lambda\hat{\mathbf{x}} + 10\lambda\hat{\mathbf{y}} + 10\lambda\hat{\mathbf{z}}$ each contain 64 randomly placed points, thus the points within each box all map to identical nodes in the auxiliary grid. The moment-matching expansion scheme dictates that the overall error for an expansion of order m scales as $\mathcal{O}(\Delta s^{m+1})$.

4.5.2 Timing

Having demonstrated the convergence properties of the accelerated algorithm, we now examine its computational efficiency. As a representative simulation, we discretize using δ -functions in space and tessellate the same arrangement of basis functions throughout each box of a cubic grid. This ensures a predictable, volume-filling geometry that captures the major features of the quantum dot systems we wish to investigate. We use a first-order expansion to project to/from the grid and a fifth-order Lagrange basis in time, and the simulation runs for 1024 timesteps, and take $\gamma = 1$ (implying expansions separated by at most one box require a nearfield correction). Finally, each source has a prescribed Gaussian amplitude of width $1024 \Delta t/12$ and centered about $1024 \Delta t/2$. These parameters give a relative error of $\sim 1 \times 10^{-6}$ in the full FFT + NEARFIELD calculation when compared with an analytic calculation. The FFT-accelerated simulation outpaces the direct field calculation near $N_s = 400$.

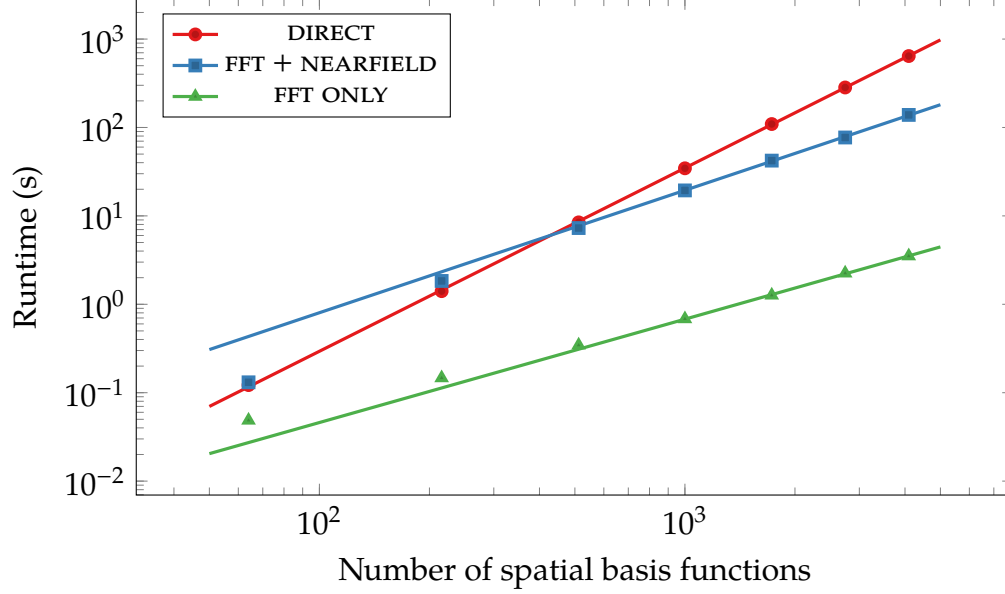


Figure 4.8: Time to evaluate retarded potential vs. number of spatial basis functions for several system sizes. Simulated on an Intel(R) Core(TM) i5-4690K CPU @ 3.50 GHz.

| Simulation | Regression | r^2 |
|-----------------|---|----------|
| DIRECT | $t(n) = 2.10086 \times 10^{-5} n^{2.073}$ | 0.999946 |
| FFT + NEARFIELD | $t(n) = 1.36362 \times 10^{-3} n^{1.385}$ | 0.999590 |
| FFT ONLY | $t(n) = 2.10896 \times 10^{-4} n^{1.169}$ | 0.999577 |

Table 4.1: Power-law regressions and their coefficients of determination (r^2) for the data in fig. 4.8. Here, t denotes the walltime of the simulation (in seconds) and n the number of spatial basis functions.

4.5.3 Maxwell-Bloch

Finally, as a pragmatic test of our algorithm, we revisit a sample radiating quantum dot system like those detailed in ???. We consider a random arrangement of 1024 quantum dots within a $0.2 \mu\text{m}$ cube. The quantum dots have a resonant transition energy of 1500 meV (thus $\omega_{\text{max}} = 1500 \text{ meV}/\hbar$) and a dipole moment of $\mathbf{d} = 10 e a_0 \hat{\mathbf{z}}$ where e and a_0 denote the electron charge and Bohr radius, respectively. We employ a rotating-wave framework so as to take $\Delta t = 50\omega_{\text{max}}$, and we use $\Delta s = c/(10\omega_{\text{max}})$ for our auxiliary grid spacing. Figure 4.9 shows the evolution of the off-diagonal matrix elements for 25 randomly sampled quantum dots with both a fully-direct and FFT-accelerated calculation.

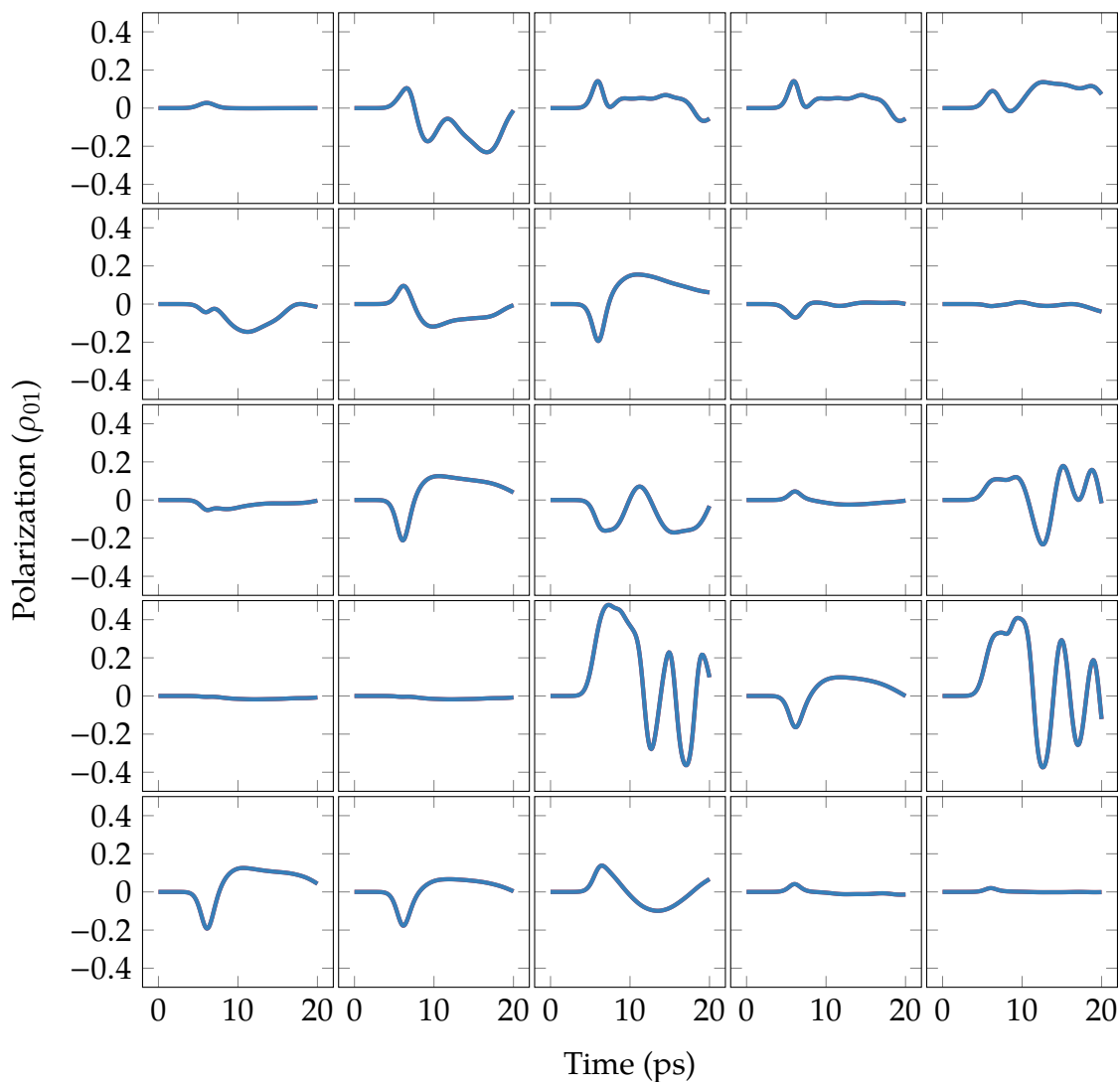


Figure 4.9: Comparison of a Maxwell-Bloch quantum dot simulation with direct (red) and FFT-accelerated (blue) propagation strategies. Here, we show the off-diagonal matrix elements of 25 random quantum dots (out of 1024) as a function of time. The quantum dots experience an incident π -pulse and their interactions induce significant secondary oscillations (see the second-to-last row). The FFT-accelerated algorithm developed here readily captures these effects, making it eminently suitable for large-scale quantum dot simulations.

CHAPTER 5

CONCLUSIONS AND FUTURE PERSPECTIVE

“Why, sometimes I’ve believed as many as six impossible things before breakfast!”

—The White Queen, *Through the Looking Glass*

This thesis serves three main purposes. First, it introduces the concept of *active media*—physical systems governed by ordinary differential equations that couple together via radiative processes—and motivates the difficulty in examining these systems at a macroscopic or continuum level. Second, it provides a discussion of numerical solution strategies based around time-domain integral equations. Finally, it introduces and details the QuEST software package. This chapter summarizes the main findings of each of these parts and offers some perspective on potential future research.

5.1 Conclusion

In chapter 2 we presented a computational analysis of acoustically-driven microsphere systems. By considering only small microspheres we cast the problem in terms of an incompressible fluid where velocity potentials describe pressure distributions. Acoustic radiation incident on the system scatters from rigid spherical objects, leading to pressure variations over the objects’ surfaces; this variation necessarily sets the objects into motion, leading to further potential/pressure perturbations within the system. By expressing the velocity potential on the surface of each microsphere in terms of spherical harmonics, we obtain a matrix equation relating the velocity of each microsphere to the potential on every other microsphere. From this, we compute the net force on every body which we then integrate numerically, noting that directly integrating the force causes numerical instabilities due to an atypical acceleration-dependent force. To remedy this, we note that this force serves only to impede the motion of each microsphere, thus we treat it as an additional mass term. We find that an incident acoustic pulse predominantly serves to translate a

collection of microspheres a fixed distance along $\hat{\mathbf{k}}$ —the pulse’s wavevector—though the scattering effects also produce system-scale expansions and contractions depending on the microspheres’ initial configuration.

Chapter 3 departs from kinematic systems to develop a semiclassical description of coupled quantum dots. Here, each of N quantum dots evolves according to the Liouville equation in response to an ambient electric field. From this, we compute the expectation value of a transition dipole moment. This acts as a source term in Maxwell’s equations and gives rise to secondary radiation that couples the evolution of each quantum dot. By employing an integral equation framework to describe this radiation, we recover fields with a high degree of accuracy at both extremely short and extremely long length scales. We find that pairs of exceptionally close quantum dots have a greatly diminished response to an incident pulse; we attribute this effect to a dynamical detuning that brings the pair out of resonance with the external driving field. Larger assemblages of quantum dots, however, display a much richer behavior: we observe spatially-localized regions of increased and diminished polarization as well as multiple frequency generation in the nonlinear polarization response of particular quantum dots.

The integral equation methodology of chapter 3 has an implicit $\mathcal{O}(n^2)$ spatial complexity because of the pairwise interactions between quantum dots. In practice, this limits simulations to several tens of thousands of particles. To overcome this bottleneck, chapter 4 develops a FFT-based acceleration scheme that exploits the translational invariance of the radiation kernel to greatly reduce the spatial complexity of the calculation. Moreover, our acceleration scheme retains a strong-form integral formulation and makes no assumptions about the underlying computational basis functions to effect propagation. We give preliminary results that depict the accuracy and speed of the method and demonstrate that we can recover fields under the action of an arbitrary linear operator to the precision of the underlying machine.

5.2 Discussion

5.2.1 Advanced dissipators

Designed to provide a semblance of spontaneous emission within a semiclassical framework, the two-level dissipator in eq. (3.2b) works to remove internal energy from each quantum dot system and return it to the ground state. A semiclassical radiation model will never fully describe spontaneous emission due to the lack of a quantized electromagnetic field, but more robust operators that couple the dissipation terms of multiple quantum dots together may more accurately model cooperative phenomena such as four-wave mixing or superradiance. To derive the structure of one such advanced dissipator, consider first a two-quantum dot system with particles A and B . Without rigorous derivation, a coupled dissipator evolves the particles according to

$$\frac{d\hat{\rho}}{dt} = \frac{-i}{\hbar} [\hat{\mathcal{H}}_a^0 + \hat{\mathcal{H}}_b^0, \hat{\rho}] + \sum_{\substack{m \in \{A,B\} \\ n \in \{A,B\}}} \frac{\gamma_{mn}}{2} (2\hat{\sigma}_m^- \hat{\rho} \hat{\sigma}_n^+ - \hat{\sigma}_m^+ \hat{\sigma}_n^- \hat{\rho} - \hat{\rho} \hat{\sigma}_m^+ \hat{\sigma}_n^-). \quad (5.1)$$

Assuming $\hat{\rho} \approx \hat{\rho}_A \otimes \hat{\rho}_B$ and tracing over B to remove its degrees of freedom,

$$\frac{d\hat{\rho}_A}{dt} = \frac{-i}{\hbar} [\hat{\mathcal{H}}_{A'}^0, \hat{\rho}_A] + \hat{\mathcal{D}}_{AA} + \hat{\mathcal{D}}_{AB} \quad (5.2)$$

where

$$\hat{\mathcal{D}}_{AA} = \gamma_{AA} \begin{pmatrix} -\rho_{11}^A & -\rho_{10}^A/2 \\ -\rho_{01}^A/2 & \rho_{11}^A \end{pmatrix} \quad (5.3a)$$

$$\hat{\mathcal{D}}_{AB} = \frac{\gamma_{AB}}{2} \begin{pmatrix} -\rho_{10}^A \rho_{01}^B - \rho_{10}^B \rho_{01}^A & \rho_{11}^A \rho_{10}^B - \rho_{10}^B \rho_{00}^A \\ \rho_{01}^B \rho_{11}^A - \rho_{00}^A \rho_{01}^B & \rho_{01}^B \rho_{10}^A + \rho_{01}^A \rho_{10}^B \end{pmatrix} \quad (5.3b)$$

$$\gamma_{mn} = \frac{4}{3} \omega^3 |\mathbf{d}|^2 \left(J_0(r_{mn}) + P_2(\cos \theta_{mn}) J_2(r_{mn}) \right) \quad (5.3c)$$

Finally, J_ℓ and P_ℓ denote the Bessel function and Legendre polynomial of order ℓ , respectively. Note that the first two terms on the right side of eq. (5.2) give the evolution equation defined in chapter 3. The additional $\hat{\mathcal{D}}_{AB}$ dissipator, then, has terms proportional

to the product of A and B 's coherences/off-diagonal terms with a long-range inverse- r scaling due to the J_0 Bessel function. These terms afford a mechanism for A and B to influence each other's dynamics more directly than through an intermediate radiation field alone.

In a many-particle system, eq. (5.2) expands to include pairwise dissipators that perturb the evolution of every particle due to the assumption of a rank-deficient $\hat{\rho}$. Thus,

$$\frac{d\hat{\rho}_m}{dt} = \frac{-i}{\hbar} [\hat{\mathcal{H}}_m^0, \hat{\rho}_m] + \sum_n \gamma_{mn} \hat{\mathcal{D}}_{mn}. \quad (5.4)$$

Evaluating eq. (5.4) for each of N then scales as $O(N^2)$, making it infeasible to use in large simulations. Fortunately, the kernel-agnostic nature of QuEST makes it relatively straightforward to develop FFT-accelerated interactions of the form in eq. (5.3) alongside those used to describe electromagnetic fields.

5.2.2 Micromagnetics

The Landau-Lifshitz-Gilbert (LLG) equation,

$$\frac{d\mathbf{M}}{dt} = -\gamma' \mathbf{M} \times \mathbf{H} - \lambda \mathbf{M} \times \mathbf{M} \times \mathbf{H} \quad (5.5)$$

where

$$\gamma' = \frac{\gamma_0}{1 + \gamma^2 \eta^2 M_s^2} \quad (5.6a)$$

$$\lambda = \frac{\gamma_0^2 \eta}{1 + \gamma^2 \eta^2 M_s^2} \quad (5.6b)$$

details the evolution of magnetization, \mathbf{M} , in response to an applied magnetic field, \mathbf{H} [2].

In these equations, γ_0 denotes the electron gyromagnetic ratio

$$\gamma_0 = \frac{g|e|\hbar}{2m_e c}, \quad (5.7)$$

η represents a material-dependent damping parameter, and $g, e, m_e,$ & c stand for the Landé g -factor, elementary charge, electron mass, and speed of light, respectively. Simulating the evolution of the Landau-Lifshitz-Gilbert equation at the level of individual particles stands ready to offer novel perspectives into spintronics or other mesoscale systems.

5.2.2.1 Technical details

Immediately, eq. (5.5) draws a large number of parallels with the material equation of chapter 3. Apart from the obvious first-order and vector nature of both equations, the dual nature of electromagnetism means that \mathbf{M} (as a source in Maxwell's equations) relates to \mathbf{H} in the exact same way that \mathbf{P} relates to \mathbf{E} . By simply exchanging some of the physical constants, then, eq. (3.3) also describes radiation emanating from a magnetization distribution [64].

Solving eq. (5.5) within a semiclassical radiation framework requires a little more care than an equivalent Bloch problem, however. Equation (3.1) describes the evolution of a quantum wavefunction—a vector in “Bloch space”—that generates an electromagnetic source distribution through application of an operator (see the discussion surrounding eqs. (3.2) and (3.11) on pages 26 to 29 for an illustration of this point). As a result, the dynamics of eq. (3.1) describe the evolution of a dipole's amplitude but not its orientation and we may employ separate spatial and temporal discretizations to effect a numerical analysis. Moreover, this allow for systems with zero initial polarization ($\mathbf{P} = 0$ in an eigenstate of the unperturbed Hamiltonian, e.g. $\hat{\rho} = |0\rangle\langle 0|$ or $\hat{\rho} = |1\rangle\langle 1|$), thus the external pulse induces all of the dynamical behavior. This makes for a far easier simulation as sources/fields before the start of the simulation do not require any specification.

On the other hand, eq. (5.5) determines the trajectory of an electromagnetic source vector in both (real, Cartesian, directional) space and time with no ability to decouple the dimensions beyond

$$\mathbf{M}(t) = m_x(t)\hat{\mathbf{x}} + m_y(t)\hat{\mathbf{y}} + m_z(t)\hat{\mathbf{z}}. \quad (5.8)$$

QuEST accommodates histories of any numeric type (scalar or tensor, real or complex) through careful templating, and so building a propagator for eq. (5.5) does not present much difficulty aside from some extra index tracking. Equation (5.5) also has an implicit

normalization condition, however, in that

$$\frac{d|\mathbf{M}|}{dt} = 0. \quad (5.9)$$

This presents a larger computational challenge as it implies particles/magnetic domains/“spins” always interact—even before the start of a simulation in a manner not dissimilar to molecular dynamics simulations. The mechanism behind the predictor/corrector algorithm—updating a source distribution and then reincorporating that into the electromagnetic fields before advancing the timestep—will accommodate these interactions without issue but meaningful simulations will require an equilibration period of order $\mathcal{O}(r_{\max}/c)$ before collecting data.

APPENDICES

APPENDIX A
QUEST MANUAL

A.1 Design philosophy

The collection of formulas and algorithms in this thesis provide a mathematical foundation upon which one can implement a simulation tool. This section gives some details on v0.2.1 of the **Quantum Electromagnetics Simulation Toolbox (QuEST)** reference implementation, available at [35]. Written in C++, QuEST has minimal external dependencies, using only the Boost Multiarray and Program Options libraries [1], the Eigen linear algebra library [39], and FFTW [31].

As a scientific endeavor, QuEST largely emphasizes reproducibility, ease of extension, and execution speed. Reproducibility demands modularity to allow well-tested pieces to combine in a recordable manner reminiscent of experiments, thus the main functionality of QuEST resides within a library of independently-constructed objects that interface

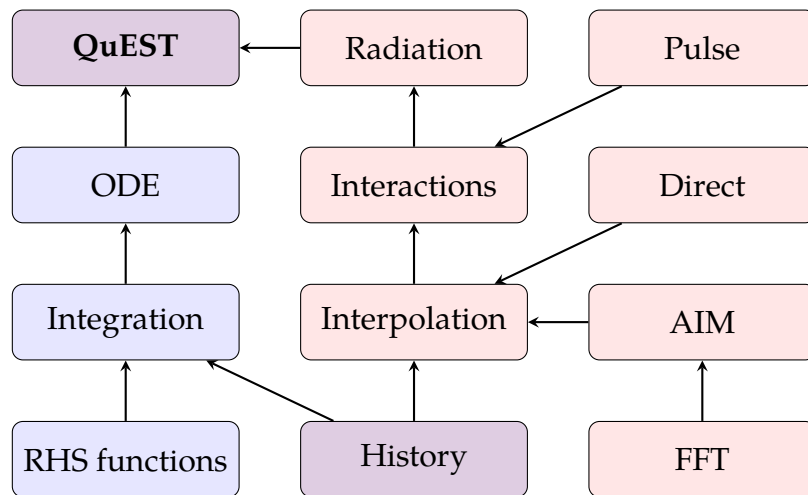


Figure A.1: Hierarchy of the major pieces of QuEST. While a true class diagram would depict the inheritance relationships of the objects that comprise the QuEST library, These blocks *roughly* indicate the interdependence of the program pieces that form QuEST, akin to a class hierarchy (though avid software developers should not take this literally).

with each other. These objects have appropriate constructors to set the parameters of the simulation and slot together to build an executable. For example, to isolate the ODE solver’s behavior from the tricky numerics of the propagation code, the ODE solver only requires the definition of a right-hand side (an RHS) (see section A.2). Coding an RHS with a well-known solution, such as $f'(x) = -\lambda f(x)$, can validate the numerics of the integration step independent of the propagation calculations.

Similarly, making QuEST easy to extend necessitates encapsulating mathematical statements as tightly as possible with these objects. As the project grows to encapsulate new phenomena/models, only the pieces that directly represent the mathematics need to change, not how they fit into the rest of the simulation framework. Unfortunately, these factors often lead to seemingly-unintelligible code. What follows contains a brief discussion of the major pieces of QuEST and why I designed them the way I did.

A.2 Descriptions

cmplx An alias for `std::complex<double>` with an identical bit structure to FFTW’s `fftw_complex` type (hence the use of `static_cast` when interfacing with FFTW).

Configuration This struct effectively contains “global” simulation parameters—the speed of light, number of particles, total time, etc. Most objects do not read these values directly, instead preferring to have them as a parameter in their constructor to enhance modularity. The `parse_configs` function uses the Boost Program Options [1] library to provide a clean, error-checked way of reading these values from specified files.

QuantumDot Collection of parameters necessary to define a quantum dot (position, transition frequency, decay times, and dipole moment). Also provides a method to calculate the right-hand side of eq. (3.4) given an input density matrix and electric field. Because these right-hand sides have instance-dependent parameters (transition frequency, T_1 and T_2 , etc.), `std::bind` produces the appropriate functors for constructing `Integrator::RHS` instances.

Pulse Mathematical description of a Gaussian pulse. Provides a method to evaluate a pulse at a given spacetime coordinate, as well as methods to read/record Pulse objects from/to a file.

UniformLagrangeSet Tool to evaluate Lagrange polynomials and their derivatives. Upon construction, each instance allocates a workspace table (to avoid reallocation overhead) to contain the evaluated interpolants and their derivatives. This object uses the definition of Lagrange polynomials and logarithmic derivatives, $\frac{d}{dx} \log f(x) = f'(x)/f(x)$, to efficiently fill each column (the interpolant and two derivatives) of the table simultaneously.

TransformPair Struct to manage FFTW plans (pointers). Constructed with a forward and backward plan and automatically de-allocates both in its destructor to avoid memory leaks.

Interaction Abstract base-class to provide an interface for calculating an interaction for each QuantumDot in an array. Each Interaction contains a shared pointer to a `std::vector<QuantumDot>` and allocates a complex-valued Eigen row-vector (once, to avoid reallocation overhead) upon construction. This row-vector serves as a workspace in which to place interaction values in the evaluate method before returning. Ultimately subclasses into `PulseInteraction`, `DirectInteraction`, and `AimInteraction`.

PulseInteraction Calculates and returns $\mathbf{d} \cdot \mathbf{E}_{\text{inc}}/\hbar$ at the location of each QuantumDot at a specified time.

DirectInteraction (subclass of `HistoryInteraction`) Calculates and returns $\mathbf{d} \cdot \mathbf{E}_{\text{rad}}/\hbar$ at the location of each QuantumDot (where \mathbf{E}_{rad} depends on the history of every other QuantumDot due to retardation effects). This object stores the space/-time interaction matrix elements between each QuantumDot directly, assuming reciprocity and no self interactions (effectively the lower triangle of the matrix).

Uses Lagrange interpolation to calculate quantities “between” timesteps as well as temporal derivatives.

AIMInteraction (subclass of `HistoryInteraction`) Calculates $\mathbf{d} \cdot \mathbf{E}_{\text{rad}}/\hbar$ between well-separated sources (so as to avoid incurring undue approximation error). Uses the vastly more efficient AIM (FFT) framework to reduce the storage and accelerate the matrix-vector products. Uses Lagrange interpolation to calculate quantities “between” timesteps as well as temporal derivatives. **WARNING:** you *must* call `AIMInteraction.evaluate` with sequential arguments (starting at zero, corresponding to sequential timesteps) due to the way this object fills internal tables. This keeps the indexing correct as later calls to `evaluate` depend on the results of previous calculations.

Grid Class to construct and manage a representation of the auxiliary AIM grid. Provides methods to convert between grid coordinates ($n_x, n_y,$ and n_z integers that index a node in the grid), a grid index (linearization of the grid coordinates to a single integer index starting at zero), and spatial coordinates ($\mathbf{r} = x\hat{\mathbf{x}} + y\hat{\mathbf{y}} + z\hat{\mathbf{z}}$ real-valued coordinates in three-dimensional space).

ExpansionFunction Complicated black magic sorcery. Stay away.

ExpansionTable Table of dimension [number of sources][number of points each source expands into] containing the thirteen $(\partial_0, \partial_x, \dots, \partial_{yz}, \partial_{zz})$ expansion weights relating each source to its immediate (i.e. not trivially zero) auxiliary grid points.

LeastSquaresExpansionSolver Utility class to build and solve the least-squares system in eq. (4.9). Uses a named constructor to avoid creating a persistent instance that implicitly depends on a non-`const` `Grid` (only the static `get_expansions` function can instantiate a `LeastSquaresExpansionSolver` and thus will call its destructor when the function returns).

PredictorCorrector Implementation of the exponentially-fitted predictor/corrector scheme in [33]. Implemented as a template class so as to allow solution of arbitrary ODEs (scalar/vector, real/complex, etc.).

Weights Assistance class for solving the matrix equation that determines the predictor/corrector weights. Putting the code for these matrices into its own object automatically frees the resources used to store them (by automatically calling the object's destructor when it goes out of scope) after calculating the required values.

History Wrapper around a three-dimensional `Boost::multi_array` to store data for coupled first-order ODEs at fixed solution points (timesteps). Stores both a solution and its derivative (the "RHS") for each of N_s ODEs at N_t solution points, indexed by [equation index][time index][derivative index]. Provides integer-equivalent **typedefs** to assist with indexing. As the predictor/corrector integration scheme requires a history to solve for any timepoint (including the first), these arrays extend the time axis backwards to negative indices so as to always start at $t = 0$.

APPENDIX B

THE PREDICTOR/CORRECTOR INTEGRATION SCHEME

B.1 Motivation

Given an ordinary differential equation,

$$\frac{dx}{dt} = f(t, x(t)) \quad (\text{B.1})$$

and some initial condition at t_0 , we may compactly write the unknown function at any discrete time $t_i \equiv i \Delta t$ as

$$\begin{aligned} x(t_i) &= x(t_{i-1}) + \int_{t_{i-1}}^{t_i} \frac{dx}{dt'} dt' \\ &\equiv x(t_{i-1}) + \int_{t_{i-1}}^{t_i} f(t', x(t')) dt' \end{aligned} \quad (\text{B.2})$$

Numerical integration schemes advance a solution from t_{i-1} to t_i by approximating this integral, often as a weighted sum of the integrand evaluated at intelligently chosen points within the interval¹. This process—particularly evaluating the integrand—becomes vastly more complicated through the introduction of retardation effects, effectively turning eq. (B.1) into

$$\frac{dx}{dt} = f(t, x(t), x(t - \tau_1), x(t - \tau_2), \dots). \quad (\text{B.3})$$

Causality imposed by the propagation operators only requires $\tau_j > 0$, thus eq. (B.3) can relate a derivative to quantities arbitrarily far back in time, often between the discrete t_i /known solution values. Further problems arise when $\tau_j < \Delta t$; in such cases, the unknown $x(t_i)$ depends on an unknown $x(t_i - \tau_j)$ which depends on an unknown $x(t_i - 2\tau_j)$ etc., at least one of which lies “ahead” of the last known quantity, $x(t_{i-1})$. While adjusting the timestep to require $\tau_j \geq \Delta t$ makes the system perfectly causal, it also makes the timestep

¹Many numerical integrators use much more sophisticated methods than a weighted sum, but the idea of intelligently evaluating the integrand remains the same.

prohibitively small for dense systems. These constraints automatically exclude (or at least *severely* limit the utility of) popular ODE algorithms and packages—the difficulty of re-evaluating interactions prohibits variable-timestep integrators and integrators that require midpoint evaluations (such as the popular RK4 method) cannot accommodate small retardation factors without an exceptionally small Δt . Instead, we turn to the exponentially-fitted predictor/corrector algorithm detailed in [33]. As a multistep method, the predictor/corrector does not require any function evaluations outside of those on the fixed timepoints, thus any causal interpolation scheme facilitates evaluating approximate versions of all the $x(t - \tau_j)$ via

$$x(t_i - \tau_j) \approx \sum_{\ell=0}^m w_\ell x(t_i - (\lfloor \tau_j / \Delta t \rfloor + \ell) \Delta t). \quad (\text{B.4})$$

(The particular interpolation scheme determines the w_ℓ .) For $\tau_j < \Delta t$, eq. (B.4) suggests $x(t_i - \tau_j)$ becomes a function of $x(t_i)$. Ordinarily, this would cause problems though the predictor step of the algorithm ensures an approximate $x(t_i)$ exists before any interpolation. The corrector step then works to correct this approximation in a convergent way, reincorporating adjacent sources as a total solution evolves.

B.2 Integration coefficients

Let $x(t)$ denote the solution to a given ordinary differential equation. We seek to approximate $x(t)$ as a linear combination of complex-valued exponentials such that

$$x(t) \approx \sum_{\ell=0}^{N_\lambda-1} w_\ell e^{\lambda_\ell t} \quad (\text{B.5})$$

for a given set of complex-valued λ_ℓ arguments and w_ℓ weights (never calculated explicitly). As we wish to capture the behavior of physical systems—i.e. systems with exclusively oscillating and decaying modes—we choose the λ_ℓ to lie within the left half of the complex plane. Moreover, assuming $x(t)$ contains little power above some threshold ω_{\max} , we select the λ_ℓ from within $S = \{z \in \mathbb{C} \mid \text{Re}\{z\} \leq 0, |z| \leq \omega_{\max}\}$: the left semidisk of radius ω_{\max} (fig. B.2a). Finally, rather than choosing λ_ℓ from throughout S , the maximum modulus

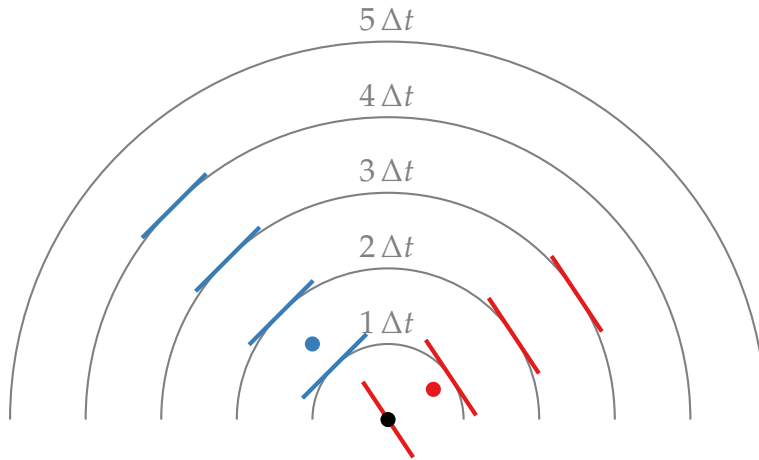


Figure B.1: Illustration of the “retardation problem” in solving coupled delay differential equations. If $\partial_t x_{\bullet}(t) = f(x_{\bullet}(t - |\mathbf{r}_{\bullet\bullet}|) + x_{\bullet}(t - |\mathbf{r}_{\bullet\bullet}|))$ then determining $x_{\bullet}(t - |\mathbf{r}_{\bullet\bullet}|)$ and $x_{\bullet}(t - |\mathbf{r}_{\bullet\bullet}|)$ requires some sort of interpolation scheme. Evaluating $\partial_t x_{\bullet}(t)$ in hopes of obtaining $x_{\bullet}(t)$ therefore requires knowledge of $x_{\bullet}(t)$. The converse holds as well;—evaluating $\partial_t x_{\bullet}(t)$ requires knowledge of $x_{\bullet}(t)$ which poses problems in evaluating the derivatives simultaneously. The predictor step of the integrator overcomes this issue by providing a stable extrapolation of past quantities to provide a guess value of $x_{\bullet}(t)$ and $x_{\bullet}(t)$.

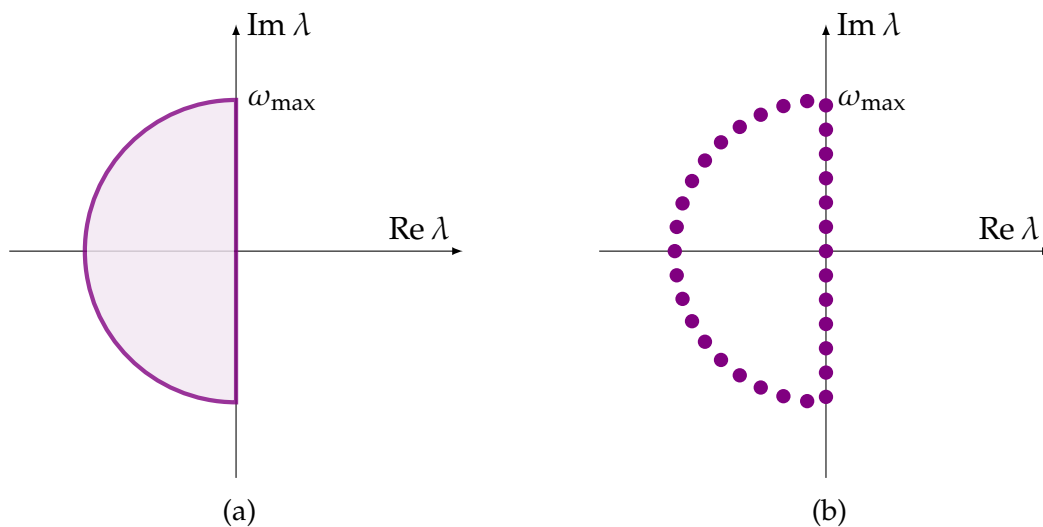


Figure B.2: Selection of the λ_n parameters used in determining the predictor/corrector coefficients.

principle ensures that arguments taken from the boundary of S in fig. B.2b will incur the maximum approximation error in eq. (B.5). As a result, an approximation using λ_ℓ chosen from the boundary of S accurately recovers the behavior of all modes with arguments in S . In particular, we choose the λ_ℓ to have an equal spacing about the perimeter of S (fig. B.2b).

If $x(t)$ and $\partial_t x(t)$ have known values at equidistant points t_0, t_1, \dots, t_{W-1} on the interval $[-1, 1]$ (thus $\Delta t = 2/(W - 1)$), we predict the value of $x(t_W)$ as a linear combination of past values and derivatives,

$$x(t_W) \leftarrow \sum_{j=0}^{W-1} p_j x(t_j) + p_{j+W} \partial_t x(t_j). \quad (\text{B.6})$$

Inserting eq. (B.5) into eq. (B.6) gives the matrix equation

$$A\mathbf{p} = \mathbf{b} \quad (\text{B.7})$$

where

$$A_{ij} = \begin{cases} e^{\lambda_i t_j}, & 0 \leq i < N_\lambda; 0 \leq j < W \\ \lambda_i e^{\lambda_i t_{j-W}}, & 0 \leq i < N_\lambda; W \leq j < 2W \end{cases} \quad (\text{B.8a})$$

$$b_i = e^{\lambda_i t_W}. \quad (\text{B.8b})$$

Solving this equation for \mathbf{p} , then, produces the prediction coefficients in eq. (B.6). Accordingly, we use a minimum-norm least-squares procedure to determine \mathbf{p} . Having conjured an (approximate) value for $x(t_W)$, we may evaluate the prescribed ODE to obtain a value for $\partial_t x(t_W)$. Writing

$$x(t_W) \leftarrow \left(\sum_{j=0}^{W-1} c_j x(t_j) + c_{W+j} \partial_t x(t_j) \right) + c_{2W} \partial_t x(t_W), \quad (\text{B.9})$$

this new equation reincorporates derivative information to refine the $x(t_W)$ approximation, requiring only a means of determining the c_j . Again, inserting eq. (B.5) gives

$$\tilde{A}\mathbf{c} = \mathbf{b}. \quad (\text{B.10})$$

Here,

$$\tilde{A}_{ij} = \begin{cases} A_{ij}, & 0 \leq i < N_\lambda; 0 \leq j < 2W \\ \lambda_i e^{\lambda_i t_W}, & 0 \leq i < N_\lambda; j = 2W \end{cases} \quad (\text{B.11})$$

b remains unchanged, and the same least-squares procedure determines **c**.

Having derived the predictor/corrector coefficients for $h = 2/(W - 1)$ —i.e. a uniform spacing between W timepoints on the interval $[-1, 1]$ —the coefficients determined above require only a slight modification to accommodate systems with any Δt . Noting that the formulation thus far remains invariant under time translation and that the substitution $\tau = \alpha t$ (equivalently $\alpha = \Delta t/h$) turns

$$\frac{\partial \varphi(t)}{\partial t} = \lambda \varphi(t) \quad (\text{B.12a})$$

into

$$\frac{\partial \varphi(\tau)}{\partial \tau} = \frac{\lambda}{\alpha} \varphi(\tau), \quad (\text{B.12b})$$

we need only scale the coefficients multiplying $\partial_t x(t_j)$ by α to adjust for other step sizes.

APPENDIX C

CHEBYSHEV POLYNOMIALS

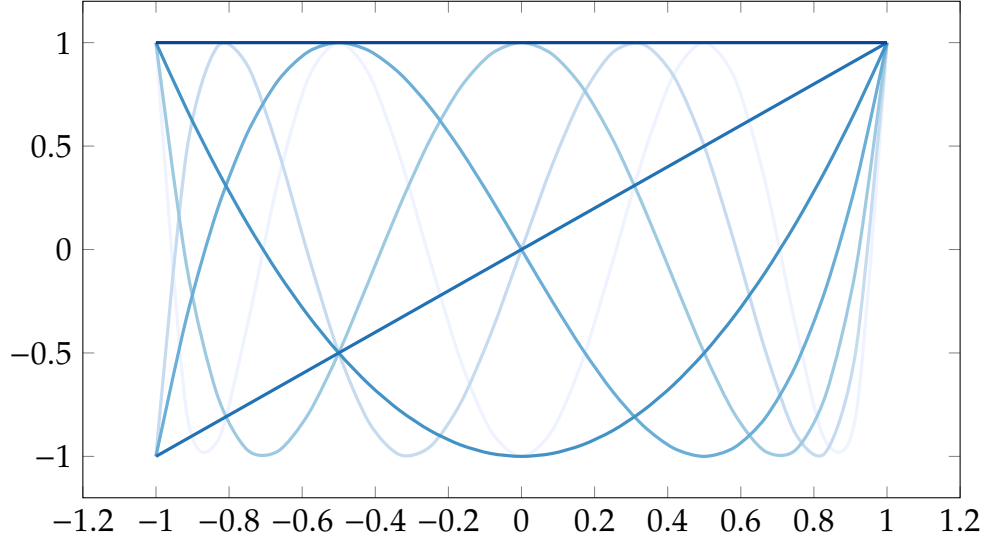


Figure C.1: Chebyshev polynomials $T_0(x)$ through $T_6(x)$. The roots of $T_{m+1}(x)$ give the sample points for an interpolation scheme of order m on the interval $[-1, 1]$.

The Chebyshev polynomials of the first kind, defined by

$$T_n(x) = \cos(n \arccos(x)) \tag{C.1}$$

and shown in fig. C.1, form an orthogonal (though not orthonormal) sequence well-suited to interpolation. These polynomials have a continuous orthogonality relation over the interval $-1 \leq x \leq 1$ with respect to $w(x) = (1 - x^2)^{-1/2}$, giving

$$\int_{-1}^1 \frac{T_i(x)T_j(x)}{\sqrt{1-x^2}} dx = \begin{cases} 0 & i \neq j \\ \pi/2 & i = j \neq 0 \\ \pi & i = j = 0 \end{cases} \tag{C.2}$$

Such an orthogonality motivates $\{T_k(x) : k = 0, 1, \dots, m\}$ as a basis for \mathbb{P}^m —the polynomials through order m —on the interval $-1 \leq x \leq 1$. To construct a polynomial interpolation

of an arbitrary function $f(x)$ in this basis such that

$$\begin{aligned} f(x) &\approx P_m(x) \\ &\equiv \sum_{i=0}^m c_i T_i(x), \end{aligned} \quad (\text{C.3})$$

we require samples of the function at $m + 1$ interpolation nodes¹ $\{x_\lambda : \lambda = 0, 1, \dots, m\}$ where $f(x_\lambda) = P_m(x_\lambda)$. By choosing sample points corresponding to Chebyshev nodes,

$$x_\lambda = -\cos\left(\frac{\pi(\lambda + 1/2)}{m + 1}\right) \quad \lambda = 0, 1, 2, \dots, m, \quad (\text{C.4})$$

the Chebyshev polynomials satisfy [32]

$$\sum_{\lambda=0}^m T_i(x_\lambda) T_j(x_\lambda) = \begin{cases} 0 & i \neq j \\ (m + 1)/2 & i = j \neq 0 \\ m + 1 & i = j = 0 \end{cases} \quad (\text{C.5})$$

in addition to the continuous relationship in eq. (C.2). Inserting eq. (C.3) into eq. (C.5) then gives

$$\sum_{\lambda=0}^m T_i(x_\lambda) f(x_\lambda) = \sum_{\lambda=0}^m T_i(x_\lambda) P_m(x_\lambda) = \sum_{i=0}^m c_i \sum_{\lambda=0}^m T_i(x_\lambda) T_i(x_\lambda) \quad (\text{C.6})$$

thus

$$c_i = \frac{\alpha_i}{m + 1} \sum_{\lambda=0}^m T_i(x_\lambda) f(x_\lambda) \quad \alpha_i = 2 - \delta_{i0}. \quad (\text{C.7})$$

Finally, having obtained a Chebyshev approximation of $f(x)$ on the interval $-1 \leq x \leq 1$, we may effect a Chebyshev approximation of $f(x)$ on the interval $a \leq x \leq b$ by letting

$$y \equiv \frac{x - (b + a)/2}{(b - a)/2} \quad (\text{C.8})$$

and constructing a Chebyshev approximation in y .

¹For convenience, Latin letters index *functions* while Greek letters index *points*.

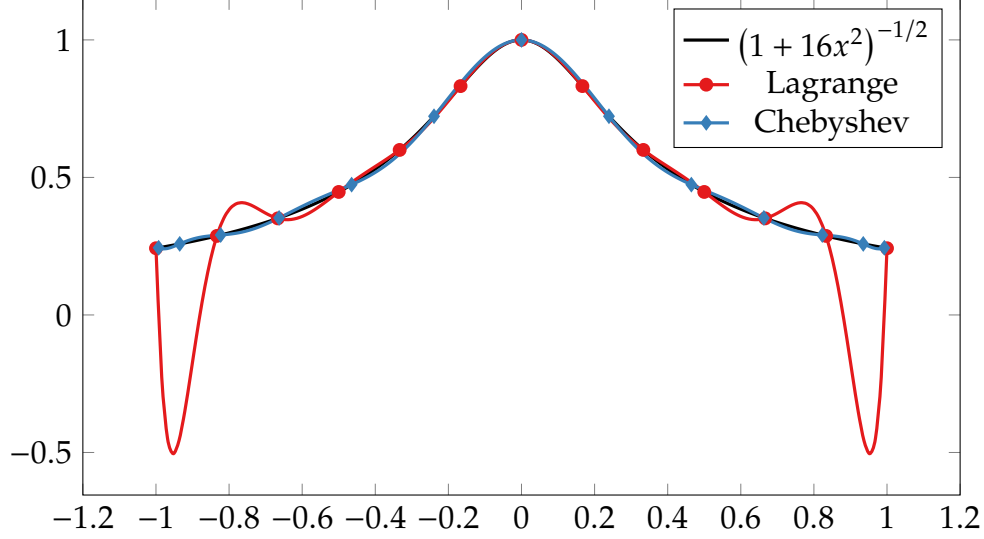


Figure C.2: Interpolation of a pathological function, $f(x) = (1 + 16x^2)^{-1/2}$, using Chebyshev and equally-spaced Lagrange interpolation schemes. Because the Chebyshev scheme clusters sample points in the tails of the interpolation window, it does not suffer from high-order ringing effects (Runge's phenomenon).

C.1 Notes on the Chebyshev polynomials

C.1.1 Derivatives

The Chebyshev polynomials provide two means of approximating $f'(x)$ given samples of $f(x)$ though both have numerical drawbacks. Given that we wish to repeatedly evaluate the interpolating polynomial at a collection of static points, it becomes prudent to pre-evaluate and cache $T_i(x)$ in eq. (C.3) for speed. The recurrence

$$(1 - x^2)T'_n(x) = n[T_{n-1}(x) - xT_n(x)] \quad (\text{C.9})$$

analytically relates Chebyshev polynomials to their derivatives, and so we may equivalently cache $T'_n(x)$ to repeatedly evaluate a derivative. Unfortunately, this becomes problematic for $x \rightarrow \pm 1$ as the $1 - x^2$ term can cause a catastrophic loss of precision due to division by (near) zero. Instead,

$$c'_{i-1} = c'_{i+1} + 2ic_i \quad c'_{m+1} = c'_m = 0 \quad (\text{C.10})$$

adjusts the Chebyshev coefficients to give an approximated derivative in terms of the original basis. While this expression does not suffer from numerical cancellation issues, it incurs a large amount of overhead when evaluating many approximations. Moreover, this overhead grows significantly in higher-dimensional systems with vector derivatives.

In practice, QuEST makes use of the former strategy of differentiating the “evaluating functions” though without the recurrence of eq. (C.9). Instead, functions for the Chebyshev polynomials and their derivatives through a specified order, provide the necessary evaluations. Moreover, these functions contain the requisite polynomials expressed in Horner form to improve both speed and precision [52]. While this method does not readily generalize to interpolations of arbitrary order (as it would require prohibitively long enumerations of functions), it nevertheless facilitates an efficient derivative evaluation without unduly sacrificing clarity.

C.1.2 Higher-dimensional approximations

The mechanics for constructing an approximation to $f(x)$ extend naturally to higher-dimensional and vector-valued systems. In such systems, the Chebyshev approximation becomes a tensor polynomial, and the summations in eqs. (C.3) and (C.7) become mondo tensor contractions, i.e.

$$\mathbf{f}(\mathbf{r}) \approx \mathbf{c}_{ijk} T_i(x) T_j(y) T_k(z), \quad (\text{C.11a})$$

$$\mathbf{c}_{ijk} = \frac{\alpha_{ii'} \alpha_{jj'} \alpha_{kk'}}{(m+1)^3} T_{ii'}(x_\lambda) T_{jj'}(y_\mu) T_{kk'}(z_\nu) \mathbf{f}(x_\lambda, y_\mu, z_\nu) \quad (\text{C.11b})$$

with an implied summation over the bound indices i', j', k' and λ, μ, ν . QuEST makes use of the Tensor Algebra Compiler (taco) [51] to generate the equivalent source-expression for eq. (C.11b) with dense tensors (listing C.1).

Listing C.1: C-source expression for eq. (C.11b).

```
for (int32_t boxeval = 0; boxeval < num_boxes; boxeval++) {
    double tbox = norm;
```

```

for (int32_t ialphas = 0; ialphas < size; ialphas++) {
    int32_t pcoef2 = boxeval * size + ialphas;
    double ti = tbox * alphas_[ialphas];
    for (int32_t lambdachebS = 0; lambdachebS < size; lambdachebS++) {
        int32_t pchebS2 = ialphas * size + lambdachebS;
        int32_t peval2 = boxeval * size + lambdachebS;
        double tlambd = ti;
        double tlambd0 = chebS[pchebS2];
        for (int32_t jalphas = 0; jalphas < size; jalphas++) {
            int32_t pcoef3 = pcoef2 * size + jalphas;
            double tj = tlambd * alphas_[jalphas];
            double tj0 = tlambd0;
            for (int32_t muchebS = 0; muchebS < size; muchebS++) {
                int32_t pchebS20 = jalphas * size + muchebS;
                int32_t peval3 = peval2 * size + muchebS;
                double tmu = tj;
                double tmu0 = tj0;
                double tmul = chebS[pchebS20];
                for (int32_t kalphas = 0; kalphas < size; kalphas++) {
                    int32_t pcoef4 = pcoef3 * size + kalphas;
                    double tk = tmu * alphas_[kalphas] * tmu0 * tmul;
                    for (int32_t nuchebS = 0; nuchebS < size; nuchebS++) {
                        int32_t pchebS21 = kalphas * size + nuchebS;
                        int32_t peval4 = peval3 * size + nuchebS;
                        double tnu = tk * chebS[pchebS21];
                        for (int32_t dimeval = 0; dimeval < 3; dimeval++) {
                            int32_t peval5 = peval4 * 3 + dimeval;

```

```
int32_t pcoef5 = pcoef4 * 3 + dimeval;
coef[pcoef5] = coef[pcoef5] + tnu * eval[peval5];
    }
  }
}
}
}
}
}
}
```

APPENDIX D

CONVENTIONS

D.1 Fourier transforms

The definition of the Fourier transform leaves some room to adopt conventions. I write the fully-generalized Fourier transform $f(t) \leftrightarrow F(\omega)$ pair as

$$F(\omega) = \sqrt{\frac{|s_2|}{(2\pi)^{1-s_1}}} \int_{-\infty}^{\infty} f(t) e^{is_2\omega t} dt \quad (\text{D.1a})$$

$$f(t) = \sqrt{\frac{|s_2|}{(2\pi)^{1+s_1}}} \int_{-\infty}^{\infty} F(\omega) e^{-is_2\omega t} d\omega \quad (\text{D.1b})$$

where the s_1, s_2 parameters allow for different normalization and frequency conventions. Of principal importance, eq. (D.1b) implies

$$\partial_t f(t) \leftrightarrow -i\omega s_2 F(\omega). \quad (\text{D.2})$$

The most common *physics* and *engineering* conventions take $\{s_1, s_2\} = \{1, 1\}$ and $\{s_1, s_2\} = \{1, -1\}$, though myriad other discipline-specific conventions exist.

D.2 Maxwell's equations

An unfortunate ambiguity in the prescription of electromagnetic units allows for unit systems that differ by more than simple scaling factors (mega-, kilo-, centi-, etc.)—the placement of physical constants in equations changes as well. In a unit-independent format, Maxwell's equations become [45]

$$\nabla \cdot \mathbf{E} = 4\pi k_1 \rho \quad (\text{D.3a})$$

$$\nabla \times \mathbf{B} = 4\pi k_2 \alpha \mathbf{J} + \frac{k_2 \alpha}{k_1} \frac{\partial \mathbf{E}}{\partial t} \quad (\text{D.3b})$$

$$\nabla \cdot \mathbf{B} = 0 \quad (\text{D.3c})$$

$$\nabla \times \mathbf{E} = -k_3 \frac{\partial \mathbf{B}}{\partial t} \quad (\text{D.3d})$$

with k_1 , k_2 , α , and k_3 as system-dependent constants. One need only specify two of the four constants to pin down the unit system, however; in particular

$$\frac{k_1}{k_2 k_3 \alpha} = c^2 \quad \text{and} \quad k_3 = \frac{1}{\alpha}. \quad (\text{D.4})$$

From eq. (D.3c), $\mathbf{B} = \nabla \times \mathbf{A}$. Then, using eq. (D.3d), it becomes apparent that

$$\nabla \times \left(\mathbf{E} + k_3 \frac{\partial \mathbf{A}}{\partial t} \right) = 0$$

so I may take

$$\mathbf{E} = -\nabla\varphi - k_3 \frac{\partial \mathbf{A}}{\partial t}.$$

Thus, in electrostatic systems, $\mathbf{E} = -\nabla\varphi$ regardless of units. By eq. (D.3a), then,

$$\nabla^2 \varphi = -4\pi k_1 \rho$$

and thus

$$\varphi(\mathbf{r}) = \int \frac{k_1 \rho(\mathbf{r}')}{|\mathbf{r} - \mathbf{r}'|} d^3 \mathbf{r}'$$

as

$$\nabla^2 \left(\frac{1}{|\mathbf{r} - \mathbf{r}'|} \right) = -4\pi \delta(\mathbf{r} - \mathbf{r}').$$

This defines the *Laplace-kernel Green's function* as

$$g(\mathbf{r}) \equiv \frac{1}{|\mathbf{r}|}. \quad (\text{D.5})$$

Analogously, the *Helmholtz-kernel* and *Wave-kernel* Green's functions become

$$g(\mathbf{r}; k) \equiv \frac{e^{ik|\mathbf{r}|}}{|\mathbf{r}|} \quad g(\mathbf{r}; t) \equiv \frac{\delta(t - |\mathbf{r}|/c)}{|\mathbf{r}|} \quad (\text{D.6})$$

D.2.1 Vector wave equation

D.2.1.1 Operator form

From eqs. (D.3b) and (D.3d),

$$\nabla \times \nabla \times \mathbf{E} + \frac{1}{c^2} \frac{\partial^2 \mathbf{E}}{\partial t^2} = -4\pi k_2 \frac{\partial \mathbf{J}}{\partial t}. \quad (\text{D.7})$$

Taking the divergence of both sides and removing one time derivative,

$$\frac{1}{c^2} \nabla \cdot \frac{\partial \mathbf{E}}{\partial t} = -4\pi k_2 \nabla \cdot \mathbf{J}.$$

As $\nabla \times \nabla \times \mathbf{A} = \nabla(\nabla \cdot \mathbf{A}) - \nabla^2 \mathbf{A}$, the time derivative of eq. (D.7) becomes

$$\nabla \left(\nabla \cdot \frac{\partial \mathbf{E}}{\partial t} \right) - \nabla^2 \frac{\partial \mathbf{E}}{\partial t} + \frac{1}{c^2} \frac{\partial^3 \mathbf{E}}{\partial t^3} = -4\pi k_2 \frac{\partial^2 \mathbf{J}}{\partial t^2}$$

therefore

$$\nabla^2 \frac{\partial \mathbf{E}}{\partial t} - \frac{1}{c^2} \frac{\partial^3 \mathbf{E}}{\partial t^3} = 4\pi k_2 \left(\frac{\partial^2 \mathbf{J}}{\partial t^2} - c^2 \nabla \nabla \cdot \mathbf{J} \right).$$

Immediately, the left-hand side gives the “wave operator” acting on $\partial_t \mathbf{E}$ and thus

$$\frac{\partial}{\partial t} \mathbf{E}(\mathbf{r}, t) = g(\mathbf{r}; t) * -k_2 \left(\frac{\partial^2}{\partial t^2} - c^2 \nabla \nabla \cdot \right) \mathbf{J}(\mathbf{r}, t)$$

from which it follows

$$\mathbf{E}(\mathbf{r}, t) = -k_2 \iint \frac{\delta(t_R - t')}{|\mathbf{r} - \mathbf{r}'|} \left(\frac{\partial^2}{\partial t'^2} - c^2 \nabla' \nabla' \cdot \right) \mathbf{P}(\mathbf{r}', t') d^3 \mathbf{r}' dt' \quad (\text{D.8})$$

where $t_R \equiv t - |\mathbf{r} - \mathbf{r}'|/c$ and $\partial_t \mathbf{P} \equiv \mathbf{J}$.

D.2.1.2 Dyadic form

In addition to eq. (D.8), one may also construct an equivalent propagator without any spatial derivatives in the resulting expression. This form of the propagator has advantages in describing $\mathbf{E}(\mathbf{r}, t)$ when derivatives become ill-defined (for example, fields arising from point sources).

To begin, we note that for time-harmonic $\mathbf{P}(\mathbf{r}, t) = \mathbf{P}(\mathbf{r})e^{-i\omega t}$ eq. (D.8) becomes

$$\mathbf{E}(\mathbf{r}) = -k_2 \int \frac{e^{ik|\mathbf{r}-\mathbf{r}'|}}{|\mathbf{r} - \mathbf{r}'|} \left((-i\omega)^2 - c^2 \nabla' \nabla' \cdot \right) \mathbf{P}(\mathbf{r}') d^3 \mathbf{r}' \quad (\text{D.9})$$

after suppressing the time-harmonic function and taking $k = \omega/c$. All of the terms in this equation commute due to the linearity of the operators, thus

$$\begin{aligned} \mathbf{E}(\mathbf{r}) &= -k_2 (-i\omega)^2 \int \left(\mathbf{I} + \frac{\nabla \nabla}{k^2} \right) \frac{e^{ik|\mathbf{r}-\mathbf{r}'|}}{|\mathbf{r} - \mathbf{r}'|} \cdot \mathbf{P}(\mathbf{r}') d^3 \mathbf{r}' \\ &\equiv -k_2 (-i\omega) \int \mathbf{G}_d(\mathbf{r} - \mathbf{r}'; \omega) \cdot \mathbf{P}(\mathbf{r}'; \omega) d^3 \mathbf{r}' \end{aligned} \quad (\text{D.10})$$

which defines the *dyadic Green's function*

$$\mathbf{G}_d(\mathbf{r}; \omega) = \left(\mathbf{I} + \frac{\nabla \nabla}{k^2} \right) \frac{e^{ikr}}{r}, \quad (\text{D.11})$$

where \mathbf{I} represents the identity dyad.

In spherical coordinates, $\mathbf{G}_d(\mathbf{r}) = G_d(r)$ and the spatial derivatives become particularly easy to compute. Accordingly,

$$\begin{aligned} \nabla \nabla \frac{e^{ikr}}{r} &= \nabla \left(\frac{e^{ikr}}{r^2} (ikr - 1) \hat{\mathbf{r}} \right) \\ &= \hat{\mathbf{r}} \nabla \left(\frac{e^{ikr}}{r^2} (ikr - 1) \right) + \frac{e^{ikr}}{r^2} (ikr - 1) (\nabla \hat{\mathbf{r}}) \\ &= \left[\left(\frac{3}{r^2} - \frac{3ik}{r} - k^2 \right) \hat{\mathbf{r}} \hat{\mathbf{r}} + \left(-\frac{1}{r^2} + \frac{ik}{r} \right) \mathbf{I} \right] \frac{e^{ikr}}{r} \end{aligned} \quad (\text{D.12})$$

Inserting this expression back into eq. (D.11) then gives

$$\begin{aligned} G_d(r) &= \left[\left(\frac{3}{k^2 r^2} + \frac{3}{(ik)r} - 1 \right) \hat{\mathbf{r}} \hat{\mathbf{r}} + \left(-\frac{1}{k^2 r^2} - \frac{1}{(ik)r} + 1 \right) \mathbf{I} \right] \frac{e^{ikr}}{r} \\ &= \left[(\mathbf{I} - \hat{\mathbf{r}} \hat{\mathbf{r}}) - (\mathbf{I} - 3\hat{\mathbf{r}} \hat{\mathbf{r}}) \left(\frac{1}{(ik)r} + \frac{1}{k^2 r^2} \right) \right] \frac{e^{ikr}}{r}. \end{aligned} \quad (\text{D.13})$$

Having eliminated the spatial derivatives, we can perform the inverse of the Fourier transform that gave eq. (D.9). Inserting eq. (D.13) back into eq. (D.10) and replacing k with ω gives

$$\mathbf{E}(\mathbf{r}, \omega) = -k_2 \int \left[(\mathbf{I} - \hat{\mathbf{r}} \hat{\mathbf{r}}) (-i\omega)^2 + (\mathbf{I} - 3\hat{\mathbf{r}} \hat{\mathbf{r}}) \left(c \frac{-i\omega}{r} + \frac{c^2}{r^2} \right) \right] \frac{e^{ikr}}{r} \cdot \mathbf{P}(\mathbf{r}', \omega) d^3 \mathbf{r}' \quad (\text{D.14})$$

where $\hat{\mathbf{r}} = (\mathbf{r} - \mathbf{r}')/|\mathbf{r} - \mathbf{r}'|$. Exchanging $-i\omega$ for a time derivative and restoring the temporal convolution,

$$\mathbf{E}(\mathbf{r}, t) = -k_2 \iint \left[(\mathbf{I} - \hat{\mathbf{r}} \hat{\mathbf{r}}) \frac{\partial_t^2 \delta(t_R - t')}{|\mathbf{r} - \mathbf{r}'|} + (\mathbf{I} - 3\hat{\mathbf{r}} \hat{\mathbf{r}}) \left(\frac{c \partial_t \delta(t_R - t')}{|\mathbf{r} - \mathbf{r}'|^2} + \frac{c^2 \delta(t_R - t')}{|\mathbf{r} - \mathbf{r}'|^2} \right) \right] \cdot \mathbf{P}(\mathbf{r}, t') d^1 t' d^3 \mathbf{r}'. \quad (\text{D.15})$$

The derivatives acting on the δ -functions make little sense, thus we can apply them equally to $\mathbf{P}(\mathbf{r}, t)$ again due to the linearity of the operators. As a result,

$$\mathbf{E}(\mathbf{r}, t) = -k_2 \int (\mathbf{I} - \hat{\mathbf{r}} \hat{\mathbf{r}}) \cdot \frac{\ddot{\mathbf{P}}(\mathbf{r}', t_R)}{|\mathbf{r} - \mathbf{r}'|} + (\mathbf{I} - 3\hat{\mathbf{r}} \hat{\mathbf{r}}) \cdot \left(\frac{c \dot{\mathbf{P}}(\mathbf{r}', t_R)}{|\mathbf{r} - \mathbf{r}'|^2} + \frac{c^2 \mathbf{P}(\mathbf{r}', t_R)}{|\mathbf{r} - \mathbf{r}'|^3} \right) d^3 \mathbf{r}' \quad (\text{D.16})$$

where dots indicate derivatives with respect to t (or, equivalently, t_R).

BIBLIOGRAPHY

BIBLIOGRAPHY

- [1] *BOOST C++ Libraries*. <http://www.boost.org>.
- [2] Amikam Aharoni. *Introduction to the theory of ferromagnetism*. Oxford University Press, Oxford New York, 2000.
- [3] John S Allen, Donovan J May, and Katherine W Ferrara. Dynamics of therapeutic ultrasound contrast agents. *Ultrasound in medicine & biology*, 28(6):805–816, 2002.
- [4] L. Allen and J.H. Eberly. *Optical Resonance and Two-level Atoms*. Dover books on physics and chemistry. Dover, 1975.
- [5] Philip W. Anderson. The question of classical localization: A theory of white paint? *Philosophical Magazine B*, 52(3):505–509, 1985.
- [6] F. Arecchi and R. Bonifacio. Theory of optical maser amplifiers. *IEEE Journal of Quantum Electronics*, 1(4):169–178, July 1965.
- [7] Kenta Asakura, Yasuyoshi Mitsumori, Hideo Kosaka, Keiichi Edamatsu, Kouichi Akahane, Naokatsu Yamamoto, Masahide Sasaki, and Naoki Ohtani. Excitonic rabi oscillations in self-assembled quantum dots in the presence of a local field effect. *Phys. Rev. B*, 87:241301, Jun 2013.
- [8] S. Azizoglu, S. Koc, and O. Buyukdura. Time domain scattering of scalar waves by two spheres in free-space. *SIAM Journal on Applied Mathematics*, 70(3):694–709, 2009.
- [9] Nicolas Bachelard, Rémi Carminati, Patrick Sebbah, and Christian Vanneste. Linear and nonlinear rabi oscillations of a two-level system resonantly coupled to an anderson-localized mode. *Phys. Rev. A*, 91:043810, Apr 2015.
- [10] Pierre Barthelemy, Jacopo Bertolotti, and Diederik S. Wiersma. A Lévy flight for light. *Nature*, 453:495 EP –, May 2008.
- [11] Jean-Pierre Berenger. A perfectly matched layer for the absorption of electromagnetic waves. *Journal of Computational Physics*, 114(2):185 – 200, 1994.
- [12] E. Bleszynski, M. Bleszynski, and T. Jaroszewicz. AIM: Adaptive integral method for solving large-scale electromagnetic scattering and radiation problems. *Radio Science*, 31(5):1225–1251, Sept 1996.
- [13] M. J. Blomley, J. C. Cooke, E. C. Unger, M. J. Monaghan, and D. O. Cosgrove. Microbubble contrast agents: a new era in ultrasound. *BMJ*, 322(7296):1222–1225, May 2001.
- [14] M. J. Bluck and S. P. Walker. Time-domain bie analysis of large three-dimensional electromagnetic scattering problems. *IEEE Transactions on Antennas and Propagation*, 45(5):894–901, May 1997.

- [15] R. Bonifacio, P. Schwendimann, and Fritz Haake. Quantum statistical theory of superradiance. i. *Phys. Rev. A*, 4:302–313, Jul 1971.
- [16] R. Bonifacio, P. Schwendimann, and Fritz Haake. Quantum statistical theory of superradiance. ii. *Phys. Rev. A*, 4:854–864, Sep 1971.
- [17] F. Borgnis. Acoustic radiation pressure of plane compressional waves. *Rev. Mod. Phys.*, 25:653–664, Jul 1953.
- [18] David C. Burnham and Raymond Y. Chiao. Coherent resonance fluorescence excited by short light pulses. *Phys. Rev.*, 188:667–675, Dec 1969.
- [19] M J Caola. Solid harmonics and their addition theorems. *Journal of Physics A: Mathematical and General*, 11(2):L23, 1978.
- [20] Qing-Hu Chen, Yu-Yu Zhang, Tao Liu, and Ke-Lin Wang. Numerically exact solution to the finite-size dicke model. *Phys. Rev. A*, 78:051801, Nov 2008.
- [21] Hank Childs, Eric Brugger, Brad Whitlock, Jeremy Meredith, Sean Ahern, David Pugmire, Kathleen Biagas, Mark Miller, Cyrus Harrison, Gunther H. Weber, Hari Krishnan, Thomas Fogal, Allen Sanderson, Christoph Garth, E. Wes Bethel, David Camp, Oliver Rübél, Marc Durant, Jean M. Favre, and Paul Navrátil. VisIt: An End-User Tool For Visualizing and Analyzing Very Large Data. In *High Performance Visualization—Enabling Extreme-Scale Scientific Insight*, pages 357–372. Oct 2012.
- [22] Claude Cohen-Tannoudji, Jacques Dupont-Roc, and Gilbert Grynberg. *Photons and atoms: introduction to quantum electrodynamics*. Wiley Online Library, 1989.
- [23] Xiaoyun Ding, Jinjie Shi, Sz-Chin Steven Lin, Shahrzad Yazdi, Brian Kiraly, and Tony Jun Huang. Tunable patterning of microparticles and cells using standing surface acoustic waves. *Lab Chip*, 12:2491–2497, 2012.
- [24] Y. Ding, A. Forestier, and T. Ha Duong. A galerkin scheme for the time domain integral equation of acoustic scattering from a hard surface. *The Journal of the Acoustical Society of America*, 86(4):1566–1572, 1989.
- [25] Alexander A. Doinikov. Mathematical model for collective bubble dynamics in strong ultrasound fields. *The Journal of the Acoustical Society of America*, 116(2):821–827, 2004.
- [26] Alexander A. Doinikov, Richard Manasseh, and Andrew Ooi. Time delays in coupled multibubble systems (I). *The Journal of the Acoustical Society of America*, 117(1):47–50, 2005.
- [27] A. A. Ergin, B. Shanker, and E. Michielssen. The plane-wave time-domain algorithm for the fast analysis of transient wave phenomena. 41(4):39–52.
- [28] A. A. Ergin, Balasubramaniam Shanker, and Eric Michielssen. Analysis of transient wave scattering from rigid bodies using a burton–miller approach. *The Journal of the Acoustical Society of America*, 106(5):2396–2404, 1999.

- [29] A. Arif Ergin, Balasubramaniam Shanker, and Eric Michielssen. Acceleration of integral equation based transient analysis of acoustic scattering phenomena using the plane wave time domain algorithm. *The Journal of the Acoustical Society of America*, 106(4):2195–2195, 1999.
- [30] A Fratalocchi, C Conti, and G Ruocco. Mode competitions and dynamical frequency pulling in Mie nanolasers: 3d ab-initio Maxwell-Bloch computations. *Optics express*, 16(12):8342–8349, 2008.
- [31] Matteo Frigo. A fast Fourier transform compiler. *SIGPLAN Not.*, 34(5):169–180, May 1999.
- [32] Amparo Gil, Javier Segura, and Nico Temme. *Numerical Methods for Special Functions*. 01 2007.
- [33] Andreas Glaser and Vladimir Rokhlin. A new class of highly accurate solvers for ordinary differential equations. *Journal of Scientific Computing*, 38(3):368–399, 2009.
- [34] Connor Glosser. cglosser/QuEST: v0.1.0, May 2017.
- [35] Connor Glosser. cglosser/QuEST: v0.2.1. May 2018.
- [36] Connor Glosser, Carlo Piermarocchi, Jie Li, Dan Dault, and B. Shanker. Computational dynamics of acoustically driven microsphere systems. *Phys. Rev. E*, 93:013305, Jan 2016.
- [37] Leslie Frederick Greengard. *The Rapid Evaluation of Potential Fields in Particle Systems*. PhD thesis, New Haven, CT, USA, 1987. AAI8727216.
- [38] M. Gross and S. Haroche. Superradiance: An essay on the theory of collective spontaneous emission. *Physics Reports*, 93(5):301 – 396, 1982.
- [39] Gaël Guennebaud, Benoît Jacob, et al. Eigen v3. <http://eigen.tuxfamily.org>, 2010.
- [40] Nail A. Gumerov and Ramani Duraiswami. Computation of scattering from n spheres using multipole reexpansion. *The Journal of the Acoustical Society of America*, 112(6):2688–2701, 2002.
- [41] Fritz Haake, Harald King, Guntram Schröder, Joe Haus, and Roy Glauber. Fluctuations in superfluorescence. *Phys. Rev. A*, 20:2047–2063, Nov 1979.
- [42] Sophie Hernot and Alexander L. Klibanov. Microbubbles in ultrasound-triggered drug and gene delivery. *Advanced Drug Delivery Reviews*, 60(10):1153 – 1166, 2008. *Ultrasound in Drug and Gene Delivery*.
- [43] H. Htoon, T. Takagahara, D. Kulik, O. Baklenov, A. L. Holmes, and C. K. Shih. Interplay of rabi oscillations and quantum interference in semiconductor quantum dots. *Phys. Rev. Lett.*, 88:087401, Feb 2002.

- [44] Yurii A. Ilinskii, Mark F. Hamilton, and Evgenia A. Zabolotskaya. Bubble interaction dynamics in lagrangian and hamiltonian mechanics. *The Journal of the Acoustical Society of America*, 121(2):786–795, 2007.
- [45] J.D. Jackson. *Classical Electrodynamics*. Wiley, 2007.
- [46] Frank Jahnke, Christopher Gies, Marc Aßmann, Manfred Bayer, HAM Leymann, Alexander Foerster, Jan Wiersig, Christian Schneider, Martin Kamp, and Sven Höfling. Giant photon bunching, superradiant pulse emission and excitation trapping in quantum-dot nanolasers. *Nature communications*, 7, 2016.
- [47] Eric Jones, Travis Oliphant, Pearu Peterson, et al. SciPy: Open source scientific tools for Python, 2001–. [Online; accessed 2014-10-14].
- [48] H. Kamada, H. Gotoh, J. Temmyo, T. Takagahara, and H. Ando. Exciton rabi oscillation in a single quantum dot. *Phys. Rev. Lett.*, 87:246401, Nov 2001.
- [49] S. Kapur and D. E. Long. IES³: a fast integral equation solver for efficient 3-dimensional extraction. In *1997 Proceedings of IEEE International Conference on Computer Aided Design (ICCAD)*, pages 448–455, Nov 1997.
- [50] Louis V. King. On the acoustic radiation pressure on spheres. *Proceedings of the Royal Society of London A: Mathematical, Physical and Engineering Sciences*, 147(861):212–240, 1934.
- [51] Fredrik Kjolstad, Shoaib Kamil, Stephen Chou, David Lugato, and Saman Amarasinghe. The tensor algebra compiler. *Proc. ACM Program. Lang.*, 1(OOPSLA):77:1–77:29, October 2017.
- [52] Donald Knuth. *The Art of Computer Programming*. Addison-Wesley, Reading, Mass, 1997.
- [53] L.D. Landau and E.M. Lifshitz. *Fluid Mechanics*. Number v. 6. Elsevier Science, 2013.
- [54] Jie Li, Daniel Dault, and Balasubramaniam Shanker. A quasianalytical time domain solution for scattering from a homogeneous sphere. *The Journal of the Acoustical Society of America*, 135(4):1676–1685, 2014.
- [55] J. C. MacGillivray and M. S. Feld. Theory of superradiance in an extended, optically thick medium. *Phys. Rev. A*, 14:1169–1189, Sep 1976.
- [56] G. Manara, A. Monorchio, and R. Reggiannini. A space-time discretization criterion for a stable time-marching solution of the electric field integral equation. *IEEE Transactions on Antennas and Propagation*, 45(3):527–532, Mar 1997.
- [57] G. Mur. Absorbing boundary conditions for the finite-difference approximation of the time-domain electromagnetic-field equations. *IEEE Transactions on Electromagnetic Compatibility*, EMC-23(4):377–382, Nov 1981.

- [58] M. K. Myers and J. S. Hausmann. Computation of acoustic scattering from a moving rigid surface. *The Journal of the Acoustical Society of America*, 91(5):2594–2605, 1992.
- [59] Filip Petersson, Lena Åberg, Ann-Margret Swärd-Nilsson, and Thomas Laurell. Free flow acoustophoresis: Microfluidic-based mode of particle and cell separation. *Analytical Chemistry*, 79(14):5117–5123, 2007. PMID: 17569501.
- [60] A. J. Pray, Y. Beghein, N. V. Nair, K. Cools, H. Bağcı, and B. Shanker. A higher order space-time galerkin scheme for time domain integral equations. *IEEE Transactions on Antennas and Propagation*, 62(12):6183–6191, Dec 2014.
- [61] A. J. Pray, N. V. Nair, and B. Shanker. Stability properties of the time domain electric field integral equation using a separable approximation for the convolution with the retarded potential. *IEEE Transactions on Antennas and Propagation*, 60(8):3772–3781, Aug 2012.
- [62] William H. Press, Saul A. Teukolsky, William T. Vetterling, and Brian P. Flannery. *Numerical Recipes 3rd Edition: The Art of Scientific Computing*. Cambridge University Press, New York, NY, USA, 3 edition, 2007.
- [63] Nicholas E. Rehler and Joseph H. Eberly. Superradiance. *Phys. Rev. A*, 3:1735–1751, May 1971.
- [64] E.J. Rothwell and M.J. Cloud. *Electromagnetics, Second Edition*. Electrical Engineering Textbook Series. Taylor & Francis, 2009.
- [65] Michael Scheibner, Thomas Schmidt, Lukas Worschech, Alfred Forchel, Gerd Bacher, Thorsten Passow, and Detlef Hommel. Superradiance of quantum dots. *Nat Phys*, 3(2):106–110, Feb 2007.
- [66] Tal Schwartz, Guy Bartal, Shmuel Fishman, and Mordechai Segev. Transport and anderson localization in disordered two-dimensional photonic lattices. *Nature*, 446(7131):52–55, Mar 2007.
- [67] B. Shanker, A. A. Ergin, K. Aygun, and E. Michielssen. Analysis of transient electromagnetic scattering from closed surfaces using a combined field integral equation. *IEEE Transactions on Antennas and Propagation*, 48(7):1064–1074, Jul 2000.
- [68] G. Ya. Slepyan, A. Magyarov, S. A. Maksimenko, A. Hoffmann, and D. Bimberg. Rabi oscillations in a semiconductor quantum dot: Influence of local fields. *Phys. Rev. B*, 70:045320, Jul 2004.
- [69] G. Ya. Slepyan, S. A. Maksimenko, A. Hoffmann, and D. Bimberg. Quantum optics of a quantum dot: Local-field effects. *Phys. Rev. A*, 66:063804, Dec 2002.
- [70] T. H. Stievater, Xiaoqin Li, D. G. Steel, D. Gammon, D. S. Katzer, D. Park, C. Piermarocchi, and L. J. Sham. Rabi oscillations of excitons in single quantum dots. *Phys. Rev. Lett.*, 87:133603, Sep 2001.

- [71] C. R. Stroud, J. H. Eberly, W. L. Lama, and L. Mandel. Superradiant effects in systems of two-level atoms. *Phys. Rev. A*, 5:1094–1104, Mar 1972.
- [72] Vasily V. Temnov and Ulrike Woggon. Superradiance and subradiance in an inhomogeneously broadened ensemble of two-level systems coupled to a low- q cavity. *Phys. Rev. Lett.*, 95:243602, Dec 2005.
- [73] Vasily V Temnov and Ulrike Woggon. Photon statistics in the cooperative spontaneous emission. *Optics express*, 17(7):5774–5782, 2009.
- [74] M. L. W. Thewalt. Details of the structure of bound excitons and bound multiexciton complexes in si. *Canadian Journal of Physics*, 55(17):1463–1480, 1977.
- [75] A. Tiwari, C. Pantano, and J. B. Freund. Growth-and-collapse dynamics of small bubble clusters near a wall. *Journal of Fluid Mechanics*, 775:1–23, 7 2015.
- [76] Federico Toschi and Eberhard Bodenschatz. Lagrangian properties of particles in turbulence. *Annual Review of Fluid Mechanics*, 41(1):375–404, 2009.
- [77] L. Tsang, K. H. Ding, S. E. Shih, and J. A. Kong. Scattering of electromagnetic waves from dense distributions of spheroidal particles based on monte carlo simulations. *J. Opt. Soc. Am. A*, 15(10):2660–2669, Oct 1998.
- [78] Xander F. van Kooten, Julien Autebert, and Govind V. Kaigala. Passive removal of immiscible spacers from segmented flows in a microfluidic probe. *Applied Physics Letters*, 106(7):074102, 2015.
- [79] C. Vanneste and P. Sebbah. Selective excitation of localized modes in active random media. *Phys. Rev. Lett.*, 87:183903, Oct 2001.
- [80] Pete Vukusic, Benny Hallam, and Joe Noyes. Brilliant whiteness in ultrathin beetle scales. *Science*, 315(5810):348–348, 2007.
- [81] P. C. Waterman. New formulation of acoustic scattering. *The Journal of the Acoustical Society of America*, 45(6):1417–1429, 1969.
- [82] Ling Ye, Jing Liu, Ping Sheng, and D.A. Weitz. Sound propagation in suspensions of solid spheres. *Phys. Rev. E*, 48:2805–2815, Oct 1993.
- [83] Zhen Ye. Low-frequency acoustic scattering by gas-filled prolate spheroids in liquids. *The Journal of the Acoustical Society of America*, 101(4):1945–1952, 1997.
- [84] A. E. Yilmaz, Jian-Ming Jin, and E. Michielssen. Time domain adaptive integral method for surface integral equations. *IEEE Transactions on Antennas and Propagation*, 52(10):2692–2708, Oct 2004.
- [85] Zorana Zeravcic, Detlef Loshe, and Wim Van Saarloos. Collective oscillations in bubble clouds. *Journal of Fluid Mechanics*, 680:114–149, 8 2011.